Dottorato di Ricerca in Scienze della Terra
XXVII ciclo

CURRICULUM: safeguard and soil conservation, environmental vulnerability and hydrogeologic protection.

"Investigation of a rockslide from its local seismic response"

"Analisi di una frana in roccia dalla sua risposta sismica locale"

Thesis submitted to fulfil the requirements
for a PhD degree in Earth Science, Geology

DOCTORATE CO-ORDINATOR
PROF. LORENZO ROOK

Tutor:
Prof. Sandro Moretti

Applicant:
Alessia Lotti

Co-tutor:
Prof. Gilberto Saccorotti

2011/2014

“Prevention costs 3-4 times less than repairing the damage. What’s more, due to this situation, we’re losing culture, tourism, and our positive image”

Gian Vito Graziano, President of the National Council of Geologists.

INDEX

PREFACE

For many years, the European geologists' convention have turned their attention to the massive problem of landslides in Italy. The topic is high on the agenda especially because roughly 70% of all landslides on the European continent are concentrated in Italy. As a result of Italy's steep slopes, high seismic activity, soil properties and bedrock, the hillsides in many valleys have unstable rock masses. This results in constant rock falls and rock slides of various sizes and type. A thorough understanding of failure types, the mechanisms and causes of landslides is required to effectively mitigate their catastrophic consequences.

The Istituto di Ricerca per la Protezione Idrogeologica (IRPI CNR) estimated that in Italy about 3,300 fatalities and 1,850 injuries occurred between 1963 and 2012. Consequently landslides represents one of the prominent geological hazard in our country, causing more than 55 fatalities on average each year.

Landslides occur in a wide variety of geomechanical conditions and geological settings and as a response to various loading and triggering processes, such as intense rainfall, earthquakes, changes in water levels, storm waves or rapid stream erosion, that causes a rapid increase in shear stress or decrease in shear strength of slope-forming materials. Moreover, such human activities as deforestation, slope excavations for road or railway construction, or mining have led to an increase in the occurrence of landslides.

These kind of disasters, which have caused thousands of casualties and huge economic losses, can occur without discernible warning but there are well-documented cases of signals that forecast the movement which is the main focus of the present work. Currently there are several early warning systems that can be implemented in order to prevent loss of life and reduce the economic and material impact of landslides but more frequently it is not easy to find a technique capable to provide an immediate alert.

Slope failure of rock masses represents an interesting case study for verifying the feasibility of using passive seismic monitoring to detect signals related to micro-cracking, and possible variations in the elastic parameters of the rock body related to changes in pore-fluid pressure, consolidation, and micro-fracturing that could forecast failure.

In this context, the IFFI Project carried out by APAT (now in ISPRA) - Geological Survey of Italy/Land Protection and Georesources Department, in collaboration with the Regions and the Self-Governing Provinces has made an homogenous and updated inventory of Italian landslide that pointed out the importance of setting an appropriate monitoring system able to ensure safety and mitigate the risk showing the wide distribution of Municipalities that are currently threatened by landslide risk. In 2005, APAT published the IFFI Inventory on the

Internet with the aim of disseminating information about landslides to national and local administrations, research institutes, geologists, engineers and citizens. As of today the inventory has registered almost 499,511 landslide phenomena affecting an area of around 21,182 km^2, or 7% of the nation.

Umbria Region, where our test site is located, represents one of the Regions more prone to landslides as illustrated in Figure I.

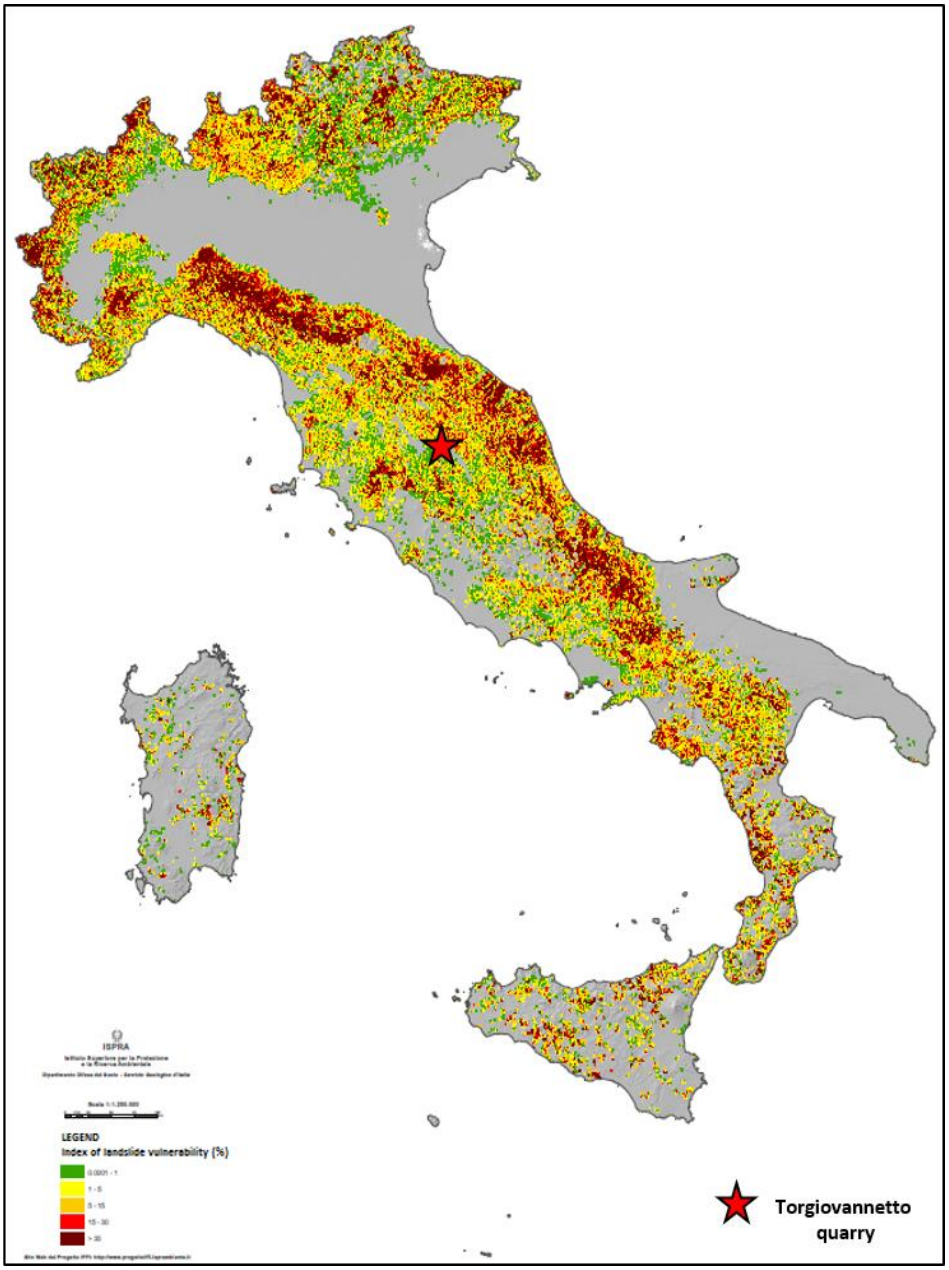

Figure I – Map of the Italian index of landslide vulnerability.

For the purpose of this research project, we carried out a pilot experiment dedicated to verifying the performance of a small-scale seismic network as a part of an early-warning system dedicated to an unstable rock mass monitoring.

INTRODUCTION

The contents and goals of the present work can be summarized through the use of a few key-words which facilitate the understanding of the discussed topics in one glance.

For each section of this thesis, the representative key-words are: *rockslide*, *passive prospecting*, *site effects*, *continuous monitoring*, *transient analysis*. In the following, the significance of these terms is briefly explained with relation to the synopsis of the present dissertation.

Rockslide.

This term refers to slopes formed by competent rock characterized by the presence of unstable block/blocks that could move downslope along a bedding plane, joint or area of weakness. This type of landslide can be extremely dangerous because the falling blocks destroy everything in their path and can reach great distance due to the energy acquired during the fall. In addition, they are particularly difficult to monitor and characterized in terms of size and stability of the unstable rock mass.

The test-site is a dismissed limestone quarry located nearby the town of Assisi (Central Apennines, Italy) where a rockfall and two subsequent reactivation occurred in 1997, 2004 (few tens of m^3) and 2005 (2500 m^3) respectively. Quarries are remarkably vulnerable areas, since the natural geomorphology is altered by the extracting activity (Graziani et al., 2009b). Physical characteristics and chronicle of the rockslide chosen as test-site for this project will be presented in detail in Chapter I together with a description of the geographical, geomorphological and geological setting of the study area by referring to previous researches (Boccaletti et al., 1971; Lavecchia et al., 1994; Intrieri et al., 2012; Ponziani et al., 2010; Brocca et al., 2012).

Passive prospecting.

While surface observation provide mainly qualitative information while geophysical prospecting allows gaining information on the internal structure of the mass, can investigate a large volume of rock at low cost, are flexible, relatively quick, non-invasive and deployable on slope.

Chapter II and Chapter III of the present work are dedicated to the presentation of the theoretical background of the geophysical methods adopted for this work.

Site effects.

Ground shaking is analysed in terms of the amplitude, frequency and duration of the three components of ground motion produced by seismic waves arriving at a given site. However, the effects of a transiting seismic wave are also strictly connected to the local geological conditions and to the geometry of subsurface heterogeneities, factors which are often difficult to estimate, especially for rockslide characterized by highly fractured materials. Both the above conditions could induce the amplification of the seismic signal and the activation (or reactivation) of unstable masses and rock block so that every additional information about the internal structure of the slope is a major input parameter in slope stability analysis.

First section (A) of Chapter IV extensively deals with this aspect using mainly Horizontal to Vertical Spectral Ratio (HVSR) technique (Nogoshi and Igarashi, 1970; Nakamura, 1989, 2000; Mucciarelli and Gallipoli, 2001) evaluated both at single-station (Field and Jacob, 1993; Chavez-Garcia et al., 1990; Lermo and Chavez-Garcia, 1993, 1994; Lachet et al., 1996) and in array configuration. The discussion also relates to the HVSR directivity analysis (Del Gaudio et al., 2008, 2011).

Continuous monitoring.

Monitoring and surveillance are strictly connected with risk management, because they imply the continuous acquisition of data that provide information on the studied system in order to forecast its future evolution.

In the last years, beside the traditional geotechnical and structural monitoring (topographic total stations, extensometers and inclinometers; Moore et al., 2010), new techniques have been used: aerial photos, LiDAR (McKean and Roering, 2004; McKean et al., 2004); GPS monitoring (Parise et al., 2004); InSAR technique (Antonello et al., 2004; Casagli et al., 2010); laser scanner (Casagli et al., 2012; Gigli and Casagli, 2013) and infrared termography (Frodella et al., 2014; Baroň et al., 2013).

Actually, shallow geophysics represent a valid complement to the aforementioned methods (Helmstetter and Garambois, 2010; Amitrano et al., 2010; Arosio et al., 2009a; Blikra, 2008); for the purpose of this research project, I carried out a pilot experiment dedicated to verifying the performance of a small-scale seismic network as a part of an early-warning system dedicated to an unstable rock mass.

This part, discussed in Chapter IV, section B, will be focus on the evaluation of the seismic velocity at the test site. Through the HVSR and the Noise Correlation Function (Shapiro et

al., 2005; Brenguier et al., 2008b; Picozzi et al., 2009; Mainsant, 2012) evaluated through the entire period of recording.

Transient analysis.

Continuous seismic monitoring also allows the recording of seismic signals possibly related to both brittle failure and rock falls (Amitrano et al., 2005, 2007, 2010; Levy et al., 2011). The recognition of seismic transients generated by the energy released during a micro-fracturing process could represent precursory pattern of a rockfall (Walter et al., 2012) while the exact location (Lacroix and Helmstetter, 2011) of them allows to detect weakened areas. This data associated with the falling rocks trajectory reconstruction (each impact of boulders on the ground will produce a localizable transient signal) could help to define the areas most prone to rockfall events. Section C of Chapter IV will deal with this subject.

The Torgiovannetto site, which is extensively monitored using traditional methods, offers the possibility to develop a multiparameter analysis that could be useful in understanding the mechanisms that control the rockslide dynamics and to evaluate possible connection between rainfall /temperature/ displacement and rockslide seismic activity.

Within this context the present works aims at several objectives: (1) to characterize the seismic response of the unstable rock mass, in order to map and quantify the occurrence of possible amplification phenomena, useful for understanding the response of the rockslide to seismic waves issued by external sources; (2) to investigate if correlation exists between the local seismic response at a very short-scale and the surface geology; (3) to investigate the feasibility of a seismic monitoring system for the automatic detection of rockfalls or brittle failure episodes within the unstable rock mass; (4) to investigate whether the analysis of ambient noise signals provide constraint on possible, tiny changes in the seismic wave velocities, which in turn could be correlated with variations in the local stress conditions /degree of fracturing /fluid content and pore pressure of the propagation medium.

CHAPTER 1 - DESCRIPTION OF THE STUDY AREA: TORGIOVANNETTO ROCKSLIDE

1.1 Geographical, Geomorphological and Geological Setting

The landslide, classified as a rockslide, is located in Umbria Region that covers 8456 km^2 in Central Italy. The landscape is hilly or mountainous, with open valleys and intra-mountain basins. The elevation range from 50 to 2436m a.s.l. and the drainage is led by the Tiber River, a tributary of the Tyrrenian Sea. Rainfall mainly occurs from October to February, with cumulative annual values ranging from 700 to 2000 mm.

Geomorphological investigations revealed that landslides cover about 14% of the entire land area and affect many cities and towns, including Perugia, Orvieto, Todi, Montone, Allerona and Assisi (Felicioni et al., 1994). The neighbourhood of the last one hosts the test site related to this application on the southward facing slope of Mount Subasio (43°4'35"N 12°38'30"E; Figure 1).

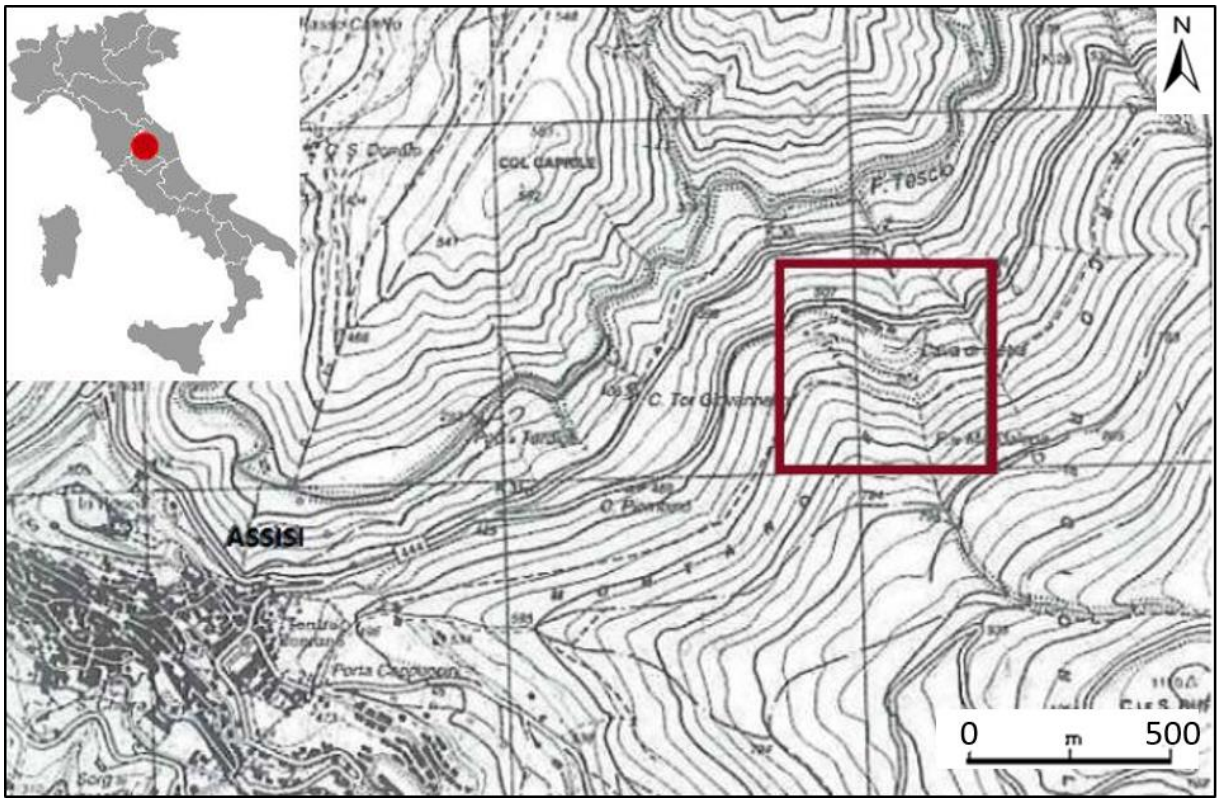

Figure 1 – Geographical location of the study area (extract IGM fg. 311 sez. II "Assisi") about 2 km northeast of Assisi.

Mount Subasio (1109 m a.s.l.) is part of the Umbria-Marche Apennines, a complex fold and thrust arcuate belt which occupies the outer zones of the Northern Apennines of Italy. The

belt developed during the Neogene as a result of the closure of the Ligurian Ocean followed by the continental collision between the European Corsica-Sardinia Margin and the African Adria Promontory (Boccaletti et al., 1971): a northeast-directed compressional tectonic phase started during the middle Miocene and is still active near the Adriatic coast (Barchi et al, 1998b). During the upper Pliocene started an extensional phase with a principal stress oriented about NE-SW which resulted in the dissection of the Umbria-Marche Apennines and the opening of a NW-SE-trending set of continental basins (Figure 2).

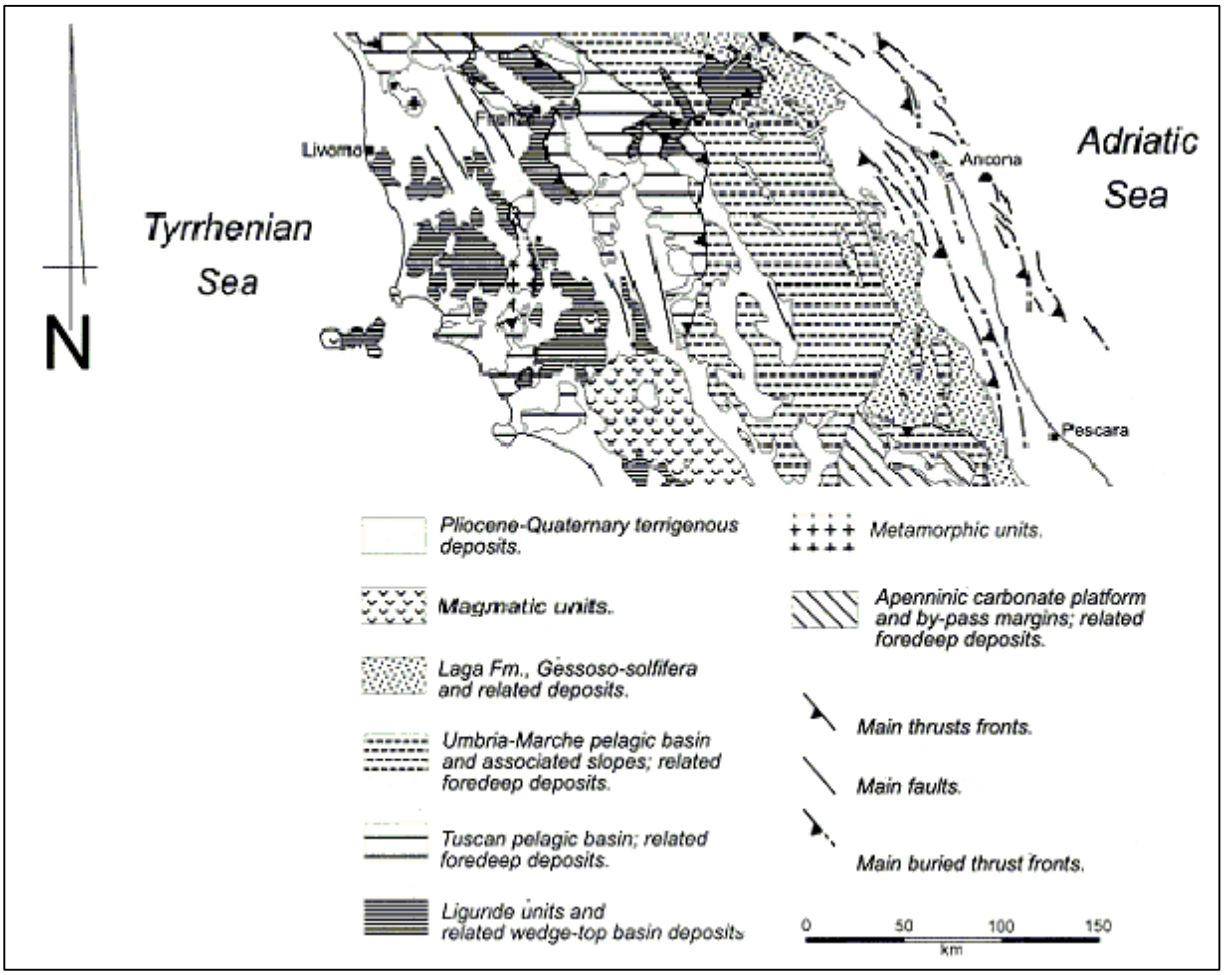

Figure 2 – Geological sketch of Central Italy (Butler et al., 2001, modified).

Mount Subasio area consists in a SSE-NNW trending anticline (Intrieri et al., 2012) with layers dipping almost vertically in the NE side of the mountain with several NW-SE striking normal faults on the eastern and western flanks.

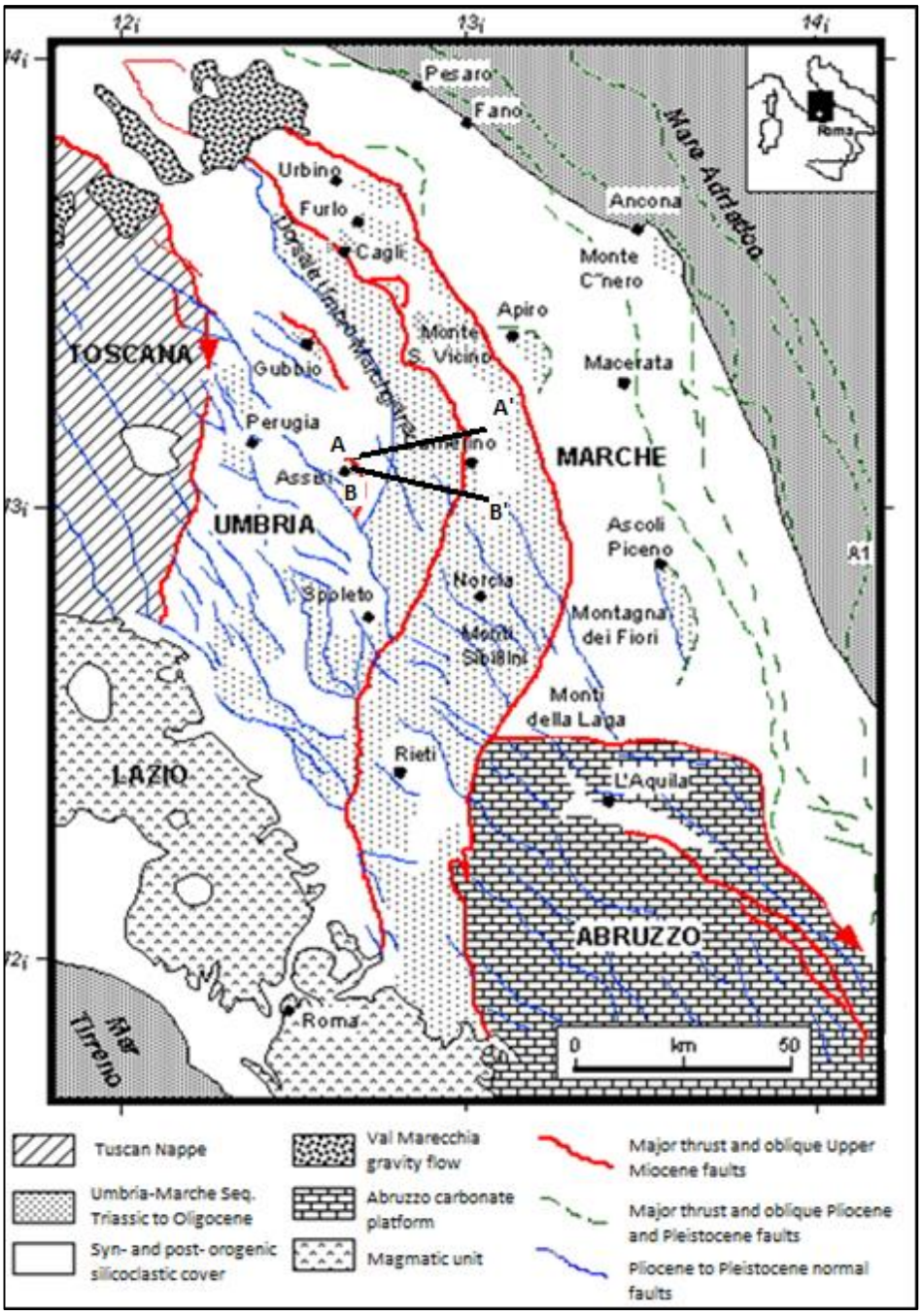

Figure 3 – Schematic geological map of the Umbria-Marche region showing the alignment of the principle group of the Umbria Fault System and the section lines AA' and BB' visible in Figure 4. Fault pattern is from Lavecchia et al. (1994).

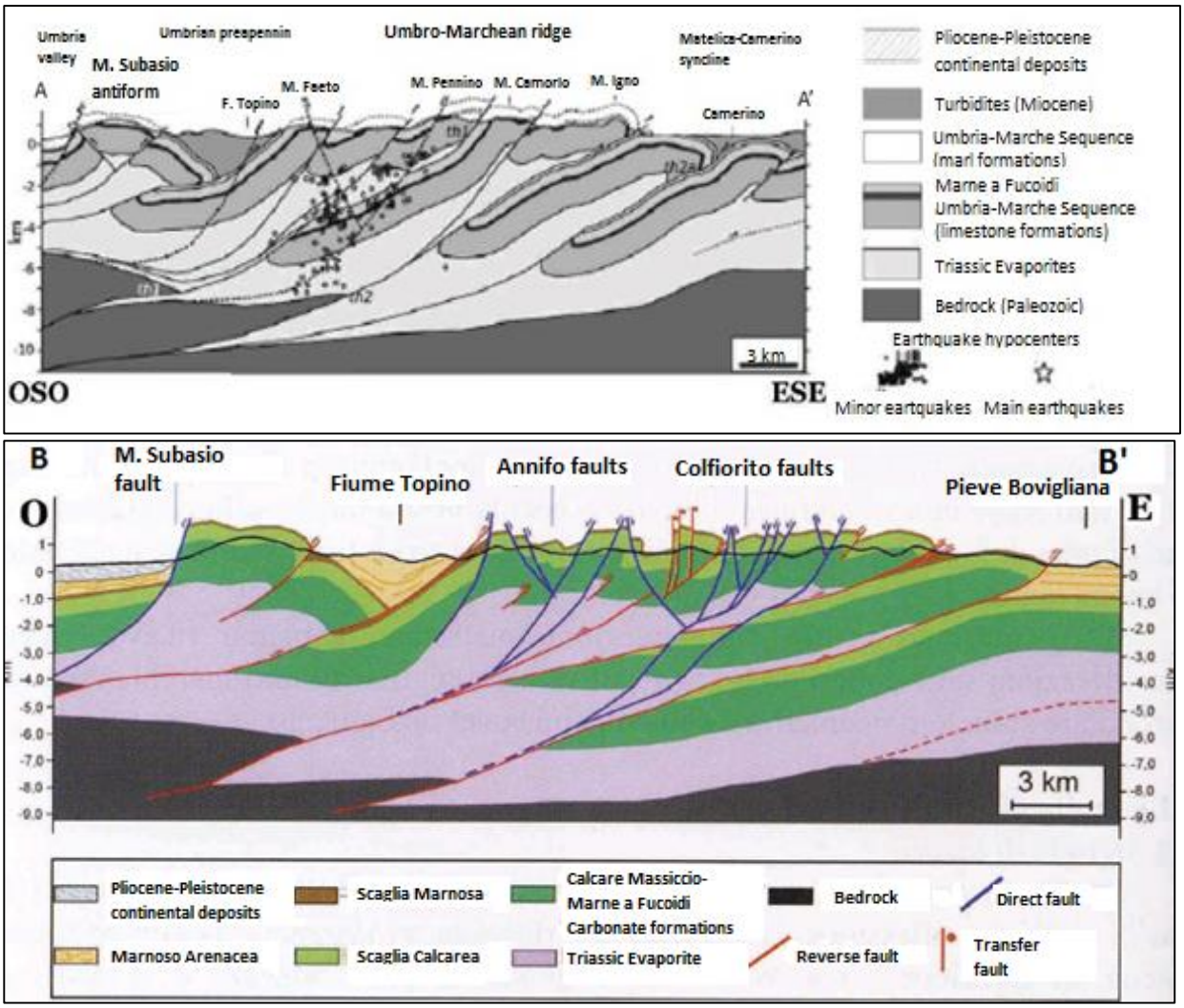

Figure 4 – Umbria-Marchean Apennines geological setting and location of section AA' and BB'.

The local geological formations, belonging to Serie Umbro-Marchigiana (from Calcare Massiccio to Marnoso Arenacea), represent the progressive sinking of a marine environment (Figure 5).

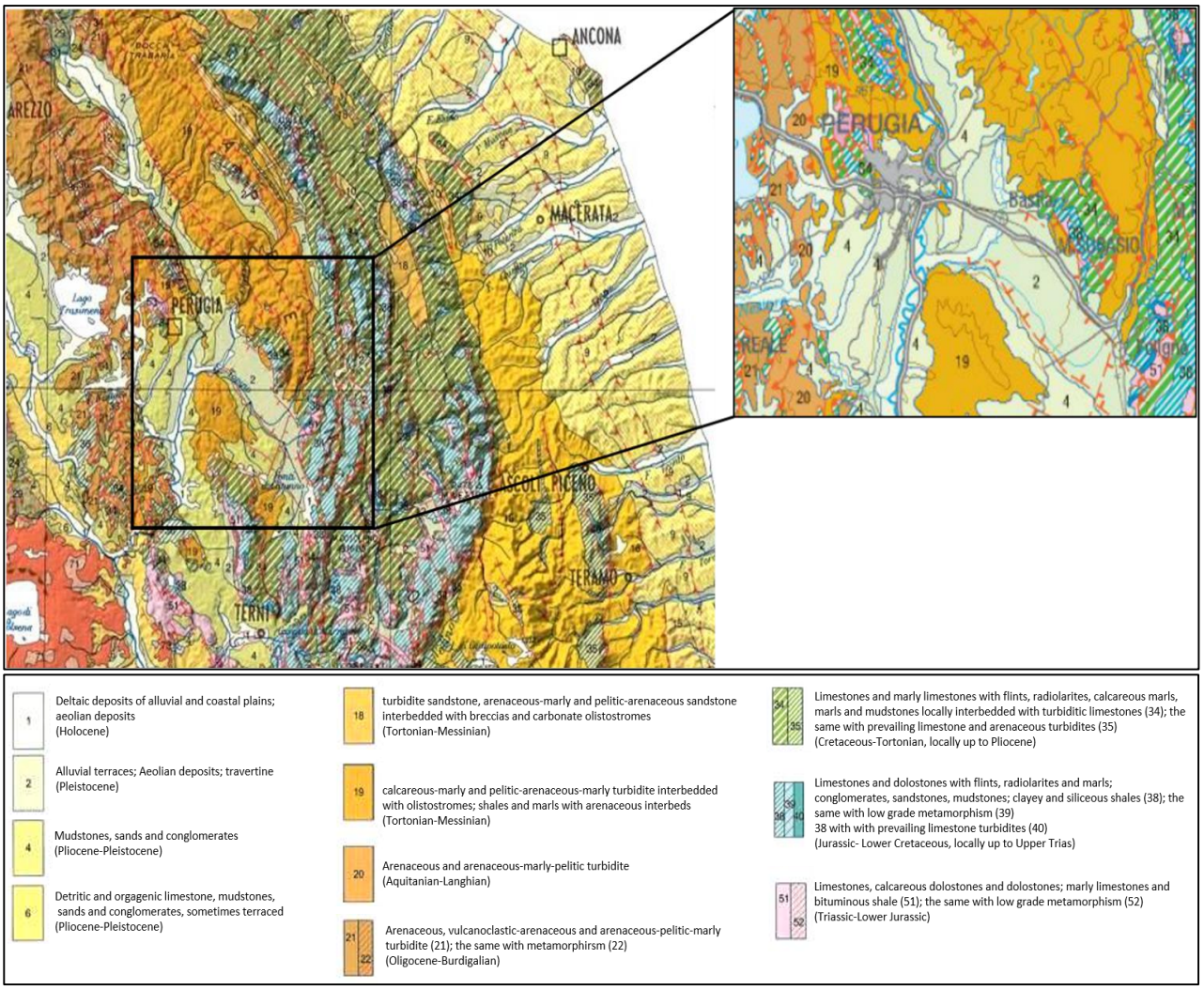

Figure 5 – Geological map of the Central Apennines and geological legend (modified from Carta Geologica d'Italia, scale 1:1 25 000). Only outcropping formations of the right figure are described in the legend. Red dashed line with notches represents direct faults; red dashed line with triangles represents thrust and reverse faults.

The test site is located in a micritic limestone former quarry (dismissed in the late '90s), 2 km NE from Assisi.

1.2 Physical characteristics and chronicle of the rockslide

The present study concentrates on a rockslide located near the city of Assisi in a seismically active part of the Apennine chain (seismic zone 2; OPCM n.3274/2003 updated BUR n.47 3/10/2012) which in past generated earthquakes of magnitude up to 6.3 Mw. The seismicity is concentrated in the SE area of Assisi in correspondence of the normal faults generated by extensional tectonic (Figure 6). The site was chosen based on the consideration that background noise level is relatively low so that even events characterized by low maximum amplitude can be easily detected.

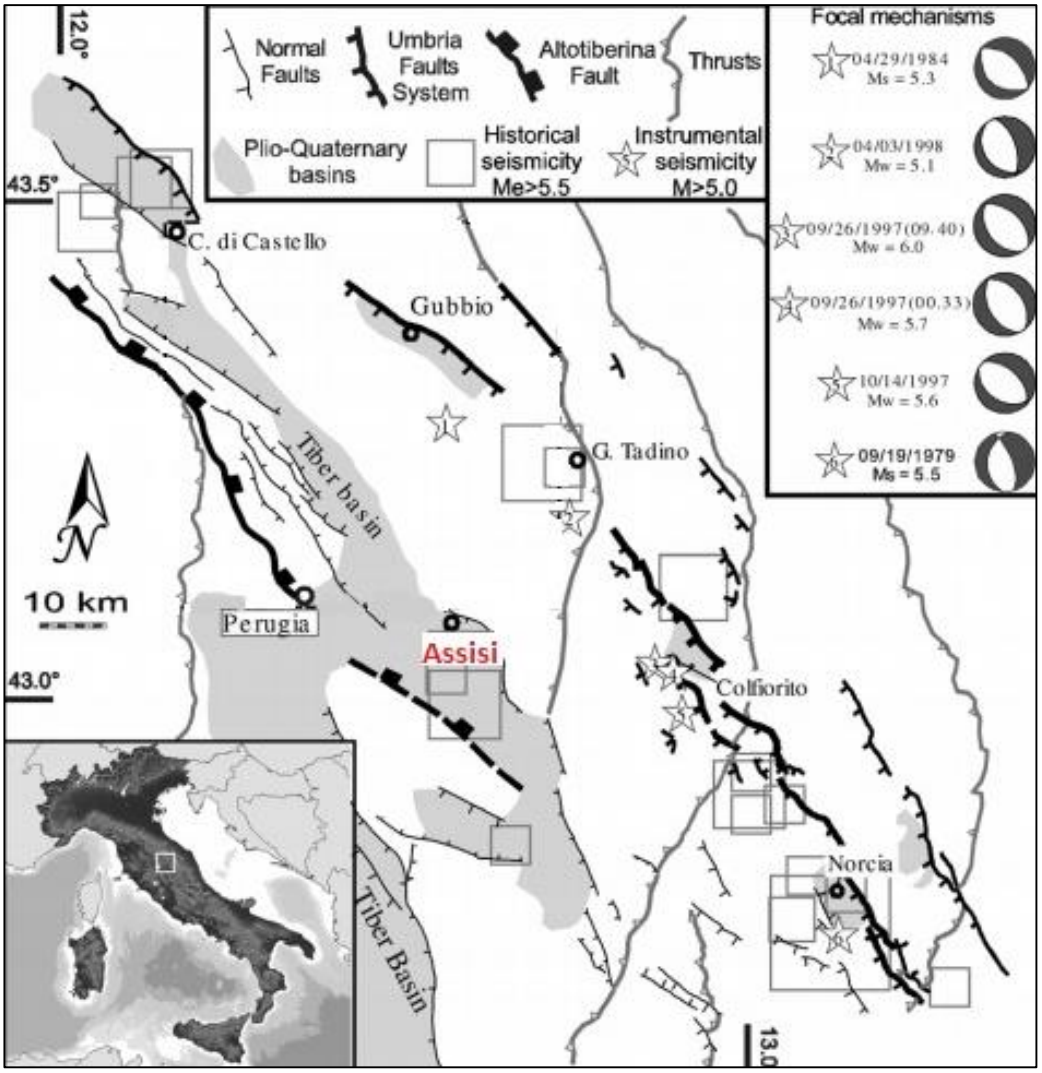

Figure 6 – Schematic structural map of the Umbria-Marche region showing the alignment of the intermountain basins along the Umbria Fault System (modified from Mirabella F. et al., 2004). Historical seismicity is reported for 461 BC – 1979 AD period (Boschi et al., 1997). Focal mechanisms and magnitude are for the 1997-98 Colfiorito sequence (Ekstroem et al., 1998), for the 1979 Norcia earthquake (Deschamps et al., 1984) and for the Gubbio earthquake (Dziewonski et al., 1985).

A first observation of the movement within the quarry site dates back to May 2003 by the State Forestry Corps, when some tension cracks were detected in the vegetated area above and within the quarry front. From then on, several monitoring campaigns were carried out by means of different instrumentations (topographic total station, inclinometers, extensometers, ground-based interferometric radar, laser scanner and infrared thermal camera). It is assured that the main predisposing factor of the instability was the quarrying activity that heavily altered the original front, actually structured in four main terraces with an overall height of about 140 m, but also the process of earthquakes-induced landslides

cannot be neglected. In fact the interconnection between those events is well-documented especially in the cases of high-magnitude seismic event (Wilson and Keefer, 1983; Jibson and Keefer, 1992, 1993; Khazai and Sitar, 2004). Given this it clearly appears that another triggering factor has to be sought in the seismic sequence that affected the area southeast of the quarry (Colfiorito basin) in the 1997-98, that reached macroseismic intensity (MCS) Io of 8-9 (Locati et al., 2011) in the Assisi area.

The research area covers a 200 x 100 m area between elevations of 550 and 680 m. The geometry and other soil parameters (such as densities, body waves velocities etc.) are well-known thanks to the geotechnical and geophysical investigations carried on the site by Alta Scuola di Perugia (2005a; 2005b; 2006a; 2006b) and Università degli Studi di Firenze (Casagli et al., 2006a; 2006b; 2007a; 2007b; Intrieri et al., 2012) since the first activity was detected. Among these investigations a passive seismic network, in continuous recording, was installed on this rockslide from December 2012 to July 2013 to support the "traditional" monitoring network composed by 13 wire extensometers, 1 accelerometer, 1 meteorological station (composed of 1 thermometer and 1 rain gauge), 3 cameras and 3 inclinometers. The monitoring network, progressively enhanced and improved through the years, was completed by means of hydrological (Ponziani et al., 2010), modeling computation analysis (Casagli et al, 2006a.; Balducci et al., 2011) and in the end by our seismological stations.

The slope consists mainly of micritic limestone belonging to the Maiolica Formation (Upper Jurassic-Lower Cretaceous) that widely outcrops in the area (Figure 7). The thickness of the Formation is about 100 m and is composed by white or light grey well stratified micritic limestone layers, whose thickness ranges between 10 cm and 1 m, and, sporadically, thin clay interlayers may occur.

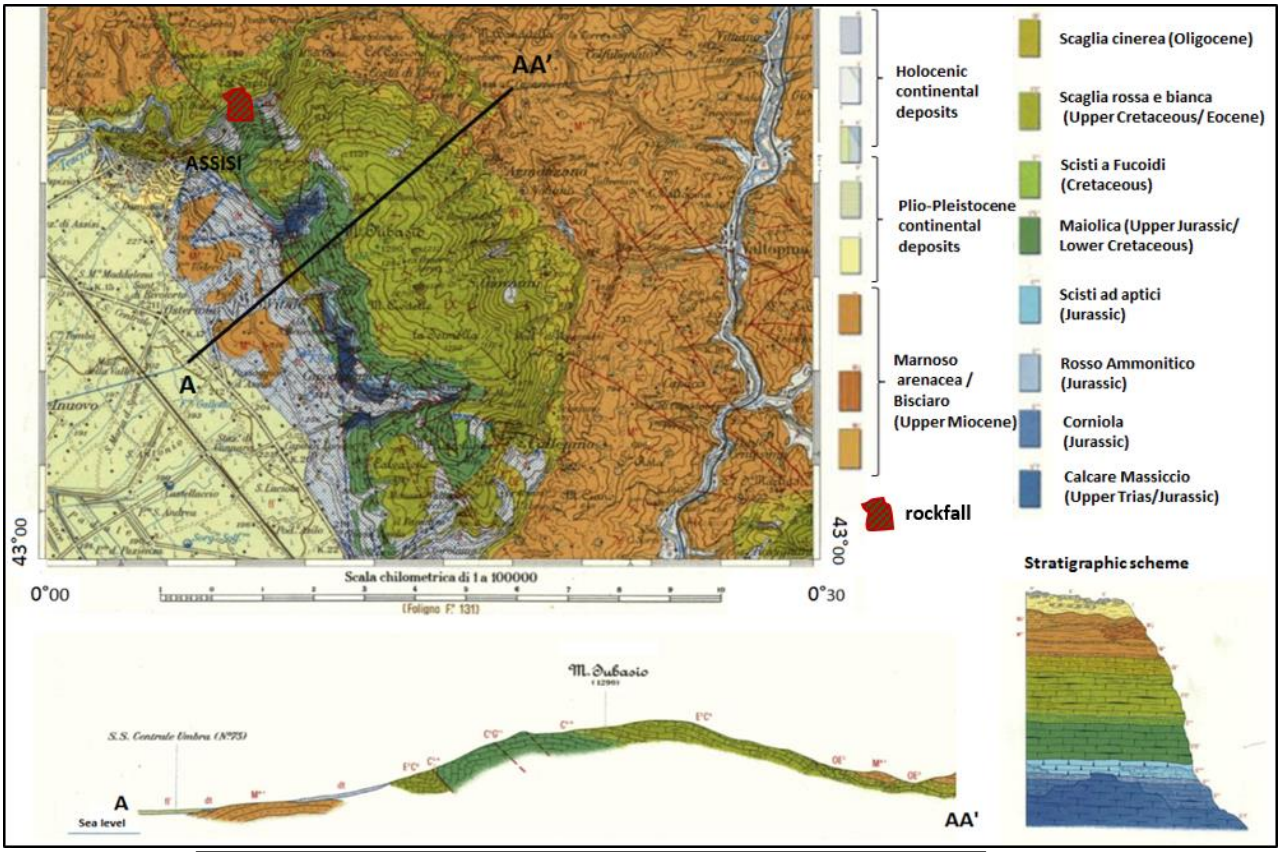

Figure 7 – In the upper part, geological map of the Mount Subasio area (modified from fg. 123 Carta Geologica d'Italia; scale 1: 100 000) indicating the geological cross-sections AA', geological legend, cross-section AA' and stratigraphic scheme of Umbria-Marchean type succession. Detail of the outcropping Maiolica Formation at Torgiovannetto site: evidence of a micritic limestone layer intercalated with clayey interlayer responsible for the sliding wedge.

The site is also partially covered by very heterometric debris (from pebble- to cobble-sized angular clasts, with scattered boulders, in a silty or coarse grained sandy matrix), some of which are anthropic in nature.

The dip direction and the dip may vary respectively from 350° to 5° and from 25° to 35°, which means that, in general, the layers dip in the same direction of the slope but with a gentler angle (Figure 8) .

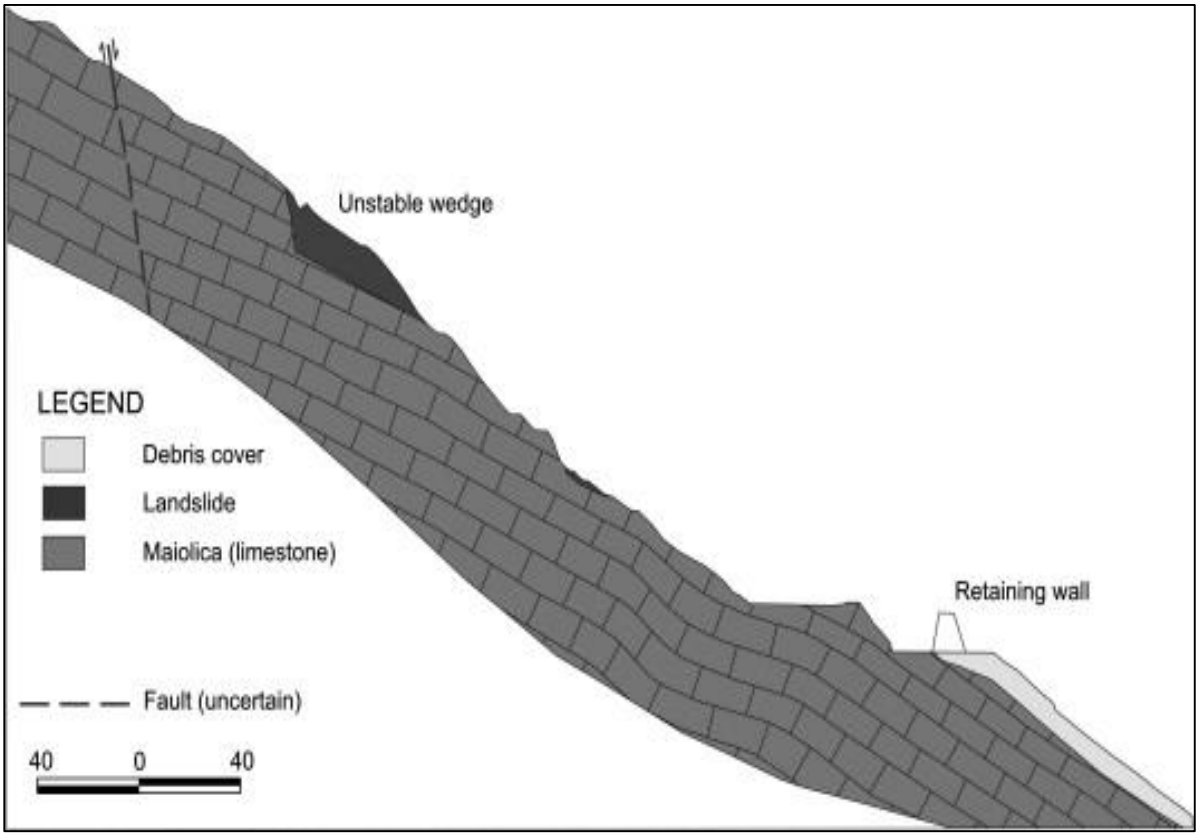

Figure 8 – Geological cross-section of the northern slope of Mount Subasio (Intrieri et al., 2012)

The rockslide (Cruden and Varnes, 1996) has a rough trapezoidal shape. Nowadays the active volume of Torgiovannetto rockslide is estimated to be about 182000 m^3. The upper boundary is defined by a big open fracture; this sub-vertical back fracture is a tension crack with an E-W strike, which in some places displays a width up to 2 m and depth of about 20 meters (Balducci et al., 2011). The fault can be seen in Figure 9.

Figure 9 – Details of the main tension crack (upper boundary) on the rear side of the quarry.

The downhill boundary, associated to a major clay interbed, is represented by a stratigraphic layer (355°/24°) that acts as sliding surface and cuts obliquely the quarry front which is associated to a major clay interbed. The estern side of the landslide is un-continuously delimited by persistent fractures belonging to a sub-vertical set having an N-S strike.

The poles of discontinuities are represented in stereographic projection and 3D representation of the sliding block in Figure 10: the main delimiting planes that more affect the kinematic of the rock block (basal (1) and western (2) plan) belong respectively to the BG (stratification) and JN1 families.

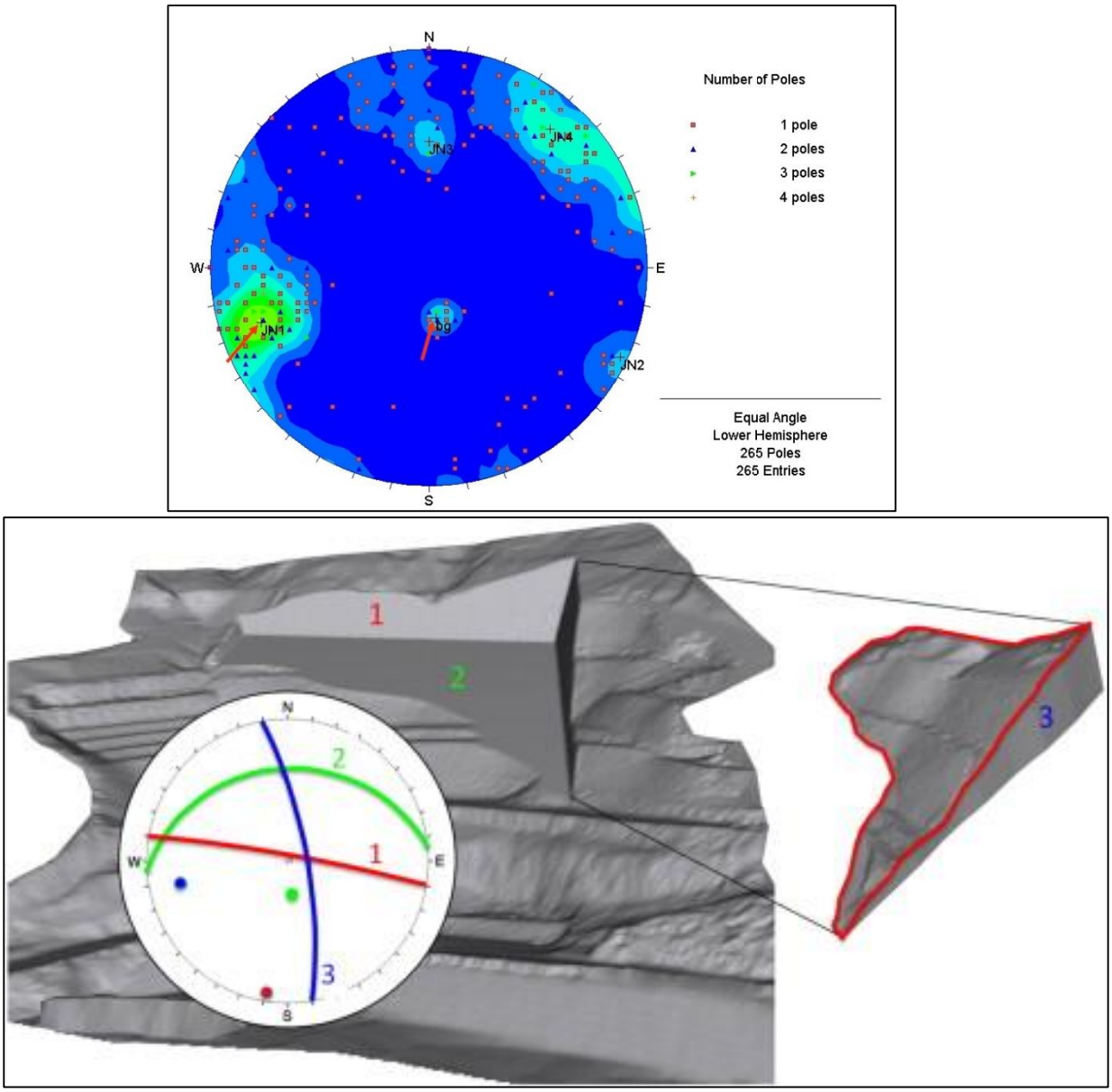

Figure 10 – Stereographic projection of the poles of discontinuities grouped into families (bg, JN1, JN2, JN3 and JN4) and 3D representation of the sliding block. Red arrows show the basal and western plan belonging families.

CHAPTER 2 - INSTRUMENTATION

2.1 Instruments and data

2.1.1 Seismic Network: gathering of seismic data

Seismic measurements were performed using a small-scale network composed of four seismic stations whose locations are shown in Figure 11. Installation at the site was not an easy challenge. Some aspects have to be considered to obtain reliable data: locations of the seismometer, access to the site, type of seismometer and electric power source.

The locations of the sensors are shown in figure : station TOR4 was located over the sliding mass while the other three stations (TOR1, TOR2 and TOR3) were located at the edge of the quarry arranged in pairs with diametrically opposite position with respect to the barycentre of the landslide. This configuration allow us to retrieve punctual information both inside and outside the landslide; furthermore, working on pairs of sensors, one can retrieve information on the state of the propagation medium in between the two sensors.

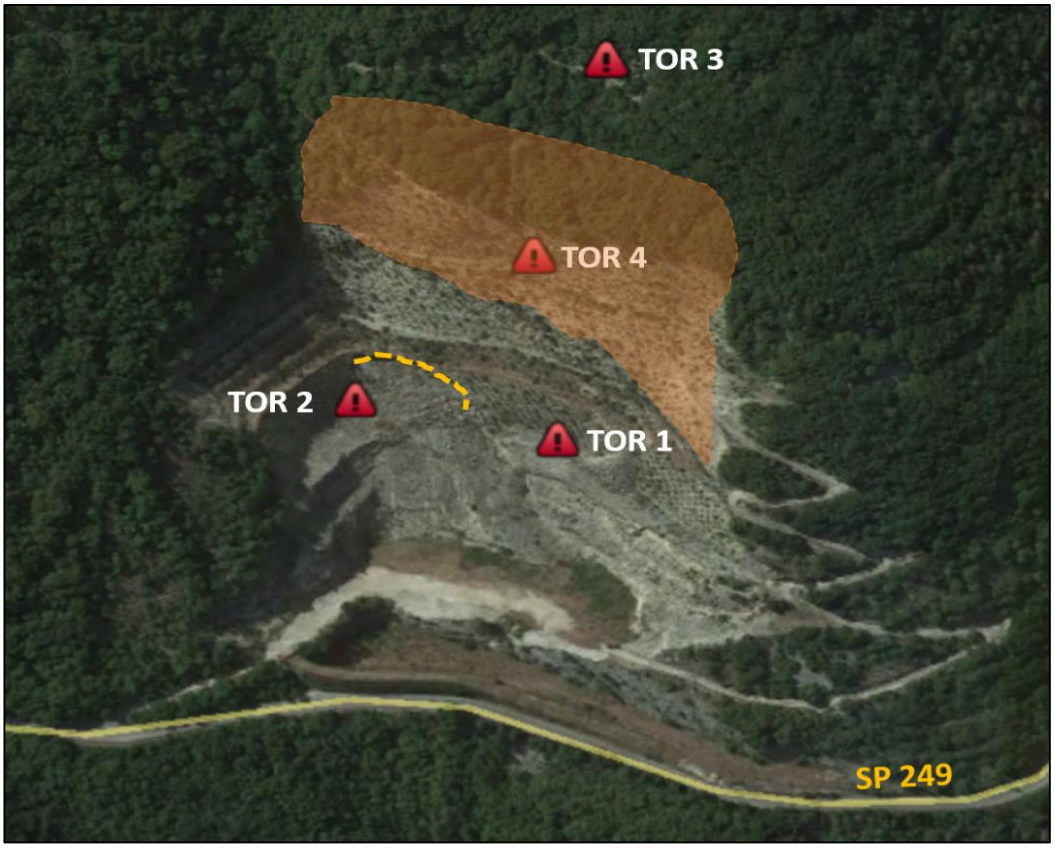

Figure 11 – Photograph of the Torgiovannetto quarry area, on Mount Subasio slope, location of the seismic network, composed by 4 stations, and contour of the rockslide. The yellow dashed line signals the detachment zone for the 2005 minor event. The gravitational instability threatens the road (SP 249) carrying traffic from and to Assisi.

Each station is equipped with a SARA 24bit A/D converters (SL06) coupled with a S45 tri-axial velocimeter sensor with a natural frequency of 4.5 Hz and transduction factor of 78 V/m/s.

Every sensor was placed on a concrete base with supporting plinth, isolated from the exterior in order to attain protection from severe weather. Battery supply and digitizer, connected to the sensors through a connector cable, were housed in a separate case. A covering sheet coated all the equipment (Figure 12).

Figure 12 – Visualization of one of the four seismic stations. The grey box contained digitizer and electrical battery supply, sensor was settled on a concrete base protected from the outside by means of a reinforced manhole.

Instruments response is flat down to 2 Hz, with an upper-corner frequency of 100 Hz. All of them used Global Positioning System (GPS) receivers for time synchronization; data were recorded in continuous mode at 200 Hz sampling frequency, as the best compromise between signal resolution and data storage. The Nyquist sampling theorem says we should sample with a frequency that is more than twice the highest frequency of interest so the choice of this sampling rate derived from the compromise between maintain limited the amount of data acquiring in continuous mode and obtain information concerning high frequencies (characteristic of microcrack) at least up to 100 Hz.

The electric power supply for the sensors came from a set of four 12V-60A batteries for each stations that needed to be substituted every 40 days to recharge them and download the data stored in the digitizer. Unfortunately, given the orientation towards NW of the slope, was not possible to use solar panels to recharge batteries; moreover the panels were likely to be destroyed due to falling blocks. Data acquisition was continuous for 210 days from 07

December 2012 to 03 July 2013 except for some short intervals due to the batteries change. Table I and Table II shows a summary statement of each station.

Station Code	Digitizer	Sensor	Power supply	Lat (°N)	Lon (°E)	Sampling frequency (Hz)
TOR1	SL06 24 bit	SS45 4.5 Hz	4 batteries 12V-60A	43.077305	12.641280	200
TOR2	SL06 24 bit	SS45 4.5 Hz	4 batteries 12V-60A	43.076983	12.642637	200
TOR3	SL06 24 bit	SS45 4.5 Hz	4 batteries 12V-60A	43.075848	12.641042	200
TOR4	SL06 24 bit	SS45 4.5 Hz	4 batteries 12V-60A	43.076567	12.641422	200

Table I - Technical characteristics and location of seismic stations.

Station Code	Start recording	Stop recording	Interruption (missing data)	Data quality
TOR1	06.12.2012 18:00:01	04.07.2013 18:00:00	20.12.2012 12:00:01-21.12.2012 00:00:00 15.01.2013 00:00:01- 15.01.2013 06:00:00 01.04.2013 00:00:01- 04.04.2013 00:00:00 04.06.2013 00:00:01- 06.06.2013 12:00:00	97%
TOR2	06.12.2012 18:00:01	04.07.2013 18:00:00	20.12.2012 12:00:01-21.12.2012 12:00:00 15.01.2013 00:00:01- 15.01.2013 06:00:00 01.04.2013 00:00:01- 04.04.2013 00:00:00	98%
TOR3	06.12.2012 18:00:01	04.07.2013 18:00:00	20.12.2012 18:00:01-21.12.2012 00:00:00 15.01.2013 00:00:01- 15.01.2013 06:00:00 01.04.2013 00:00:01- 04.04.2013 00:00:00 03.06.2013 00:00:01- 04.06.2013 00:00:00	98%
TOR4	06.12.2012 18:00:01	04.07.2013 18:00:00	20.12.2012 18:00:01-21.12.2012 00:00:00 01.04.2013 00:00:01- 04.04.2013 00:00:00 01.06.2013 00:00:01- 06.06.2013 18:00:00	96%

Table II – Working period and data quality of the four seismic stations.

As we will see in the next few chapters the entire dataset will be analysed through several technique in order to reach three different targets:

- Detection, discrimination and location of seismic signals
- Characterization of the sliding wedge (surface velocity and thickness of the sliding wedge)
- Site effect evaluation

2.1.2 Data

Data format of the seismic records retrieved from SL06 is miniSEED ('Data-only' volume); nevertheless, this format was mainly designed for the exchange of geophysical data and not for analysis so they had to be converted into SAC (Seismological Analysis Code; Goldstein et al., 2003; Goldstein and Snoke, 2005) format, more suitable for elaborations. The conversion was performed in Matlab with **mseed2sac** code. Data set, for each station, is split in 6-hr sections files (4 files/day) with $t_{start} = t_0$ =00:00:01; 06:00:01; 12:00:01; 18:00:01 to synchronize the file start at all the stations. The size of each file is equal to 16.876 Kb. Traces are displayed by using any software package for interactive visualization of earthquake seismograms such as SeisGram2K Seismogram Viewer (Lomax and Michelini, 2009, http://www.alomax.net/software) or Geopsy (Geophysical Signal Database for Noise Array Processing; http://www.geopsy.org ; Figure 13).

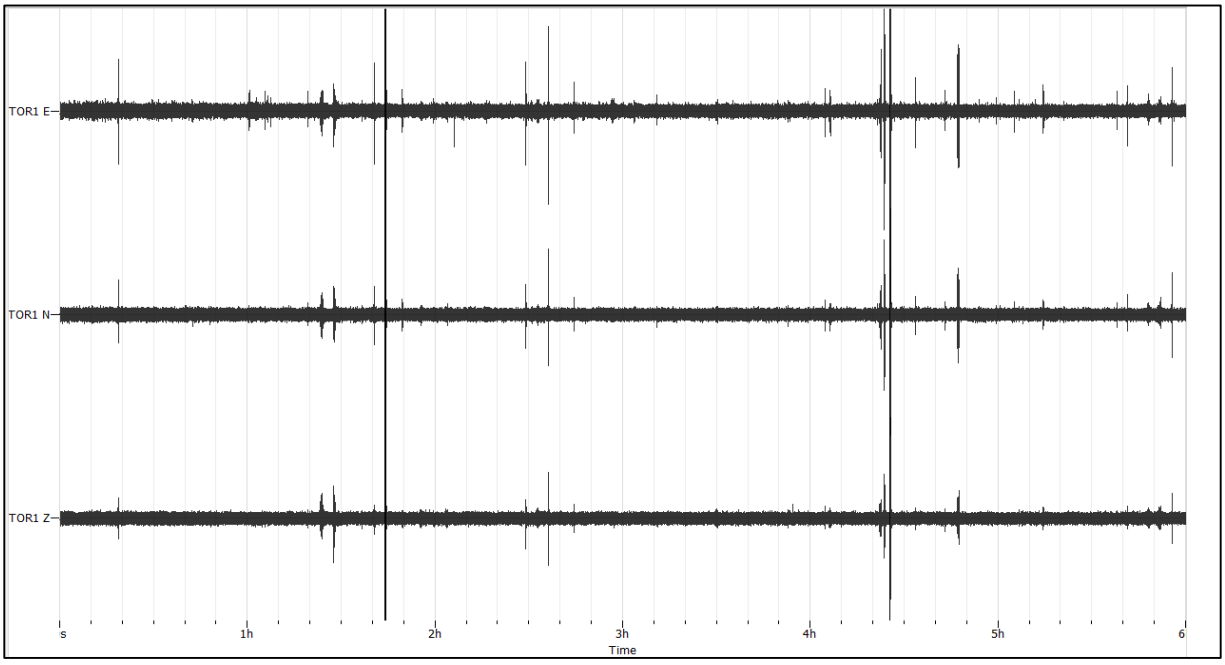

Figure 13 – 6-hr section recorded between 12:00:01-18:00:01 at TOR3 for the three component UD (SHZ), NS (SHN) and EW (SHE).

For each station, three separate files are generated, which correspond to the north-south (SHN), east-west (SHE) and vertical or up-down (SHZ) components of ground velocity. The amplitude (y-axis) is expressed in counts, x-axis express time.

For further information about SAC format consult the IRIS website (https://ds.iris.edu/files/sac-manual/manual/file_format.html).

CHAPTER 3 - METHODOLOGY

3.1 Characterization and monitoring of landslides: geophysical approach

Up to now, geophysical prospecting approach for the reconnaissance and characterization of landslides have been hindered, especially because these kind of methods provide images in terms of physical parameters that are not directly linked quantitatively to geological and mechanical properties required by geologists and geotechnical engineers (Jongmans and Garambois, 2007).

On the other hand, such mapping methods as remote sensing or aerial photography, are limited to providing surface information, and intrusive methods, like boreholes and penetration tests, provide subsurface data only at discrete locations. Over the last fifty years geophysical techniques have been successfully applied to landslide analysis, even if some studies (e.g., Fell et al. (2000)) evidenced that few landslide conditions are suitable for this purpose. Although a clear relationship between geophysical parameters and geological/geotechnical properties is often still unclear, these methods now appear as major tools for investigating and monitoring unstable slope masses (Pilz et al., 2013).

Several geophysics methods were applied to various types of landslides for slope varying from a few degrees (earth slide) to vertical (rock fall). Regardless of the geological, structural and geomorphological background, ground modifications due to a landslide could generate changes of the geophysical ground parameters that can be used to map the landslide body and to monitor its movement.

Geophysical methods will be briefly presented here, more detailed reviews on geophysical application can be found in various introductory textbooks (Kearey et al., 2002; Milsom, 2003; Schrott et al., 2003). Table III contains a short summary of the main advantages and disadvantages of geophysical methods compared to standard geotechnical approaches.

	ADVANTAGES	DISADVANTAGES
GEOPHYSICAL METHODS	• Non-invasive • Applicable to large areas • Relatively low cost • Provide spatial or volumetric information on subsurface structure and property variations	• Decrease of resolution with depth • Non-uniqueness of solution for data inversion • Interpretation • Indirect information

Table III- Main advantages and disadvantage of geophysical methods compared to standard geotechnical approaches.

The penetration depth of the surveys goes from 3 m to 400 m and the targets are mainly location of the vertical and lateral boundaries of a moving mass, mapping of its internal structure, detection of discontinuities and shear surface, and investigation of hydrological regimes.

Geoelectrical methods are the ones most commonly used for collecting information about the groundwater system (Cassinis et al., 1984; Bruno et al., 1998). They include low frequency electromagnetic profiling (Caris and Van Asch, 1991; Schmutz et al., 2000), electrical tomography (Lapenna et al., 2003; Demoulin et al., 2003; Bichler et al., 2004; Chambers et al., 2010; Popescu et al., 2014), vertical electrical sounding (Agnesi, 2005), and spontaneous potential analysis (Bruno, 2000; Méric et al, 2006).

Only recently there have been some attempts to apply geophysical techniques to the investigation of movement in crystalline formations (Ferrucci et al., 2000; Bruno and Marillier, 2000; Brückl, 2001; Havenith et al., 2002; Supper and Römer, 2003; Donnelly et al., 2005; Méric et al., 2005). This is partly due to the difficulties of deploying geophysical sensor in rocky ground and taking measurements on steep slope.

Geoelectrical investigations of landslides are dominated by the use of 2D electrical resistivity tomography (ERT) that allow to determine the distribution of the subsurface electrical resistivity. This parameter is a physical property of the substratum, which depends mainly on porosity, water saturation, pore fluid conductivity and clay content. Landslide events are often related to precipitation and to the influence of underground water on slope stability (pore water pressure, change of water flow regime, saturation). Observing temporal changes of electrical parameters aids in interpreting subsurface processes but a strong contrast in resistivity between the layers overriding a more resistive bedrock is required to reveal the landslide structure (Chambers et al., 2010). A lot of investigation have been carried out on clayey landslides (Lapenna et al. 2003, 2005; Lee et al.,2008) but very few on rockslide (Batayneh and Al-Diabat, 2002; Méric et al., 2005; Bell et al., 2006; Schmutz et al., 2009) principally because of the electric conduction that affects the surface of clay minerals. Perrone et al. (2014) suggest the use of ERT during the various phases (pre-event, emergency and post-event) of a landslide disaster cycle.

The application of 3D ERT for landslide investigation is instead rare probably due to the greater complexity of survey design, field deployment, and data processing that is required relative for 2D imaging (Chambers et al., 2010). One of the few studies (Lebourg et al., 2005) used 3D ERT to characterize a section of the La Clapière landslide identifying deep-seated slip surfaces and related hydrogeological changes.

Self-potential (SP) measurements investigate the natural electrical potential that can be produced by electrochemical, mineral and electrokinetic effects (Reynolds, 1997), assessing potential differences between the pairs of electrodes connected to a high impedance voltmeter. If electrochemical processes are absent within a slope, changes in this value describe the generation of electric fields by fluid flows. At the Séchilienne landslide, Méric et al. (2005), show a good correlation between SP anomalies and the displacement rate curve; Lapenna et al (2003) highlight the correspondence of the lateral boundaries, reported using the SP tomography at the Giarrossa landslide, and the lateral limits indicated using ERT or through a geologic–geomorphologic section. Moreover, various attempts to apply SP approach to developing an early warning system of rainfall-induced landslides have been carried out (Hattori et al., 2011).

Electromagnetic (EM) methods are quick, easy and non-destructive, but need to be combined with other geophysical techniques for landslide investigation and are useful mainly in refining the geometrical limits identification of an unstable mass.

Ground Penetrating Radar (GPR) and propagation methods (seismic reflection or refraction and seismic tomography) are preferred for delineating the geometry of a landslide zone and identifying the sliding surface (Bogolovsky and Ogilvy, 1977; McCann and Foster, 1990; Jongmans et al., 2000; Glade et al., 2005).

In particular, seismic methods directly identify mechanical parameters. However, due to the high mechanical energy attenuation of clayey rocks, they normally require very strong energy sources. Conversely, it appears as a good choice for rockslide analysis especially when the slope affected by the movement is composed of hard rock. Unfortunately, seismic reflection requires a greater effort to deploy the geophone layouts, especially in the case of hard rock, making the technique time consuming and costly. On the other hand, this method shows a high potential for imaging the geometry of a landslide structure and is used in many processing tools. Generally the measures are carried out using P-wave energization (Bruno and Marillier, 2000; Ferrucci et al., 2000, Ogunsuyi et al., 2011) but Bichler et al. (2004) and Petronio et al. (2006) used also S-wave reflection profiles. Reflection seismic data and their interpretations are also recently presented by Malehmir et al. (2013), Lundberg et al. (2014) and Shan et al. (2014).

Wave velocities are generally lower in the landslide body than in the unaffected ground: this peculiar behaviour make the method applicable for landslide investigation (Beckler et al., 2011; Adamczyk et al., 2013, 2014). Both shear and compressional wave can be used for the

energization. There are two main approaches to interpreting seismic refraction data: General Reciprocal Method (GRM) (Palmer, 1980) and First Arrival Seismic Tomography (FAST) (Olsen, 1989; Pullammanappallil and Louie, 1994), depending on the complexity of the analysed structure.

However both seismic reflection/refraction and electrical tomographies are heavy to set up, require for some heavy processing tools to implement, and consequently are expensive and time consuming: passive methods skip those problems because require lighter instrumentation and easier processing tools.

Recently, considerable attention has been devoted to the use of seismic measurements as indicator of deformation within landslides and to locate fracture both in space and time. Technology and data interpretation of passive seismic applications for landslide and rockfall monitoring is still at the very beginning compared to earthquake or reservoir hydrofracturing monitoring (Arosio et al., 2015). This group of technique includes micro-seismic and nano-seismic (Joswig, 2008; Häge and Joswig, 2009). Instead of using an artificial seismic signal (sledge hammer, explosions, airguns, etc.) these methods use seismic (Amitrano et al., 2007; Walter and Joswig, 2009; Lacroix and Helmstetter, 2011) or acoustic (Bláha, 1996; Dixon and Spriggs, 2007; Arosio et al., 2009; Zaki et al., 2014) signals emitted by deformation processes by “listening” to ruptures. A recent paper (Zoppè G., 2015) pointed out that microseisms and acoustic emission show similar trend and have an evident correlation with precipitation. Spillman et al. (2007) worked on a dataset recorded by twelve 3-axial sensor on the Randa rockslide. The results were used to characterize the slope body. Vilajosana et al. (2008) integrated microseismic data from two 3-component seismic station with video images to obtain information on rockfall size and location of impacts.

Blikra (2008, 2012) and Nielsen (2009) used eight 3-axial geophones to perform event detection and classification at the Åknes rock slope.

Amitrano et al. (2010) analysed data from five 3-axial high-frequency geophones installed in shallow bore-holes and three 3-axial low-frequency geophones on surface to evaluate the effects of freeze-thaw cycles on the fracturation and crack development and propagation within the rock block. Séchilienne monitoring network (, composed of three seismological stations and three arrays of vertical sensors, provided useful information about the application of passive seismic for the location of seismic signals detected with a semi-automatic procedure and underline the difficulties to established threshold for early warning systems based only on these kind of monitoring technique (Helmstetter and Garambois, 2010).

Walter et al. (2012) installed 3 seismic arrays and recorded a major rockfall occurred 5 km away from the network: the system also recorded a set of precursory events referable to minor rockfalls and fracture propagation.
Super-Sauze and Valoria (Tonnellier et al., 2013) reported two other interesting case studies for seismic sources in clay-shale landslides. One of the main results obtained in this context is the positive correlation between microseismicity, rockfall activity and landslide displacement rates. Lately, attention has also focused on studies of the site directional properties of the noise signals and of its H/V investigating the dynamic response of landslide prone slopes to seismic shaking and searching for a directional resonance connected to potential sliding directions (Del Gaudio et al., 2013).
All authors referred above agree on the need to use multiple techniques together to get a complete picture of the investigated situation.

3.2 Methods

In this work, the analysis of passive seismic data aims at three main objectives: (1) to obtain information on the elastic properties (seismic velocities) of the subsoil, which may help constraining geometry and thickness of the unstable rock mass; (2) to investigate whether such properties vary through time, thus indicating a change in the stress state and/or weathering conditions (fluid content and microfracturing) of the investigated volume, and (3) to detect small-amplitude transient signals possibly related to either rock-falls or micro-cracking phenomena. Objectives 1-2 above have been addressed analysing the seismic noise wavefield, in terms of its overall amplitude (Root Mean Sqaure - RMS), polarization (Horizontal-to_Vertical_Spectral-Ratio - HVSR) and correlation properties (Noise Correlation Function - NCF). Objective (3) has been addressed using a simple procedure (Short-term-average over Long-term-average - STA/LTA) for the detection of transient signals, testing the ability of the network to locate these signals, and adopting a specific procedure for improving the detection capabilities. The following sections describe the state of the art for each of the implemented procedures and explain in detail the goals that I will try to achieve in the present work. For further information on the mathematical theory of the different applications, which is beyond the scope of this text, the reader is referred to the cited literature.

3.2.1 Horizontal to Vertical Spectral Ratio (HVSR) and polarization analysis

Early studies aimed at retrieving information about the subsoil from tremor spectra recorded at a single station can be found in Kanai (1957) but for the first introduction of the HVSR technique Nogoshi and Igarashi (1970, 1971) must be mentioned. The method, become widespread after Nakamura (1989) as a fast tool to interpret records of microtremors, and it has been widely used in microzonation studies for site effect investigation at a large number of urban areas (e.g., Lermo and Chávez-Garcìa, 1994; Duval and Vidal, 1998; Duval et al., 2001; Field, 1994; Field et al., 1995; Chávez-Garcìa and Cuenca, 1995) and also for the study of sedimentary basins to identify the variation of resonance frequency with depth of the bedrock (e.g., Al Yuncha and Luzòn, 2000; a review for both these applications is also reported in Mucciarelli and Gallipoli (2001)).

The technique is based on the ratio of the horizontal to vertical components of ground motion and it only requires a 3-component (3C) sensor to acquire data. In Nakamura (1989) the base hypothesis is that microtremor energy consists mainly of Rayleigh waves, and that site effect amplification is due to the presence at the surface of a soft soil layer overlying a rigid half-space. One of the striking features of the HVSR ratio is its stability in time, documented in many papers (e.g. Volant et al., 1998; Bour et al., 1998).

Various studies analysed the composition of microtremors: most papers, and the most famous among them (Field and Jacob, 1993, 1995; Lachet and Bard, 1994) assumed that they are mainly Rayleigh surface waves; this position is in partial agreement with Arai and Tokimatsu (2004) and Cadet (2007) that also obtained good result using surface wave ellipticity in inversion schemes including Love surface waves. Actually it is accepted that the dominant contributions to ambient vibrations come from surface waves, although the exact composition may change depending on the specific site. On the other hand, Herat (2008) successful based his Matlab tool (ModelHVSR), for the inversion of the H/V ratio, on body waves ellipticity while Lermo and Chávez-Garcìa (1993) applied Nakamura's technique using the S-wave part of earthquake records for three cities in Mexico. Other studies have shown that the ambient noise wavefield is the result of the combination of unknown fractions of both body and surface waves (Bonnefoy-Claudet et al., 2006; Sánchez-Sesma et al., 2011). Although the value of the amplification factor is merely representative of the real site amplification (Pilz et al., 2009), peaks in the spectral ratio are a good indicator of the fundamental resonance frequency of the site, especially the ones with strong impedance contrast. The HVSR curve allows gaining additional information about the underlying

velocity profile at the site, especially when a strong different shear wave velocity exist between the shallow layer and the bedrock (Malichewsky and Scherbaum, 2004).
Main application of this technique on landslide concerns the possibility to reconstruct the geometry of the sliding mass and to detect the depth of the shear surface with a good approximation using the relationship between frequency (F), shear wave velocity (V_s) and thickness of the shallowest depth (H):

$$H = \frac{V_S}{4*F} \quad (1.1)$$

This approach was used, for instance, on three landslides located in the Southern Apennines: Gallipoli et al. (2000) integrated the high-resolution electric tomography and sonic surveys with the spectral analysis of microtremors. The results indicate a good agreement of the sliding surface detected by H/V inversion with that derived from the other techniques.
Havenith et al. (2002), Méric et al. (2007) and Gaffet et al. (2010) estimated the resonant frequencies of an unstable rock slopes from H/V measurements, and used those results for deriving the rupture surface depth. However, this technique is not suitable everywhere: Giocoli et al. (2015) highlighted the scarce results obtained with HVSR for the detection of the sliding surface because of the negligible impedance contrast between the Quaternary continental deposits and the material of the Verdesca landslide (Southern Apennines, Italy).
Slightly different application was carried out by Pilz et al. (2013): in this case, HVSR was successfully applied under pronounced topographic conditions to map lateral and vertical changes in the shear-wave velocity of the shallowest soil layers of a potential future landslide and the analysis of HVSR polarization was proposed for the detection of unstable section of the slope. The influence of the landslide body on seismic response directivity is also demonstrated in Del Gaudio and Wasowski (2007) and Del Gaudio et al. (2008, 2011, 2013).

3.2.2 Noise Cross-correlation Functions (NCF) and coda wave interferometry

Many recent studies have shown that cross-correlating the ambient noise signal recorded at two surface locations A and B over a period of time, is possible to extract the Green's function or impulse response associated with the medium in between the two sites. In other words, the cross-correlation of the traces recorded at sites A and B is equivalent to the wavefield that would be observed at B if there were an impulsive source at A, assuming that the noise source distribution is spatially homogeneous around the stations. This equivalence, early individuated by Aki (1957) and Claerbout (1968), has been successively

exploited and generalised (e.g. Shapiro and Campillo, 2004; Snieder, 2004; Wapenaar, 2004). The use of ambient noise offers the possibility to work without earthquakes sources or energization near the array: it offers the possibility of imaging without a source (passive imaging) estimating seismic structure even beneath aseismic regions. The result of days, months or years of stacked correlation recorded from pairs of receivers at various distances, is often called "a noise correlation function" (NCF; Roux et al., 2005; Sabra et al., 2005 Seats et al., 2012). From these NCFs, estimates of the surface wave dispersion can be obtained and then inverted to obtain 1-D velocity estimates between the stations. When applying such analyses to an entire array, implementing every combination of station, 2-D and 3-D velocity structure (both on regional and continental scale) are imaged (Shapiro et al., 2005; Lin et al., 2007; Renalier et al., 2010; Yang et al., 2007).

More recently, NCFs have been used for monitoring very small temporal changes in a medium's velocity structure (Sens-Schönfelder and Wegler, 2006; Pandolfi et al., 2006; Brenguier et al. 2008a, b; Baptie, 2010; Hadziioannou, 2009, 2011, Nakahara, 2014). This procedure is based on the analysis of the so called "coda waves", i.e. those portions of the NCF at lag times which are at least twice the travel-time of S-waves. Coda waves are related with multiple scattering from the small-scale heterogeneities within the Earth.

As the scattered waves that form the coda of NCFs, result from variable interferences between numerous waves of different types emitted by different sources, they do spend longer time in the medium once compared to other waves (Figure 14), so that the former are more sensitive to weak changes in propagation velocity.

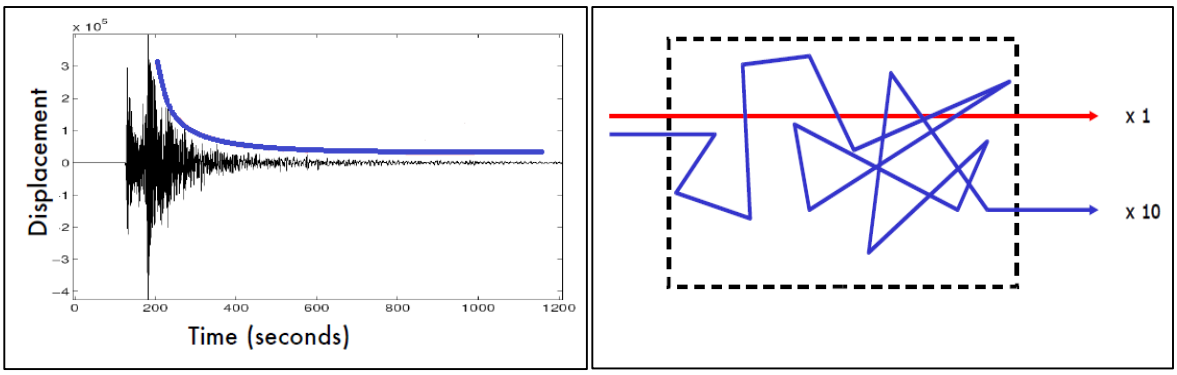

Figure 14 – On the left, coda-waves of an earthquake and, on the right, their path in the medium (blu lines) compared to direct waves (red line).

As a consequence, ambient-noise cross-correlation can be used to monitor slight relative changes in seismic speeds, with precision as small as 10^{-4}. Velocity drops observed in this manner have been proposed to be precursories of volcanic eruptions and landslides.
Among the others, this technique was also used to detect mechanical changes in an active landslide, where failure is expected, by monitoring shear wave velocity variations (Mainsant, 2012).

Possible temporal variations of the propagation velocities manifest themselves as a time shift in the coda of the NCFs retrieved over subsequent time intervals.
Let $u_0(t)$ and $u_1(t)$ be the NCFs retrieved at time zero and at a certain time after a velocity change has occurred. Due to velocity perturbation, the coda waves of $u_1(t)$ will exhibit a time shift with respect to the corresponding signal portion of $u_0(t)$. That time shift will become progressively larger for increasing lag times, as coda waves at large lag times have travelled larger distances, therefore accumulating longer delays.
This properties is quantified by measuring the cross-correlation function between the two signals over subsequent time windows of length 2T centered on t.
For two signals of duration T, the correlation of the signal $u_1(t)$ at $\overrightarrow{r_1}$ and $u_2(t)$ at $\overrightarrow{r_2}$, which evaluate the resemblance between them, and when these signals are similar enough, the time delay that separates them, is defined classically in the time domain as

$$\boldsymbol{R(t_s)} = \frac{\int_{t-T}^{t+T} \boldsymbol{u(t')\tilde{u}(t'+t_s)dt'}}{\sqrt{\int_{t-T}^{t+T} \boldsymbol{u^2(t')dt'} \int_{t-T}^{t+T} \tilde{u}^2(t')dt'}} \tag{1.2}$$

For each time window, the percentage of velocity variation dV/V can be computed from the lag-time t_s at which the above equations attains maximum value (Ratdomopurbo and Poupinet, 1995):

$$\boldsymbol{t_s} = -\frac{\Delta V}{V}\, \boldsymbol{t} \tag{1.3}$$

Under the hypothesis of a uniform velocity variation, the plot of lag-time corresponding to the maximum of the cross-correlation per time window versus time shows a linear relationship, where the mean velocity perturbation is given by its slope. The velocity variation can thus be computed by fitting a straight line to t_s versus t.

3.2.3 Seismic Signals Detection and Classification

In the processing of the continuous microseismic data, a time-picking method able to detect the most important events that is fast, accurate, and automatic is highly desirable.

A great variety of methodologies based on the amplitude, the envelope or the power of the signal in time domain, or on frequency domain content of seismic signal, for single as well as multi-component recordings, have been proposed to automate the event detection. (Chen and Stewart, 2005; Wong et al., 2009; Hafez and Kohda, 2009; Rodriguez, 2011; Akram, 2012).

The simplest, and widely used method in the microseismic analysis is based on the STA/LTA trigger.

The short-term-average over long-term-average (STA/LTA) filter (Allen, 1978) have been subsequently reviewed and modified but the first form still remain broadly used.

The ratio between the two moving-time windows continuously evaluates the absolute amplitude of the seismic signal. The trigger is declared every time that the pre-set threshold, calculated as the ratio between the short time window (STA) and the long time window (LTA), is reached.

One of the benefits of the STA/LTA method is that high amplitude signals may not trigger if there is no significant amplitude increase: the STA and LTA values will both be high, resulting in an STA/LTA ratio close to 1, avoiding falsely trigger on noise signals.

One of the goals of the research deal with the setup of a near-real-time detection and "picking" of rockslide signals to count them and interpret the precursory patterns occurring on the site. The purpose is to interpret the data recorded step by step to have an overview of the global evolution and of the rock mass behaviour before collapsing. Considering that the noise level of Torgiovannetto site is quite low, the use of a simple STA/LTA trigger appears reasonable in order to detect as many seismic events as possible without losing events with low amplitude. The parameter settings (STA and LTA length, the value of amplitude threshold, the value of pre and post-trigger) represent the most important part of this section because the seismic signal obtained depends from that (Figure 15); the STA measures the 'instant' amplitude of the seismic signal while LTA takes care of the current average seismic noise amplitude: the modification of their length would led to identify different type of events (Trnkoczy, 2002). The length of the STA window is suggested to be long enough to cover the expected seismic event avoiding to be too short otherwise the averaging will not function properly. The length of LTA window should cover the expected fluctuation of seismic noise. Obviously, larger threshold will identify less events, hence the amount of data becomes easier

to manage. Also the value of pre and post-trigger should be chosen maintaining their value to avoid that the post trigger of an event overlap the pre-trigger of the next event.

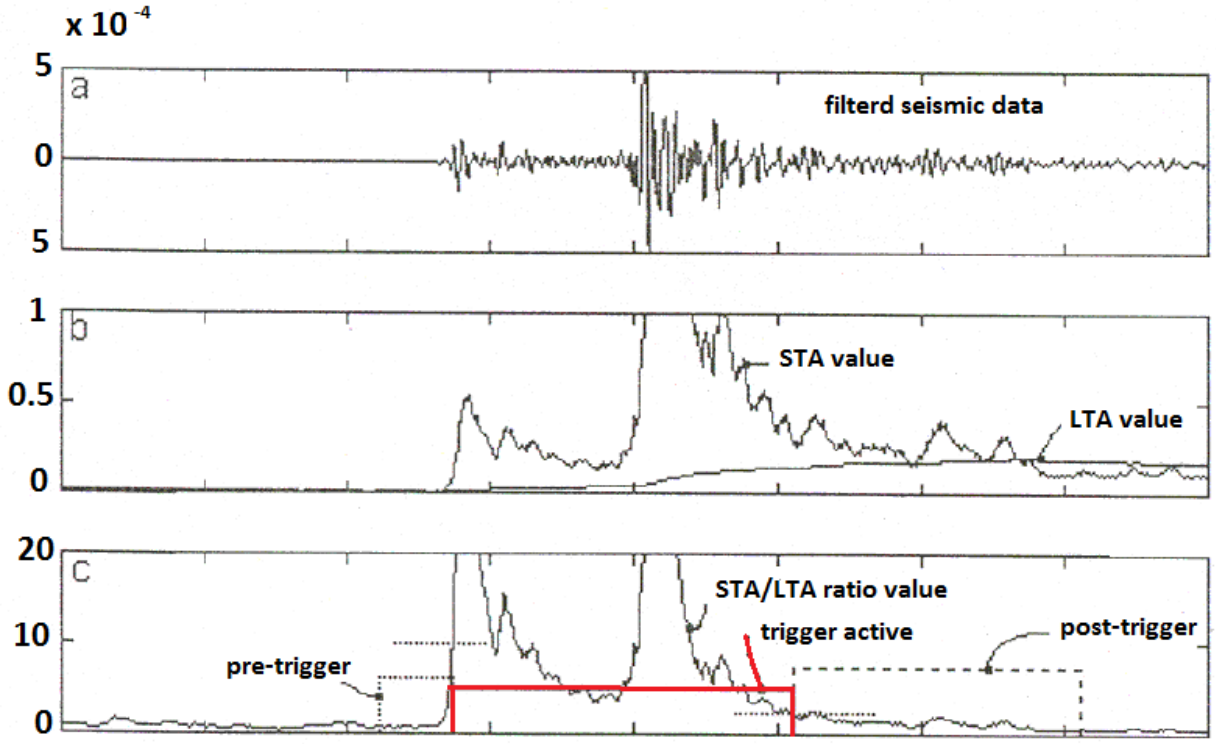

Figure 15 – Function and variables of STA/LTA trigger calculations (modified from Trnkoczy, 2002).

In literature**,** Helmstetter and Garambois (2010) at Séchielienne recorded data in triggering mode using a STA/LTA threshold; DeRoin and McNutt (2012) use STA/LTA trigger implemented in *Earthwarm* system to detect rockfalls on the Augustine Volcano slopes.

Additionally, automatic classification of the events into different group using their peculiar characteristics may be feasible (Helmstetter and Garambois, 2010; Lacroix and Helmstetter, 2011). It is possible to distinguish them in five main subcategories:

- micro-crack
- rock-fall (artificial or natural ones)
- local and regional earthquake
- multiple events
- transient (noise)

The argument is extensively discussed in Levy et al (2011) and Iriantoro Putra (2012) to select and classify events from continuous recording on a prone-to-fall rock column at

Chamousset. In these cases, classification was achieved using the waveform shapes of the seismograms, their amplitude, frequency spreading in the spectrogram, duration of events and also polarization analysis.

3.2.4 Automatic/Semi-automatic location of detected events

Over the last couple of decades, a great leap forward for the location of microseismic events has been made thanks to the development of the monitoring of industrial processes such as mining, hydraulic fracturing, carbon sequestration, geothermal operations and underground gas storage in order to increase efficiency and optimize operations (e.g. Swanson et al., 1992; Daku et al., 2004; Drew J.E., 2005; Eaton et al., 2014; Goertz-Allman et al., 2014). In these cases the monitoring and location must be in real-time to let operators check the pattern of seismicity related to production activities.

The same purpose can be applied to landslides monitoring system to identify where and when the rock mass is undergoing elastic failure. Thus, the concentration of the microseismic events, allow the recognition of hazardous situations and provide an early warning.

There are three main techniques for locating microseismic events: triangulation, hodogram and semblance based techniques. Triangulation uses P-wave and/or S-wave arrival time picks from numerous stations; the hodogram technique exploits the polarization of the P-wave phase from particle motion analysis to retrieve the azimuth and dip of the wave propagation (Jones et al., 2010); the semblance technique (Duncan and Eisner, 2010; Staněk et al., 2015) uses the multichannel coherency from a distributed network and does not need arrival time picking. All these approaches require a velocity model of the area.

In summary, the calculation of the exact location of transient event requires:

- at least three sensors (especially if location is carried out using triangulation technique)
- know the exact location and orientation of all monitoring sensors
- time synchronization of the data acquired by the different stations
- accurate arrival time picking (Eisner et al., 2010)
- have a detailed velocity model (Usher et al., 2013; Gesret A., 2015)

Clearly, arrival times of waves typically will first be detected at the sensor which is nearest to the source. A delay will be observed on all other receivers which represents the additional distance that is travelled from the source to receivers which are farther away.

Roux et al. (2008) used a two-step grid search in the parameter space to retrieve four clusters of activity at Glacier l'Argentière (Mont Blanc) that show that the fracturing process was focused in small zones and is not uniformly over the glacier. Lacroix and Helmstetter (2011) also used a beam-forming method to locate rockfalls and microearthquakes at Séchilienne rockslide taking into account the 3D nature of the landslide velocity and evaluating both the horizontal and depth error: the higher correlation retrieved for microearthquakes suggested that the method works better for point sources.

Bancroft (2009) proposed an alternative approach based only on the use of the first arrival times to estimate the source location with an array of receivers in a well.

Castellanos and van der Baan (2013) treated the problem with a two-step procedure to locate the microseismic events detected near a mine. First, they applied a grid search on the parameter space, then a cross-correlation to assess waveform similarity between events and identify doublets and multiplets and finally they used the double-difference method to obtain highly accurate relative event locations. This technique showed a good error reduction for the relocation of clusters of similar earthquakes.

CHAPTER 4 – APPLICATION

4.1 Seismic characterization of the site and of the sliding wedge

4.1.1 RMS

The main focus of this section is to characterize the seismic noise wavefield in terms of its amplitude and spectral content, with the final goal of verifying whether a correlation exists between the time evolution of these attributes and rockfall-microcrack events.

In order to test the site and the sensor resolving ability in terms of signal-to-noise ratio (SNR) I compared the power spectral densities of mine recordings to the maximum and minimum seismic noise spectra (in terms of velocity, vertical component) according to the standard models of the USA Geologic Survey (USGS). Peterson curves (HN: high noise; LN: low noise) express the seismic noise model retrieved from the spectral analysis of a great number of worldwide stations, and serve as a reference for discerning between noisy and quiet stations.

Figure 16 shows the power spectrum density (PSD) of the four stations' vertical component (SHZ), averaged over 6-hr intervals: various time sections are plotted with different colours to identify significant changes in noise level between day and night. Power spectra are obtained using a Matlab code which also includes correction for the instrument response down to a frequency of 0.2 Hz. They are calculated during a sample week (18.12.2012-24.12.2012) and compared to the average curves of minimum and maximum noise according to the Peterson model (1993). The red spectrum that diverges from the other is related to an earthquake occurred on 18.12.2012 at 13:57:54 with M=2.9, 20 Km SE of Assisi (lat 43.039 lon 12.886).

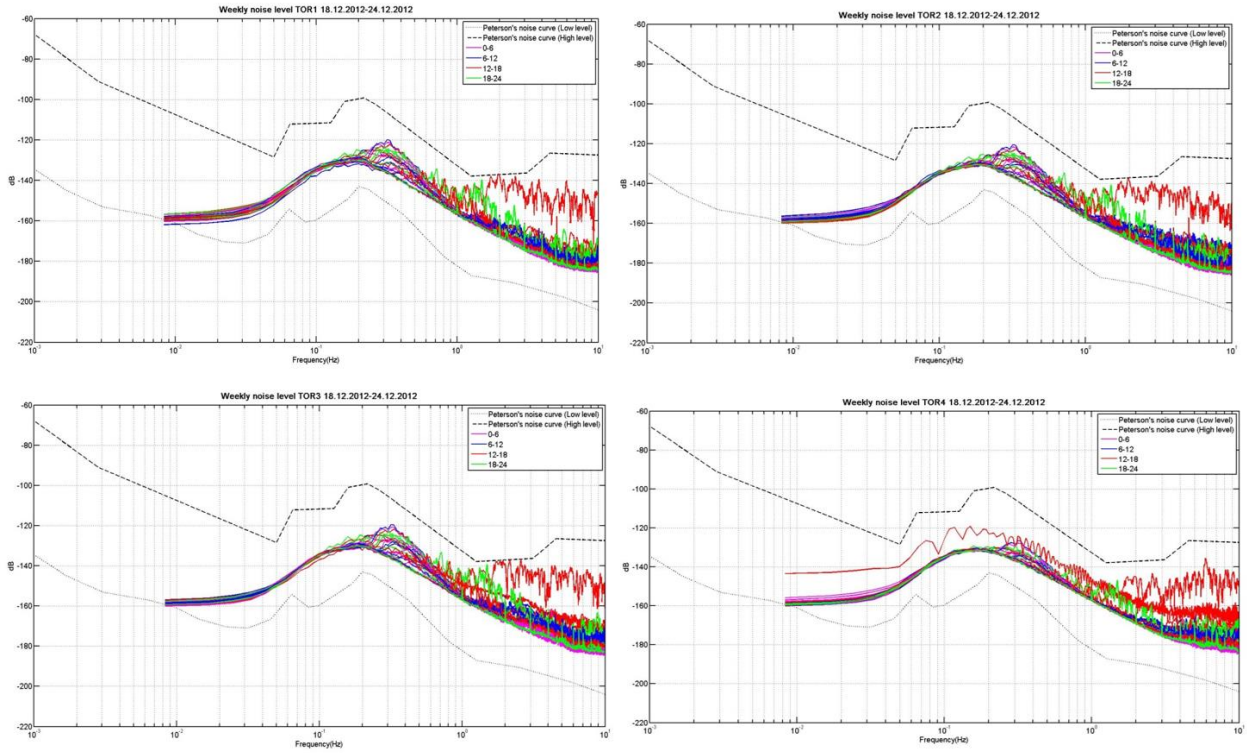

Figure 16 – PSD (Power Spectral Density, $(mm/s^2)/Hz$) – **Frequency** (Hz) graphs. Peterson curves (thick and thin dotted black line) and power spectra of the SHZ component for the four stations (TOR1, TOR2, TOR3, TOR4). Every colour referred to different time intervals (pink: 0-6; blue: 6-12; red: 12-18; green: 18-24).

The spectra have the same form regardless of the acquisition time and date and are entirely included in between the Peterson reference curves.

This analysis suggests that the site is suitable as test-site for the application of the passive seismic techniques because the signal does not exhibit large variations between different recording periods, and the overall noise level is rather low. I do therefore expect a significant resolving ability in the detection of transient events related to local microcracks, rockfalls, or earthquakes.

The very first step for the noise analysis concerns the evaluation of the time evolution of the seismic amplitudes over two frequency bands: 2-45 Hz and 20-100 Hz. Even if the manufacturer provides the acceptability of the value obtained with SS45 sensor down to a frequency of 0.2 Hz, the noise below 1 Hz is expected to be dominated by microseisms (i.e., signal related to sea climate), and therefore I preferred to exclude those frequencies from the analysis. On the contrary, the signal's amplitude at high frequencies is expected to be more representative of the occurrence of both microcracking activity (Wust-Bloch and Tsesarsky, 2013; Tonnellier et al., 2013), and rock-fall events.

The effective amplitude of seismic recordings was calculated as the median of the absolute value evaluated over sliding windows of 600 s (120000 sample points at 200 Hz), with a 50%

overlap so that two successive windows are separated by 5 min. After, I corrected the wrong data, mostly due to electronic problems, replacing these values with the overall average amplitude value, and finally removing the mean. The analysis of the signal acquired at TOR2 is omitted because of an electronic noise that frequently affected one or more components of the station.

This lack is not a big loss considering that TOR2 shows no significant HVSR peaks, indicating that this station is located on the compact rock (comparable to the bedrock in this case). Moreover that station is the farthest with respect to the sliding wedge so that I don't expect a significant variation in its amplitude values due to possible microcracking.

In the amplitude plots obtained by this process is almost impossible to detect any significant trend within any of the frequency bands considered. Except for some spikes, due to the presence of electronic transients or major earthquakes, the overall amplitude does not exhibit any major variation.

Special features of individual frequency band are:

- **2-45 Hz**: at a first glance, one can notice a slight increasing trend in the mean amplitude value starting around the last days of January. TOR4 shows the greatest mean amplitude value.

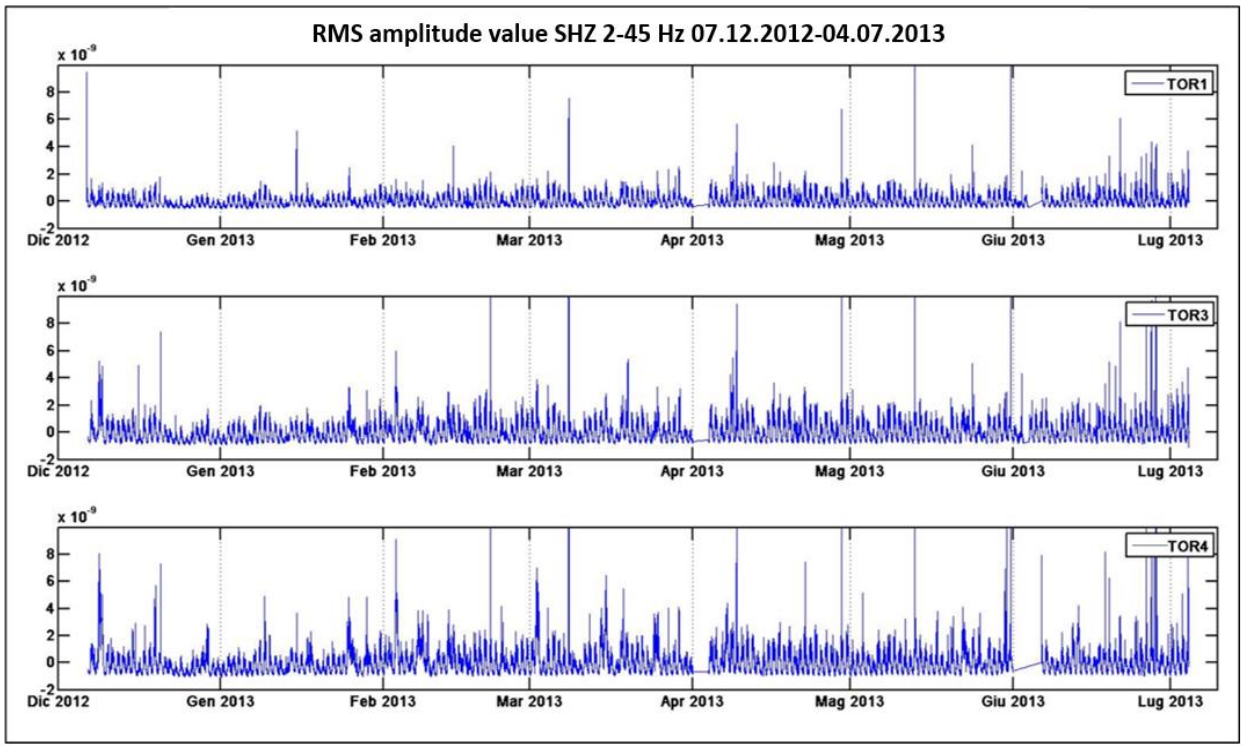

Figure 17 – Amplitude value in the 2-45 Hz frequency band from 07.12.2012 to 04.07.2013 recorded at TOR1, TOR3 and TOR4. TOR2 is omitted because of an electronic noise affecting one or more components starting on February, 2013.

- **20-100 Hz:** the amplitudes are generally lower than those recorded between 2 and 45 Hz but the number of transient peaks at TOR1 and TOR4 is substantially higher. Some periods (e.g. around December 15th, April 10th, and in the first and last days of June) show a higher peak concentration traceable at all stations (Figure 18, orange rectangles).

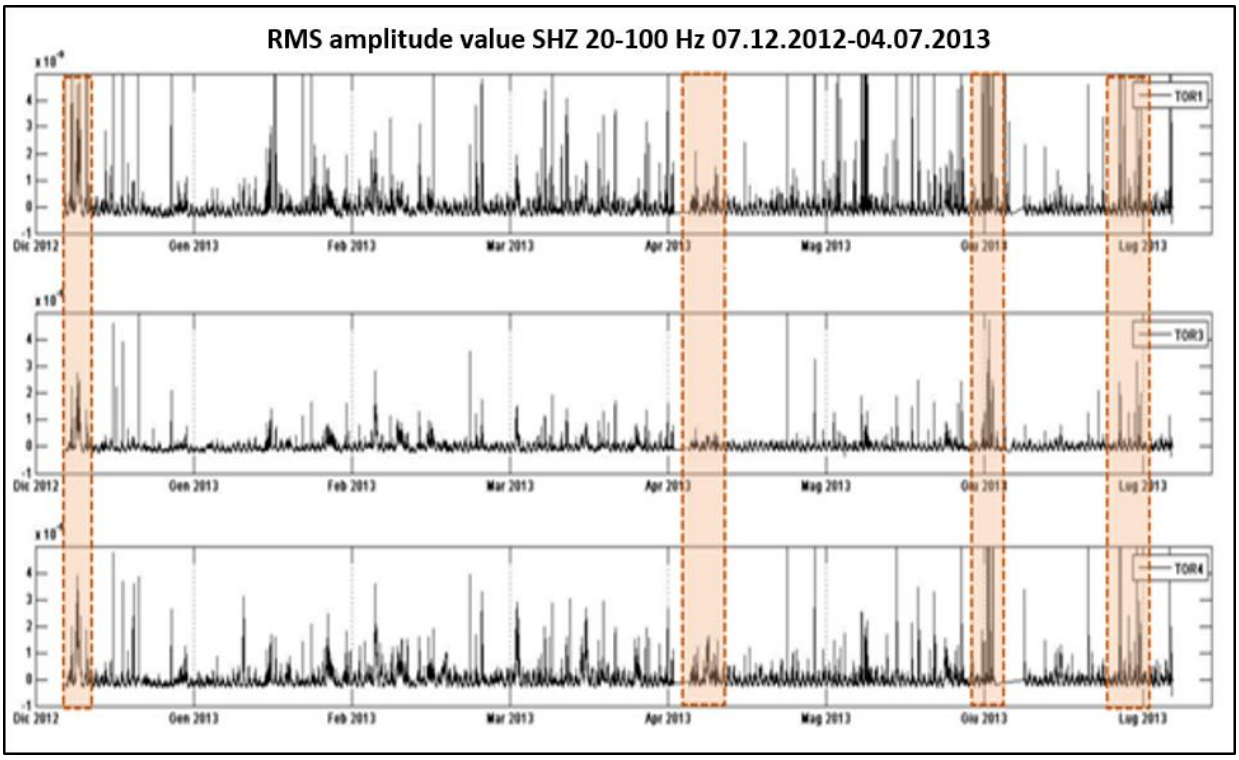

Figure 18 – Amplitude value in the 20-100 Hz frequency band from 07.12.2012 to 04.07.2013 recorded at TOR1, TOR3 and TOR4. See text for details.

Both in 2-45 Hz and in 20-100 Hz frequency bands, the zoom on shorter portions of the signal highlights a daily (24 h) and weekly modulation (Figure 19, Figure 20, 21: top images), with a significative drop of the signal amplitude during the nights and weekends and sporadical intervals with higher value. This pattern can be in great part attributed to anthropogenic effects, although meteorology can also play a role, at small scale, mainly for TOR3.

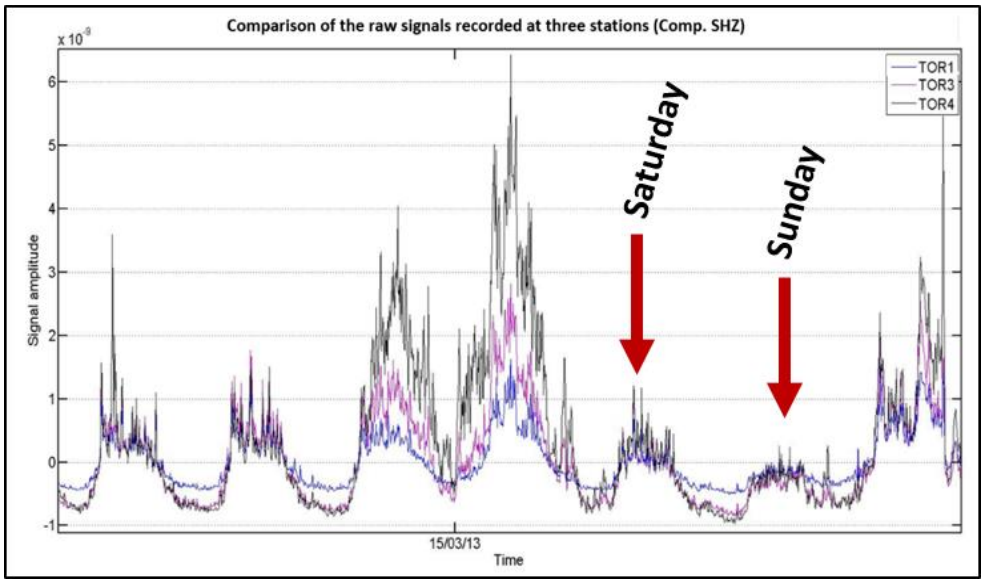

Figure 19 – Zoom on one week portion of the SHZ component of TOR1, TOR3 and TOR4. A clear 24 h modulation can be observed for all the acquisition sites.

In order to enhance the different noise variation at the four stations I proceeded integrating the data 24-hours windows with an overlap of 50% so that the resulting windows are separated by 12 hours. The data processing was performed separately for each components: SHE component shows the highest amplitude at every station. Results are reported in Figure 20 and 21 (middle images).

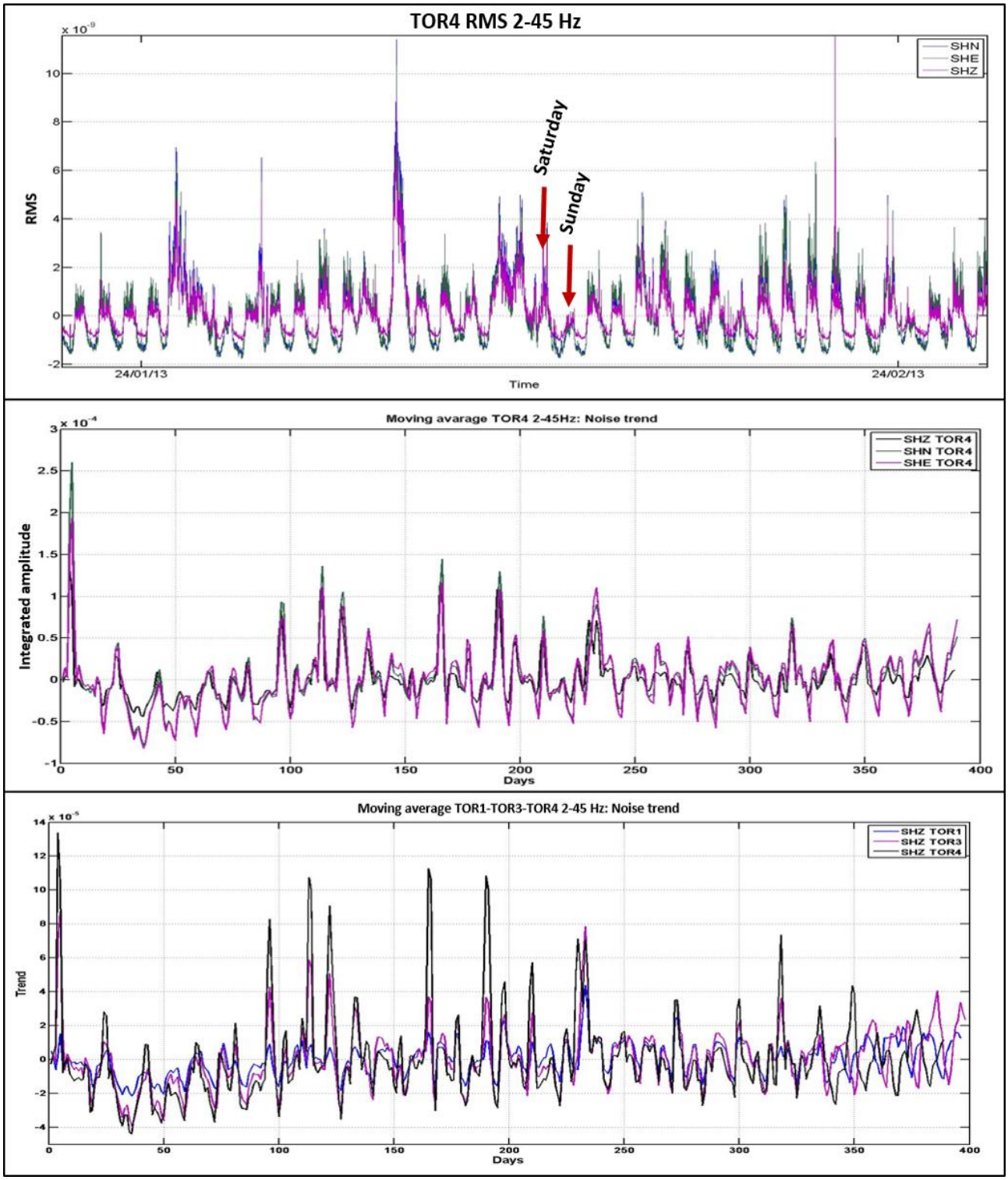

Figure 20 – Analysis of the RMS in the frequency bans 2-45 Hz. From top to bottom: (1) one month of the three motion component RMS recorded at TOR4; (2) integrated RMS value on TOR4 three motion component evaluated on 24-hours windows with an overlap of 50%; (3) same as (2) but only SHZ component for TOR1, TOR3 and TOR4.

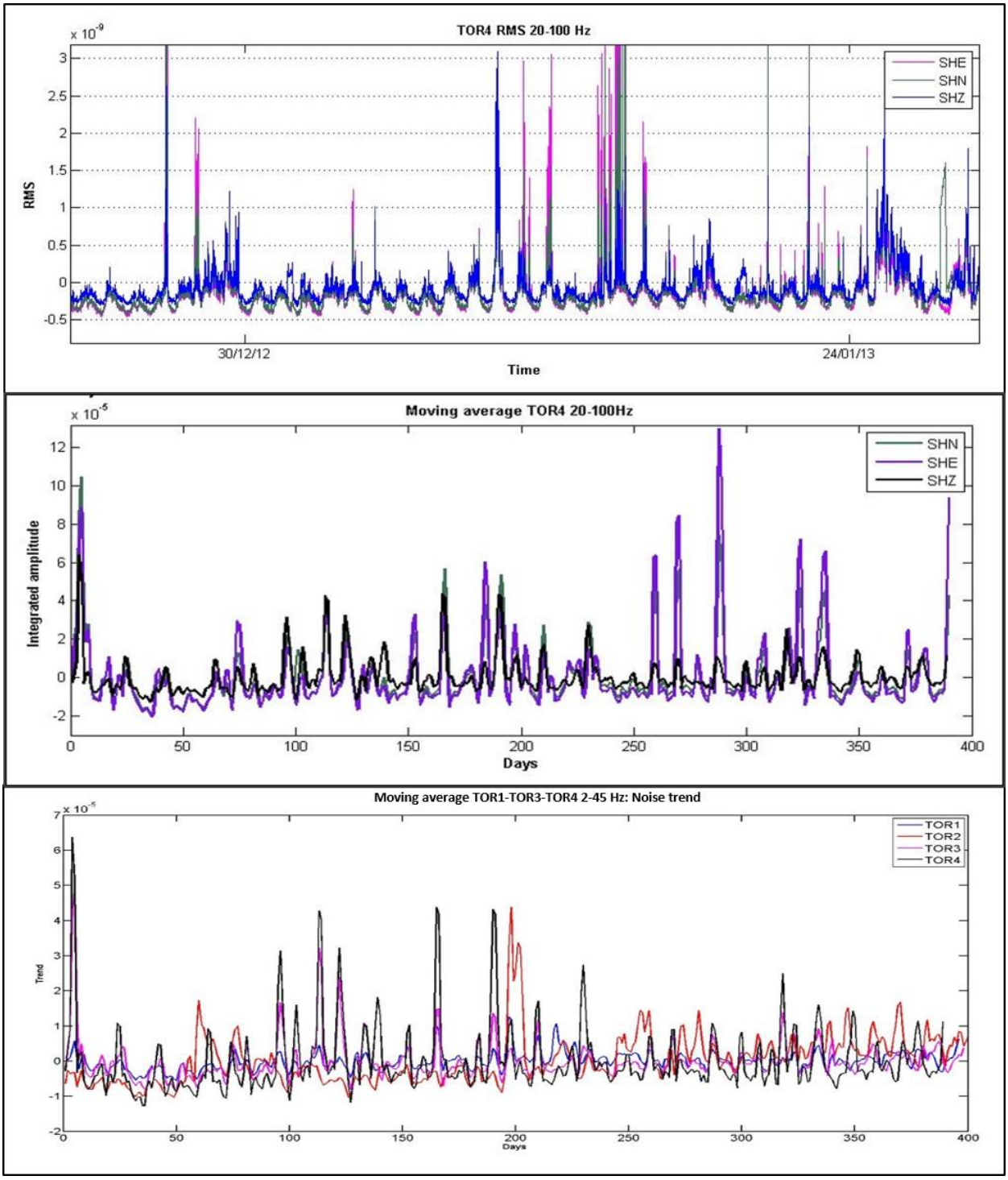

Figure 21 – Analysis of the RMS in the frequency bans 20-100 Hz. From top to bottom: (1) one month of the three motion component RMS recorded at TOR4; (2) integrated RMS value on TOR4 three motion component evaluated on 24-hours with an overlap of 50%; (3) same as (2) but only SHZ component for TOR1, TOR3 and TOR4.

Although more or less evident at the different locations, stations show a similar trend but, as I expected, the 24 h integrated amplitude recorded at TOR4, located on the landslide, shows higher peaks than that calculated at the other stations for both the frequency bands (Figure 20, 21: bottom images) suggesting a major rockslide activity in the surroundings of TOR4.

4.1.2 HVSR inside and outside the sliding wedge

The analysis of HV spectral analysis is often use in landslide area as a tool for deriving the depth of the impendence contrast that generate the HVSR peak and that frequently corresponds to the rupture surface at the landslide base. The depth interval that can be investigated through this technique depends on the amplitude of the frequency band of the employed instrument and on the average V_s of the medium. In literature many cases are reported of peaks at 0.2-0.3 Hz which correspond to horizons at depths of hundreds of meters (e.g., Castellaro et al., 2005). Ambient noise records can also be useful to characterize the dynamic behaviour of the rock mass affected by the presence of fractures linked to the sliding wedge and to investigate the existence of directional effects in the ground motion. Several studies (Panzera et al., 2013; Pischiutta et al., 2013) observed that the microseismic noise in fault and fractured zones are polarized in the horizontal plane with preferred orientation.
In this part, the analysis is aimed at the characterization of the seismo-stratigraphy underlying the acquisition points and at the evaluation of the H/V ratio polarization. The purposes are slightly different for the four stations:

TOR 4: checkpoint on landslide	Identification of the depth of the landslide basal plane throw inversion of the HVSR, recognition of additional layers with different seismic impedance that generate secondary peaks and directional effects due to landslide body.
TOR 1 – TOR 2: stations on the intact area	Check if the rock is actually intact under these points. Determination of HVSR directivity outside the landslide in the lower sector of the quarry.
TOR3: checkpoint on the weakened area above the landslide	Assess the presence of discontinuities or fractures that may lead to future detachments.

For all the 3 component of ground motion the acquired data are detrended, mean-removed and filtered; then, they are divided into windows of 120 s length, each window is tapered with a Tuckey window and padded with zeros. The amplitude spectrum is evaluated via the Fast Fourier Transform (FFT); individual spectra are finally smoothed using a boxcar of wisth 0.1 Hz. The horizontal to vertical spectral ratio is calculated for each window, and the final HVSR function is given by the average of the HVSRs over 6-hr intervals. In this work the horizontal (H) spectra have been computed by averaging E-W and N-S components using

a quadratic average, that show a lower bias with respect to the simple arithmetic mean (Albarello and Lunedei, 2013). HVSR estimates obtained over individual 6-hr interval are represented together with the standard deviation lines (Figure 23, 26, 27, 30). Though some authors suggested that transient signals can affect the estimates of the fundamental frequency of soils, other studies (Parolai and Galiana-Merino, 2006; Mucciarelli, 2007) indicate that a simple variation of amplitude does not affect the resonant frequencies. On these basis, and also considering the great amount of processed data, the spectral ratio was evaluated over the entire trace, without discarding any high-amplitude portion of the recordings.

Directional HVSR analysis was performed to analyse directional effects of the ground motion. Such analysis permits to check if the average HVSR receives more contribution from one of the two horizontal components, and in which direction it operates. The existence of directional effects is investigated at each measurements site by rotating the horizontal components of the spectral ratios by steps of 30° and plotting the contours of spectral amplitudes ratio as a function of frequency and direction of motion (Panzera et al., 2013). Directional HVSR plots represent the projection of HVSR along different directions, from 0° to 180° in a counterclockwise direction (Figure 25, 29, 32; from 0° to 360° results are symmetric). Station TOR1, installed outside the identified landslide body and therefore classified as a rock site, appears to have a rather low amplification effects around 10.5 Hz (Figure 22). The amplification level is low and partly within the accepted uncertainty of the method (i.e. less than 2).

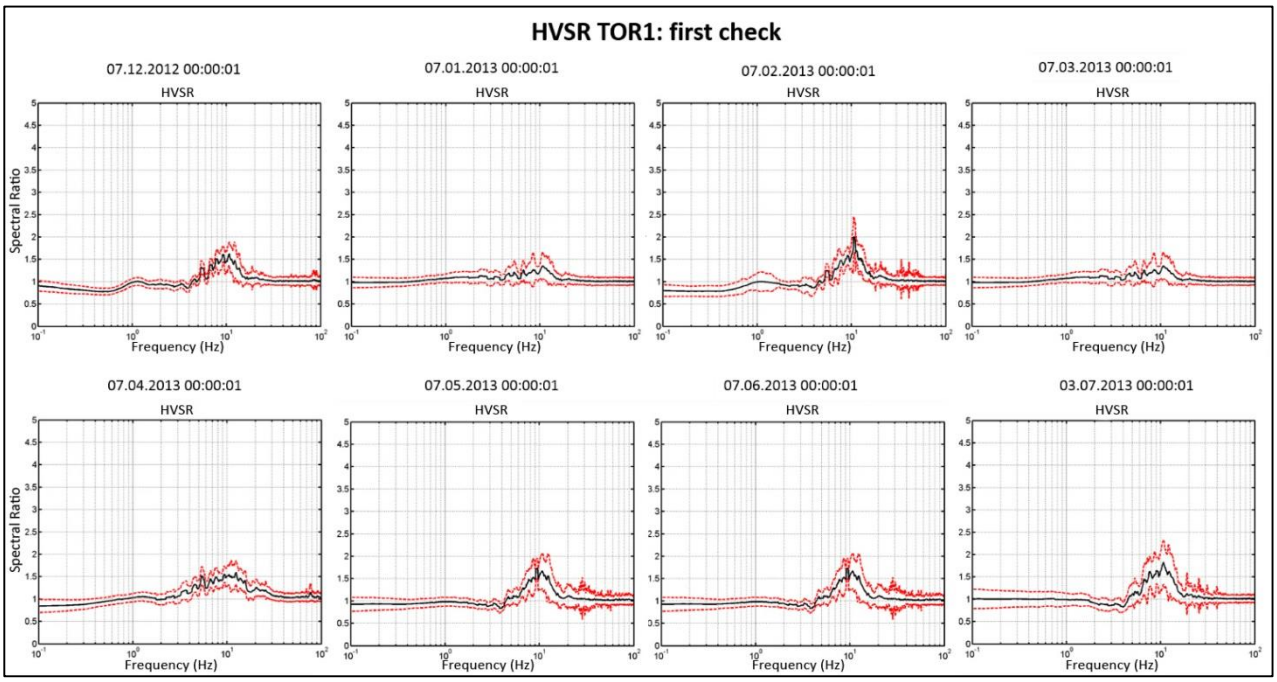

Figure 22 – HV spectral ratios recorded at the station TOR1 on some representative intervals (1 sample interval/month). The black lines are the 6-hr averaged HV and the red dotted lines represent +/- one standard deviation from the mean.

Nonetheless, the peak stability in time (Figure 23) points toward its stratigraphic, non-anthropic genesis that could be linked to a small, near surface impedance contrast.

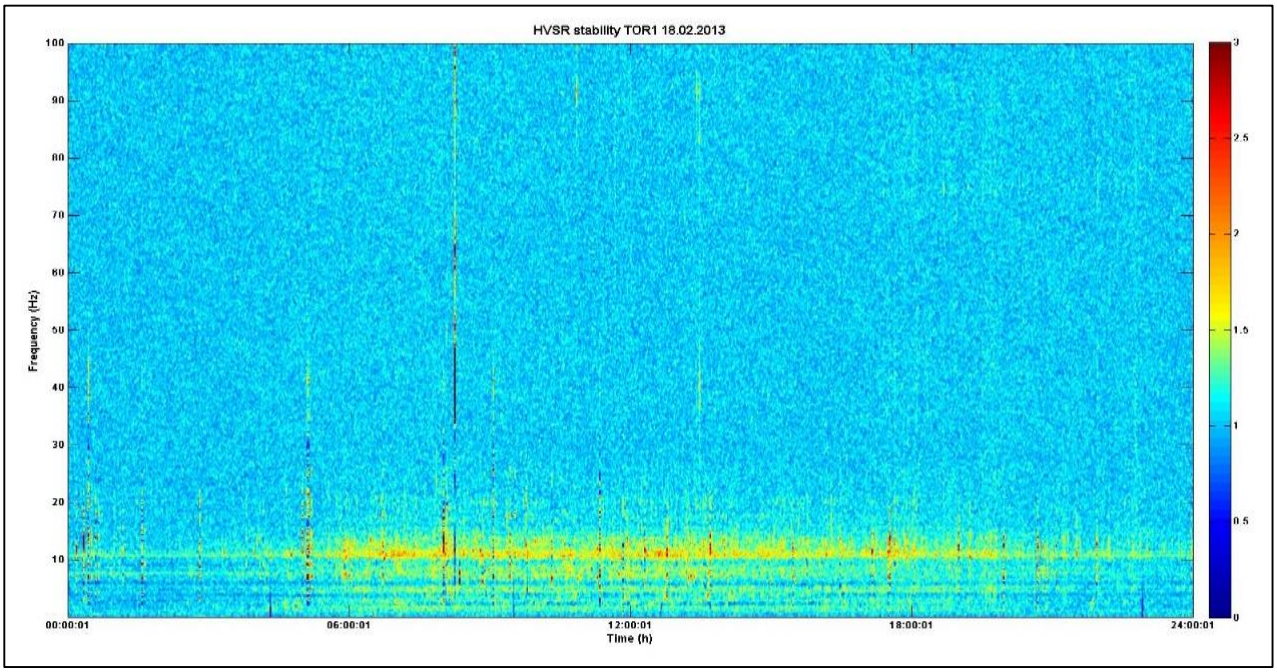

Figure 23 –Time-frequency stability of the HVSR observed at TOR1 during 1 day.

A very low variability in the amplitude value is observed and will be the object of discussion at chapter 4.2.1 when I will evaluate the general trend of the entire dataset.
The rotated spectral ratios obtained at TOR1 show clear directional effects with an angle of about 70° N for the frequency band between 9 and 20 Hz. It is impossible to identify directional effects for secondary peaks at lower frequencies (Figure 24).

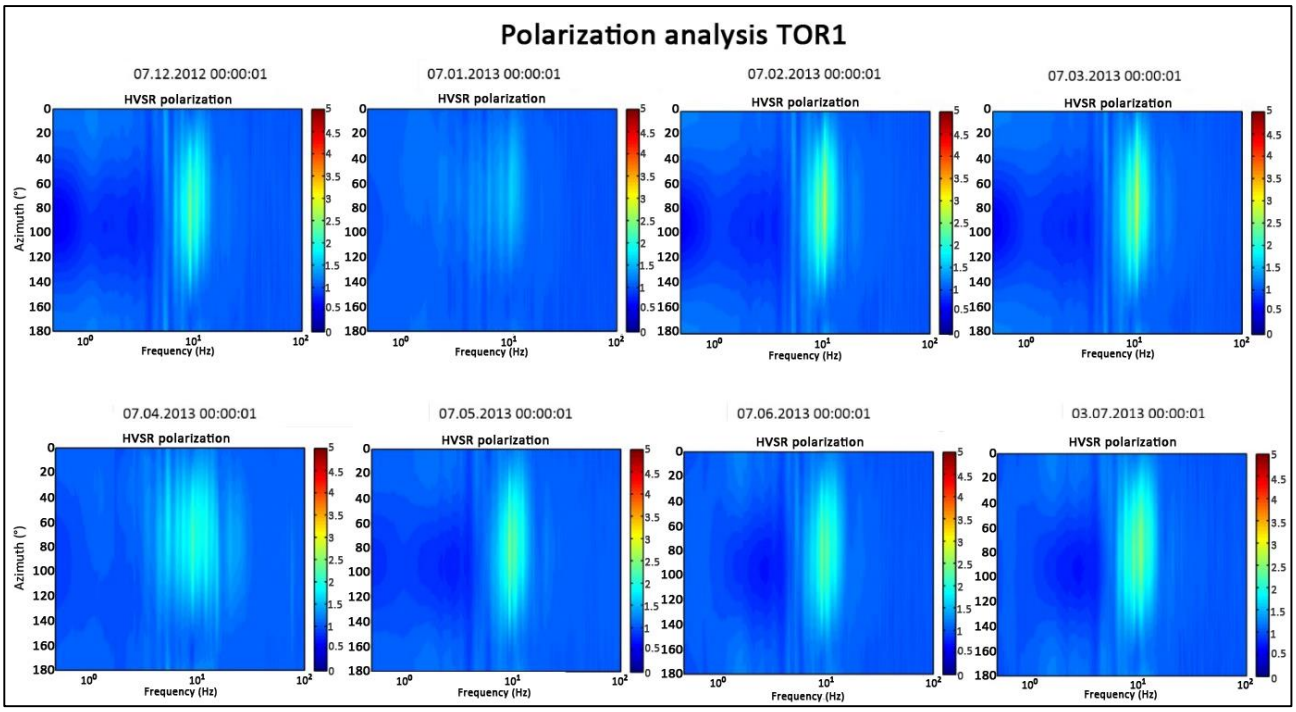

Figure 24 – Examples of the contour maps of the geometric mean of the HVSR as a function of frequency (x-axis) and rotation angle (y-axis) obtained at selected 6-hr recording at TOR1.

TOR2 exhibit the flattest HVSR curves, with a value equal to 1 at all frequencies is observed (Figure 25). The total absence of peaks (amplification factor always less than 2) confirms that this site is suitable as a reference station. We can reasonably assume that this station is placed on intact rock.

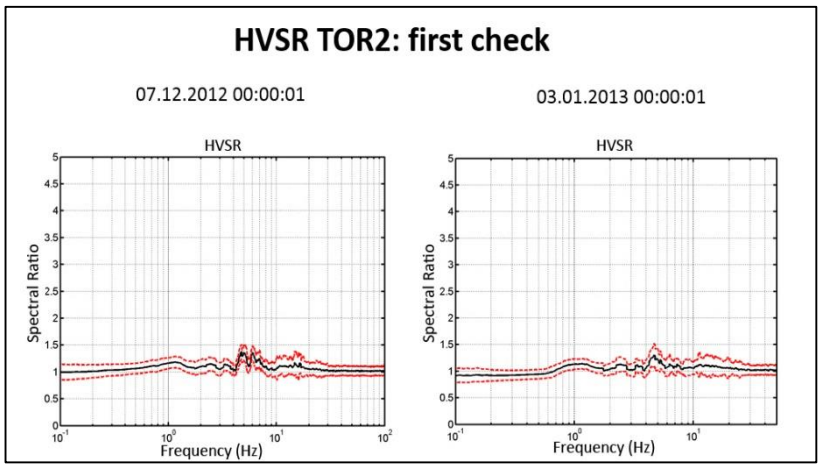

Figure 25 - HV spectral ratios recorded at the station TOR2 on two statistical intervals (December 2012/January 2013). The black lines are the 6-hr averaged HV and the red dotted lines represent +/- one standard deviation from the mean.

The plateau between 1.5 and 6 Hz, which is present at TOR3 (Figure 26), and between 2 and 8 Hz, at TOR4 (Figure 29), stands for a coalescence of minor peaks corresponding to minor

discontinuities at different depths. For these stations we can also assume that the V_s increases very gradually with depth, so that the relative peaks of the HVSR plots originating from that configuration are smoothed. At TOR4 the situation is slightly different from TOR3 because the HVSR shape seems to change from December 2012 to July 2013 both in frequency and amplitude.

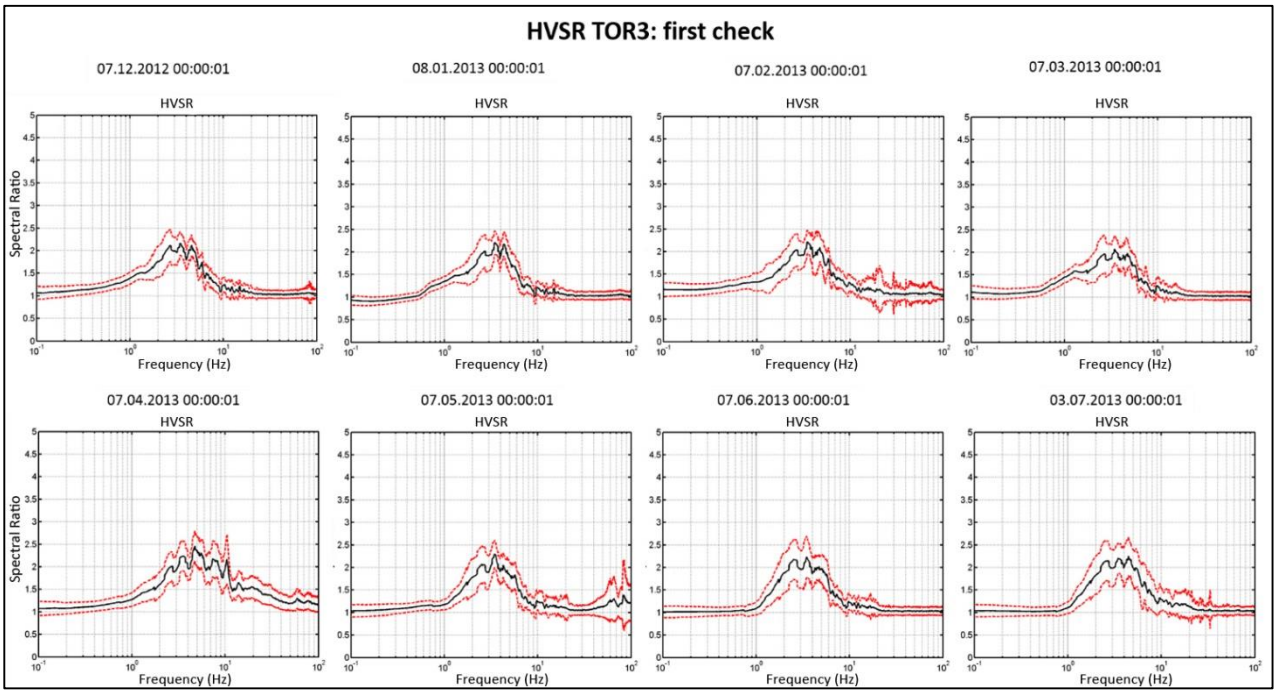

Figure 26 – HV spectral ratios recorded at the station TOR3 on some statistical intervals (1 sample interval/month). The black lines are the 6-hr averaged HV and the red dotted lines represent +/- one standard deviation from the mean.

Again, the strong stability of the frequency peaks that compose the plateau suggests their stratigraphic genesis (Figure 27, 30) while spurious peaks at higher frequencies related to anthropic transient noise can be easily recognized thanks to their impulsive and temporary features.

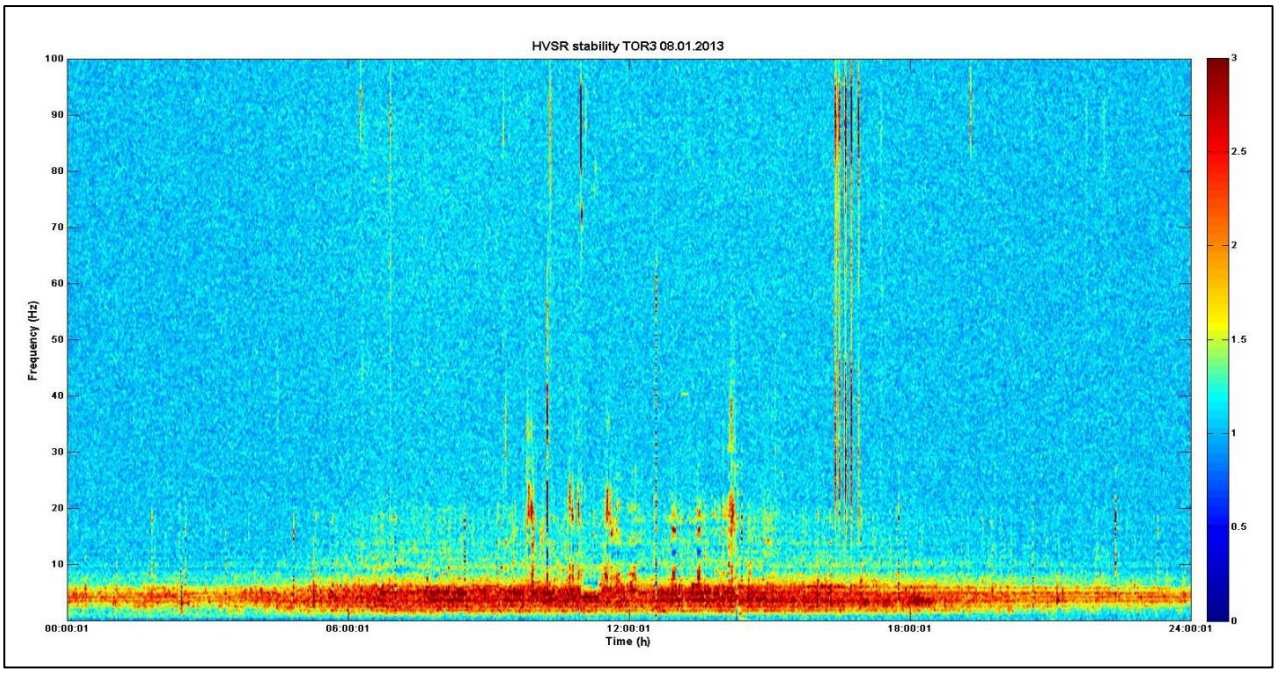

Figure 27 –Time-frequency stationarity of the HVSR observed at TOR3 during 1 day.

Finally, the rotated HVSRs performed at TOR3 and TOR4 appears quite complex: the general trend of the main peak has a prevailing direction respectively of about 50°- 60° (Figure 28) and 70° (Figure 31).

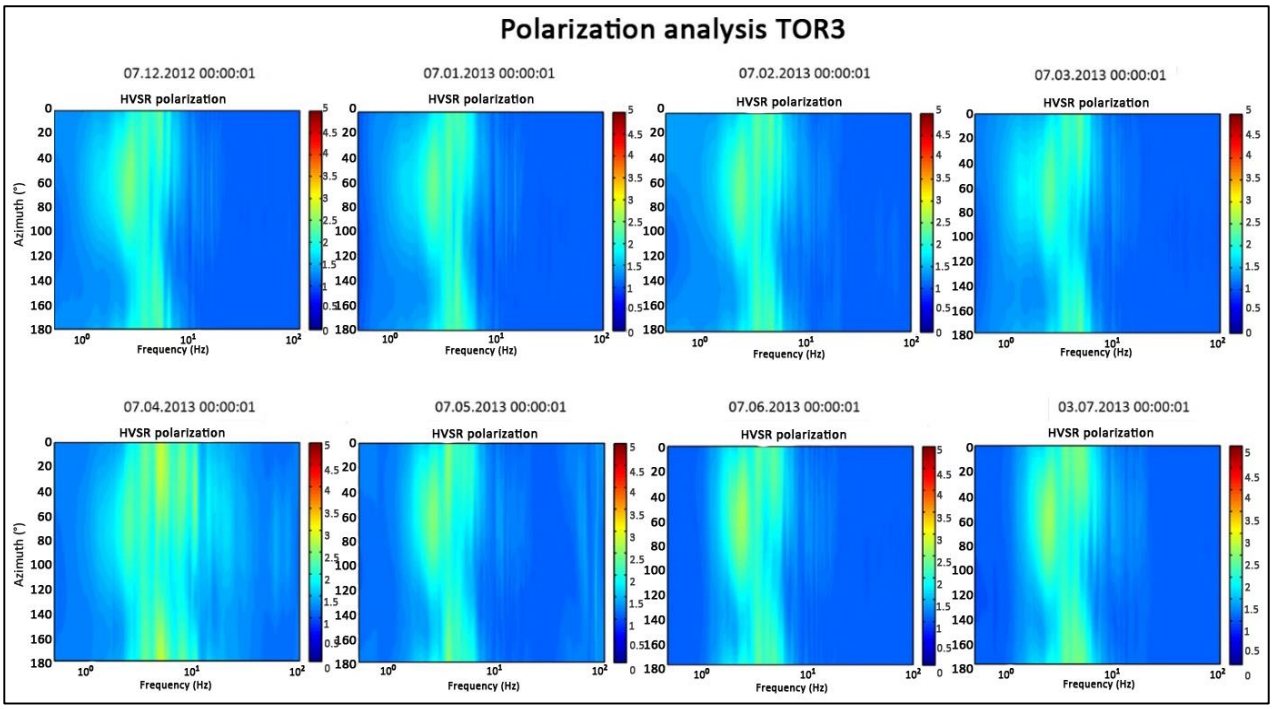

Figure 28 – Examples of the contours maps of the geometric mean of the HVSRs as a function of frequency (x-axis) and rotation angle (y-axis) obtained at selected 6-hr recording at TOR3.

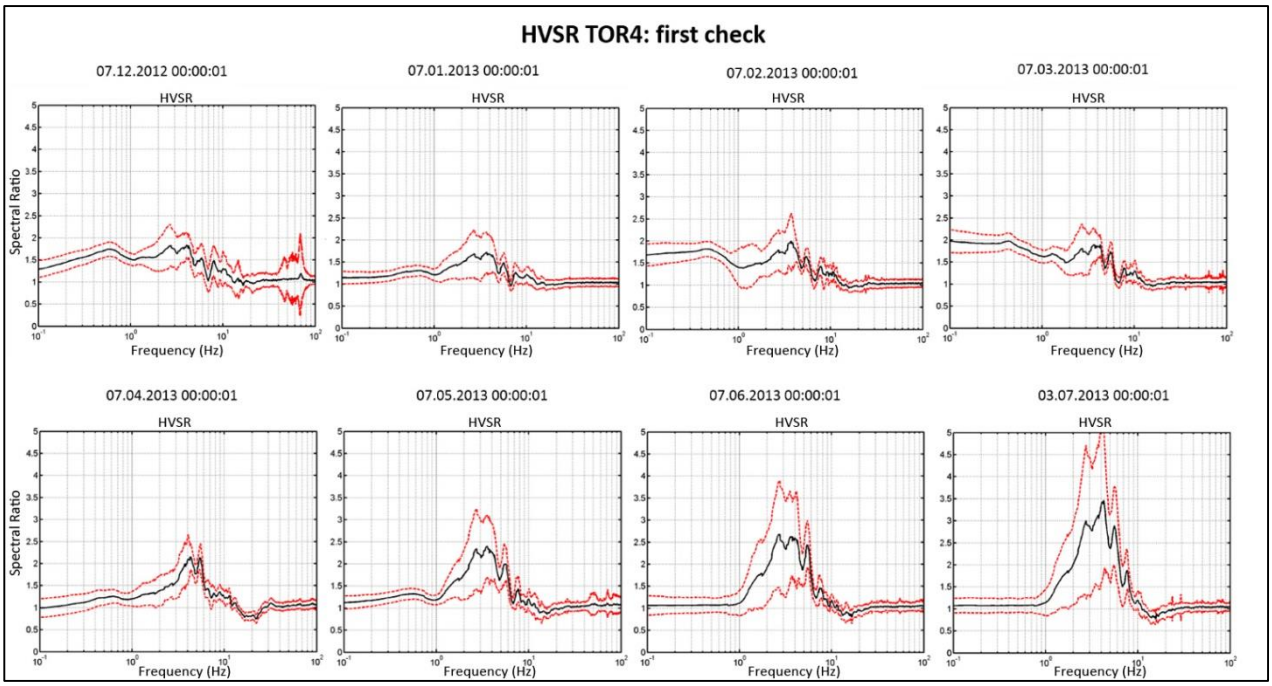

Figure 29 – HV spectral ratios recorded at the station TOR4 on some statistical intervals (1 sample interval/month). The black lines are the 6-hr averaged HV and the red dotted lines represent +/- one standard deviation from the mean.

A shift in the frequency peak corresponds to a variation in the depth of the main discontinuities or to a change of the medium propagation velocity; moreover, large amplitude variation stands for a strong variations of the mechanical properties of the medium (Castellaro et al., 2005). Considering that TOR4 is settled on the rockslide, I can hypothesize that the marked variations observed at that site are related to the mechanical changes in the portion of the sliding wedge below and around the station.

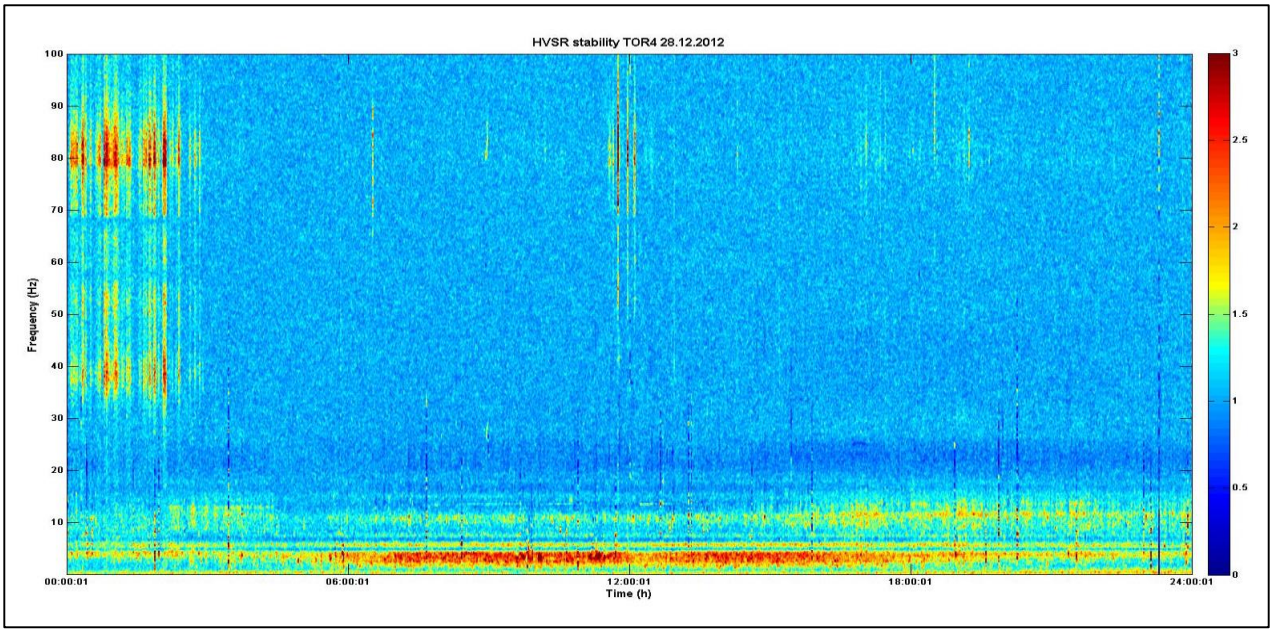

Figure 30 –Time-frequency stability of the HVSR observed at TOR4 during 1 day.

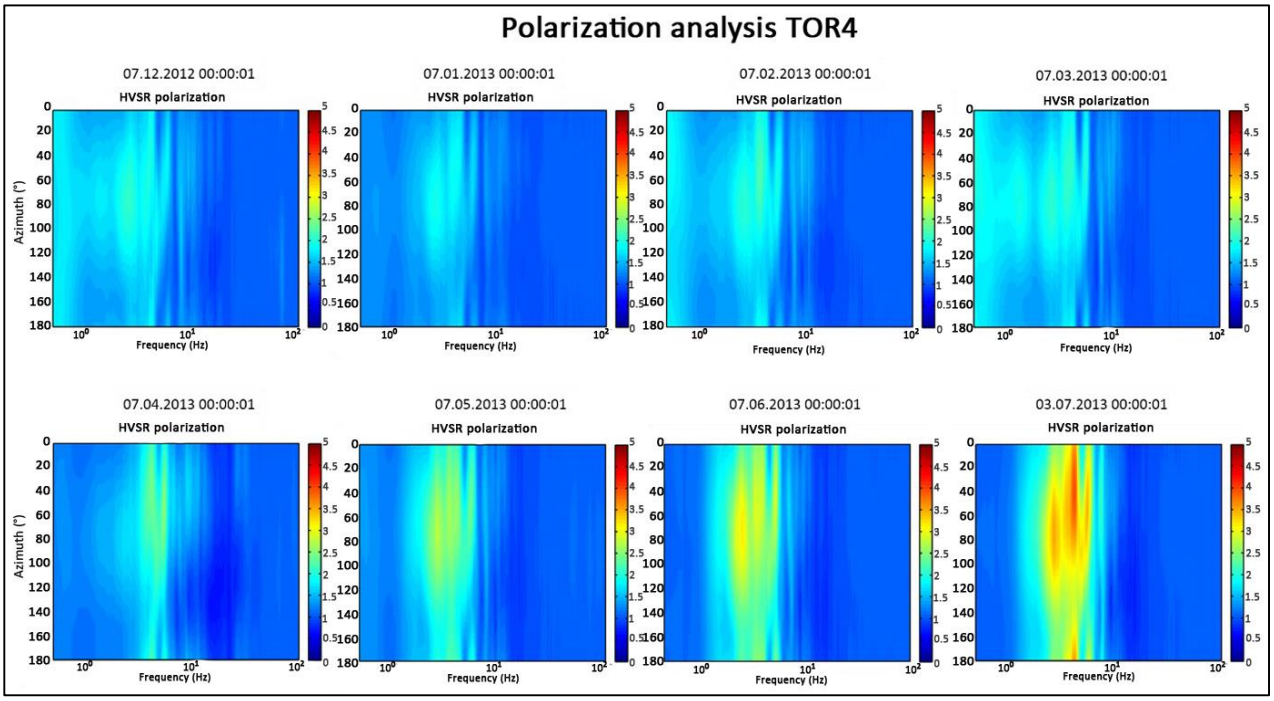

Figure 31 – Examples of the contours maps of the geometric mean of the HVSRs as a function of frequency (x-axis) and rotation angle (y-axis) obtained at selected 6-hr recording at TOR4.

It is generally accepted that the directivity is produced by a combination of factors: topography, source type and medium anisotropy.

The HVSR polarization of the noise data at Torgiovannetto seems to be strongly directional and stable at each station for the entire period: this suggests that the medium anisotropy, due to a well developed fracture field, plays a major role in controlling the polarization of the noise wavefield. Further analysis are required to verify if this behaviour remains constant in case of signals generated by punctual sources regardless of their back-azimuths and different topography. This point will be discuss in section 4.1.4.

A further use of the HVSR observed at each stations, when integrated with the information obtained (directly or indirectly) from previous geophysical survey, is the seismostratigraphic reconstruction beneath the point of acquisition and the estimation of the thicknesses of the fractured superficial that generates the impedance contrast with the underlying compact rock highlighted stations TOR1, TOR3 and TOR4. This topic will be discussed in detail in the next section.

4.1.3 Passive prospection of the sliding wedge using HVSR technique in association with independent geophysical data.

Thanks to the numerous studies carried out in the Torgiovannetto quarry, the landslide

geometry is well-known and the results from a tomographic investigation reported in Casagli et al. (2007b) provides detailed information about the V_P (α) pattern of the investigated area. The available geophysical analysis consists of six arrays carried out with a 24 channels PASI seismograph (mod.16S24) and 36 geophones with a natural frequency of 100 Hz that results in six tomographic sections (L1-L6, Figure 32). Lines L1 and L5-L6 intersect respectively TOR4 and TOR3 (red circle).

These acquisitions provide a comprehensive view of the upper part of the study area but give us limited information about the geophysical structure at TOR1 and TOR2.

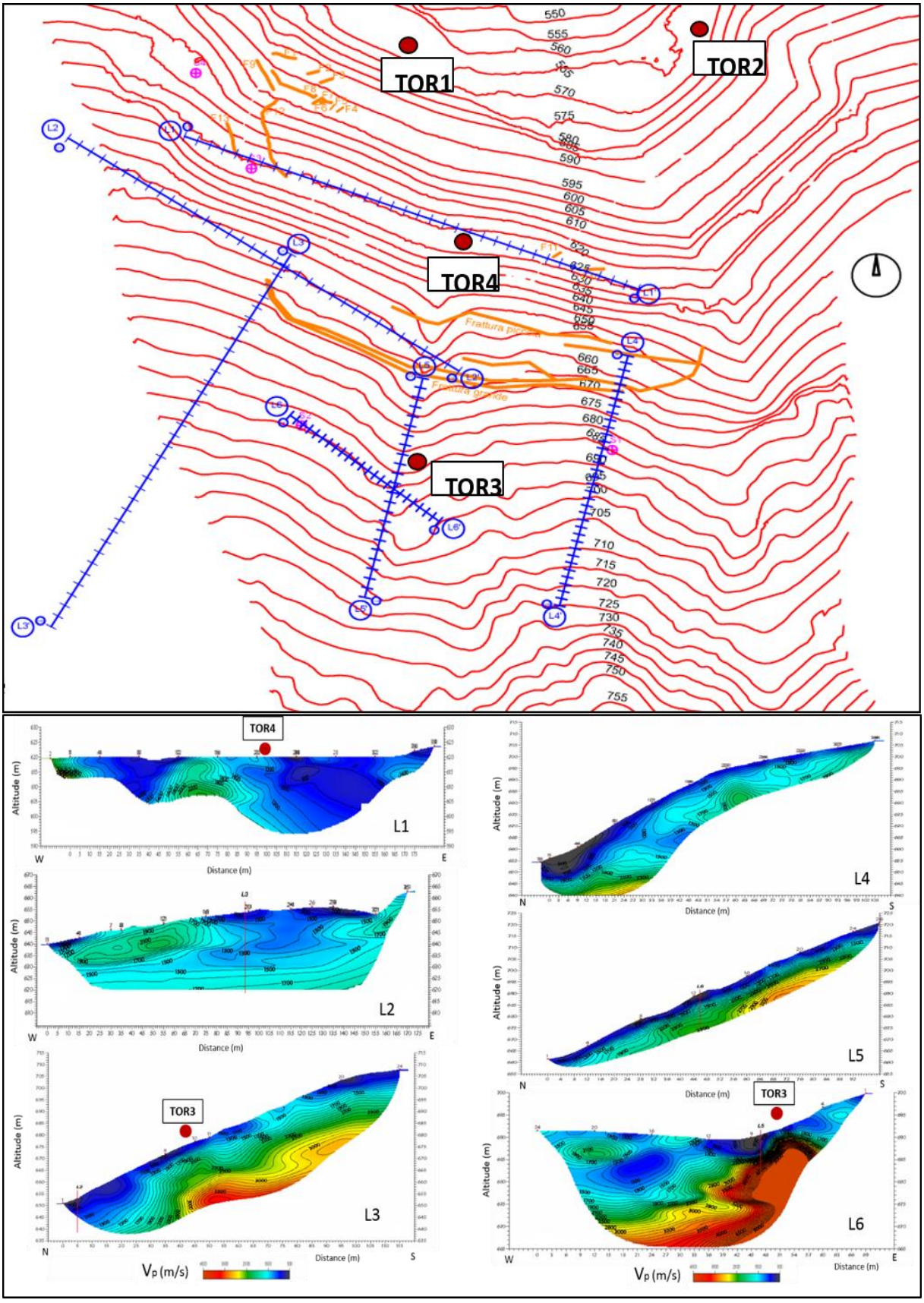

Figure 32 – Location of the six array carried out at Torgiovannetto site (top) and relatives seismic sections (bottom). In figure are also shown the main fractures.

For the purpose of this work, I conducted a supplementary noise survey at 5 sites spaced by 9 m, in order to obtain a 2D "impedance contrast" map of the area near TOR4. Because of the slope morphology, the profile has been located along a direction parallel to the main fractures, completely superimposed on L1 central section profile (Figure 33 left, yellow rectangle).

Noise recordings were obtained using 5 portable digital seismographs series TROMINO® (Micromed S.p.A), equipped with three electrodynamic orthogonal sensors (velocimeters) working at frequencies down to 0.3 Hz. Seismic noise has been acquired with a sampling frequency of 128 Hz and recorded for 22 minutes following the standard procedure suggested by Bard and SESAME-Team (2005). This allowed obtaining "stable" HVSR curves. Data acquired during the recording session were subdivided into time windows of 25 s, applying a linear detrending to each window to remove long-term drift. Horizontal to vertical spectral ratios were then calculated and inverted in Matlab interpolating the results obtained at every single point using equation (1.1).

Comparing Figures 34, bottom right and bottom left, the 2D impedance contrast retrieved with passive seismic prospection and the 2D V_p map provided by Casagli et al. (2007) are visually comparable. This similarity suggests that HVSR analysis can be exploited to estimate the 2D velocity heterogeneities in the subsurface saving both time and costs of the analysis.

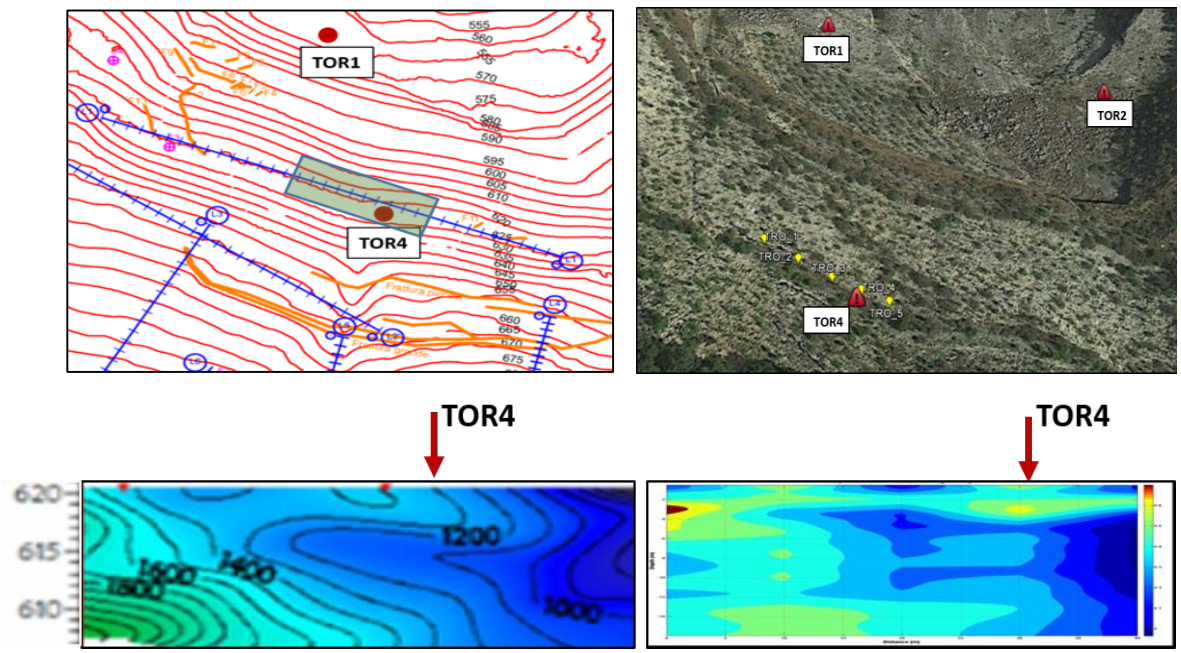

Figure 33 – Upper panels show the arrays locations while lower panels show the two resulting sections: L1 2D V_P map retrieved from active seismic tomography and 2D "impedance contrast" map derived from inversion and interpolation of HVSR measures at 5 acquisition points spaced by 9 m..

If I can assume that the subsurface asset has remained substantially stable from 2007 to 2013, then it is possible to derive a quantitative V_S (β) from the active tomography V_p values, assuming a Poisson's ratio of 0.25:

$$\boldsymbol{\beta = \alpha/\sqrt{3}} \qquad \mathbf{(1.4)}$$

Based on equation (1.1), the resonance frequency value is inversely proportional to the interface depth between two layers characterized by a contrast of seismic impedance. The higher the contrast, the higher the expected amplitude of the H/V peak, although this correlation is not linear (Mucciarelli and Gallipoli, 2001). Therefore, since a reliable V_s of the upper layer is available for each station (see Table IV below), the HVSR frequency peak can be approximatively translated into a corresponding depth of the impedance contrast.

Station	V_p (estimated from tomography)	V_s (calculated using Eq. 1.4)
TOR1	1.800 m/s	1.039 m/s
TOR2	-	-
TOR3	700 m/s	404 m/s
TOR4	1.200 m/s	692 m/s

Table IV – Parameters related to the medium propagation velocity: V_P retrieved by active seismic tomography (2007) and V_S calculated using Eq. 1.4.

I also conducted two additional ambient noise arrays recordings (29 measures, Figure 34), in order to get constrains on the lower part of the test-site. Unfortunately, however, instrumental failure during data retrieval caused permanent loss of most of the recordings.

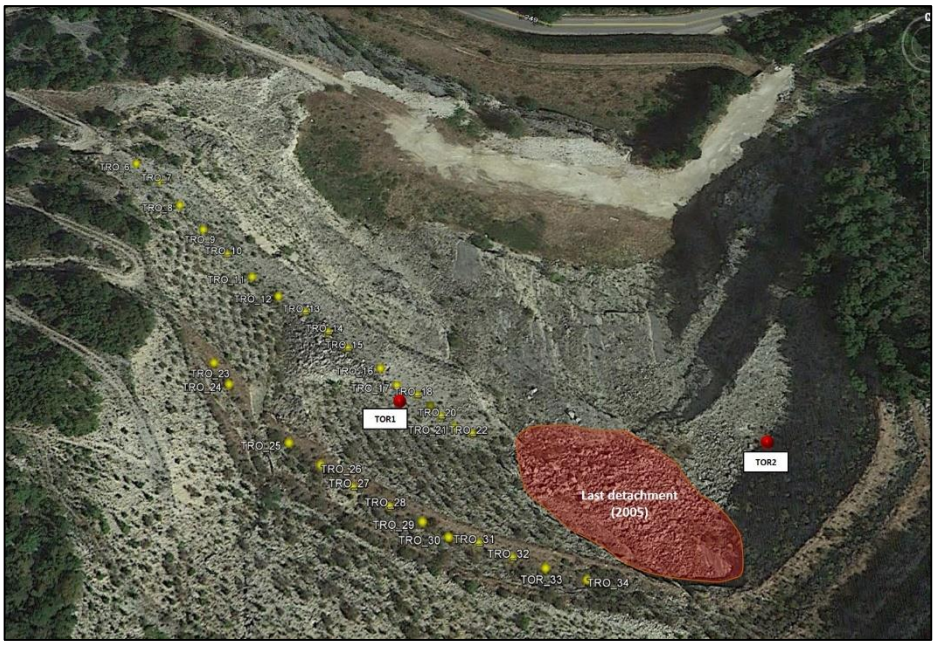

Figure 34 – Location of the measurements of passive seismic acquisition carried out both for the seismo-stratigraphic characterization of the lower part of the quarry and for the validation of the data acquired by the reference station TOR1.

Results from only a few measurement points are presented here confirming the existence of the 10 Hz frequency peak previously observed at TOR1. Four acquisition points (TRO6, TRO11, TRO12 and TRO13) show a significant peak (amplitude > 2) around that frequency (Figure 35).

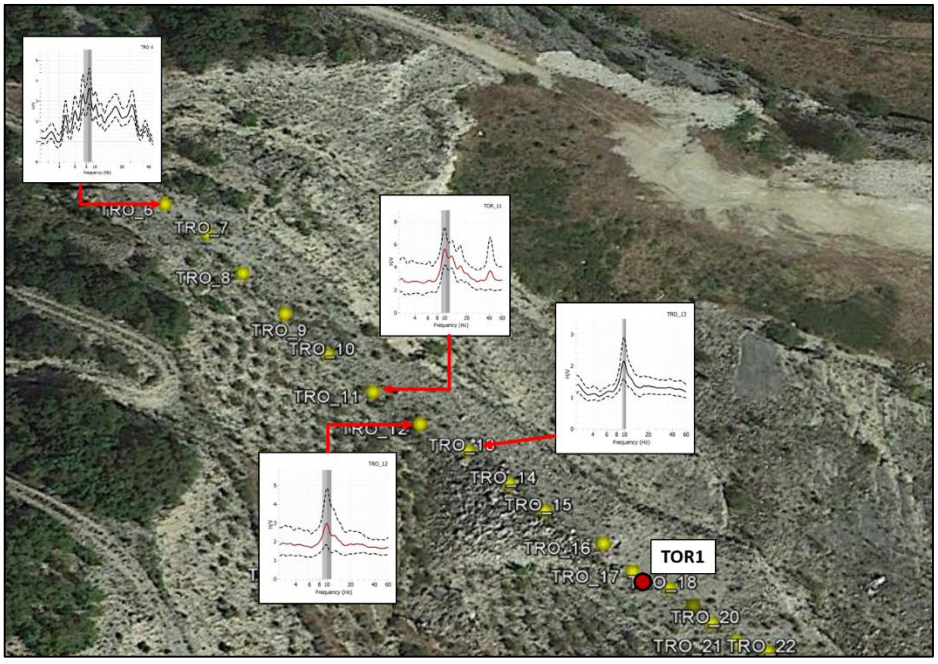

Figure 35 – HVSR peaks recorded at four of the 29 measures carried on in the lower section of the quarry: thick line represent average HVSR, dotted lines represent the standard deviation.

The constancy of the frequency peak along the array reveals that TOR1 is not settled on intact rock as we assumed but, on the contrary, is probably located above a fractured surficial layer superimposed on the compact rock.

For this same site, the depth identification related to the main frequency peak recorded at TOR1 is easy to define because here a single peak is identified (Figure 36). The interface corresponding to the TOR1 peak (10.5 Hz) is at about 26 meters depth so that we can assume that as boundary between highly fractured and semi-intact rock.

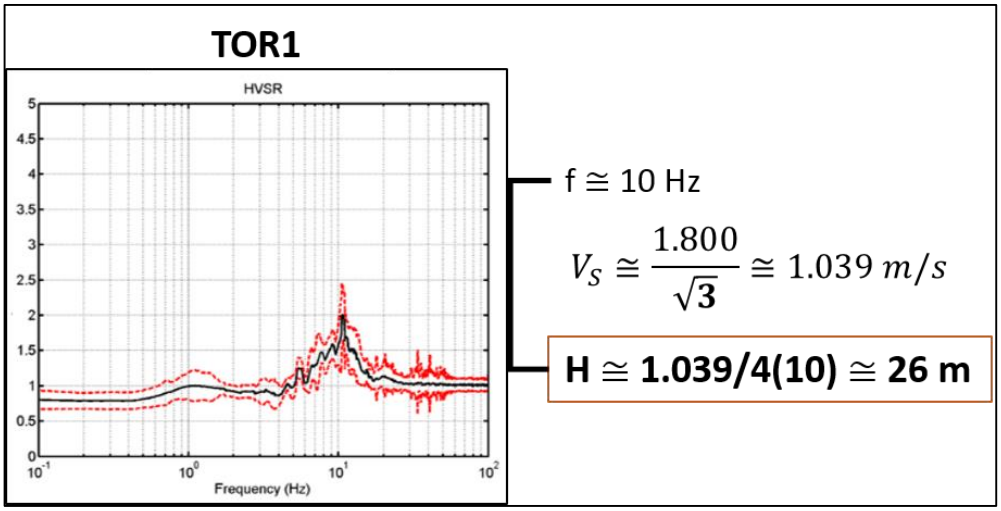

Figure 36 – Example of HVSR peak recorded at TOR1. **f** stands for the frequency peak, $\mathbf{V_S}$ is evaluated starting from V_P value and **H** is the depth corresponding to the peak in f using Eq. 1.1.

The presence of 10 Hz peak at several measurement points around station TOR1 suggests that the unstable area is larger than expected and it includes the western lower part of the quarry.

The inversion has not been carried out at TOR2 because no significant peaks were detected; at TOR3 and TOR4, the picture is somewhat more complex.

It is worth noting that the real stratigraphic successions are generally more complex than two simple layers characterized by a contrast of seismic impedance, since in most cases (and the situation at TOR3 and TOR4 are two) we deal with sequences composed of different layers with more than one contrast of impedance. However, when a multilayer succession is investigated by HVSR technique, the final shape of the spectral ratio shows as many peaks (in these cases coalescing into a plateau) as the horizons of seismic impedance, thus giving information about the seismo-stratigraphic state of the geological layers (Oliveto et al., 2004).

To obtain a reliable value of the main impedance contrast depth in those cases we decided to invert the first and the last peak of the plateau observed at these stations to have a general idea about both the maximum and minimum depth (H_{max}, H_{min}) within the sliding surface could be located.

TOR3, for which I estimated a V_s equal to 404 m/s, has a first peak at 2,5 Hz that correspond to a depth of 40 m, and a last peak at 4,5 Hz standing for an interface located at 22 m (see Figure 37).

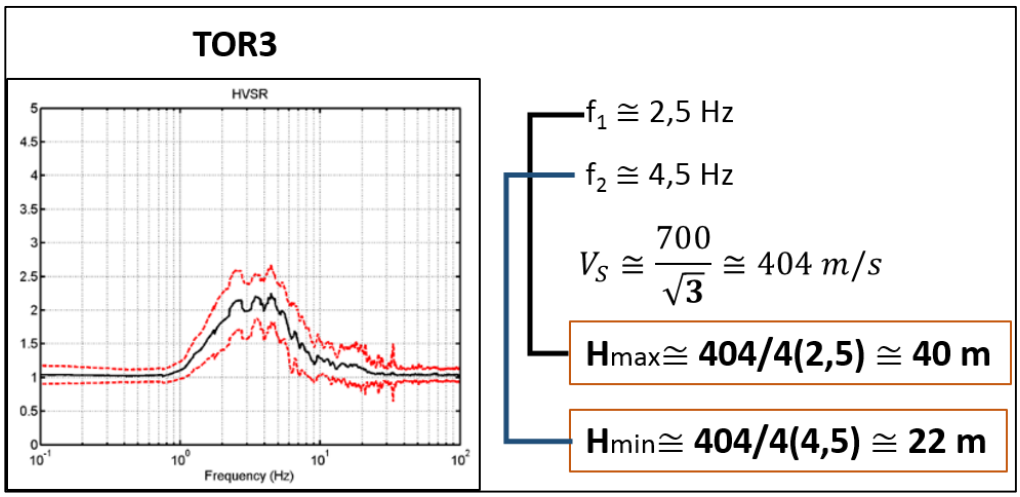

Figure 37 – Example of HVSR peak recorded at TOR3. **f** stands for the frequency peak, **Vs** is evaluated starting from V_P value and and $\mathbf{H_{min}}$ and $\mathbf{H_{max}}$ are the depths corresponding respectively to the first and last peaks in f calculated using Eq. 1.1.

Spectral ratio at TOR4 is really similar in shape to TOR3 but the first and last frequency peaks are at 2,8 Hz and 8 Hz that correspond respectively to a depth of 61 m and 22 m (Figure 38).

Moreover, we also have to take into account an evolution of the subsurface at TOR4 acquisition point because of the change in shape of the plateau observed through the monitoring period.

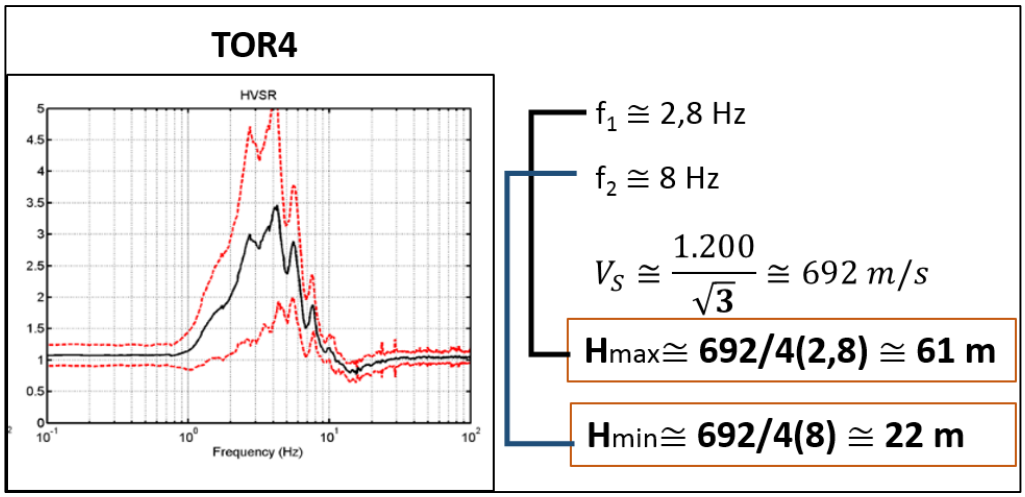

Figure 38 – – Example of HVSR peak recorded at TOR4. **f** stands for the frequency peak, **Vs** is evaluated starting from V_P value and $\mathbf{H_{min}}$ and $\mathbf{H_{max}}$ are the depth corresponding respectively to the first and last peaks in f calculated using Eq. 1.1.

The above results thus suggest a grid of measurements evenly distributed over the entire area would enable the reconstruction of the sliding wedge, even in an unfavourable geological context such as the one here accounted for. Though beyond the scope of this work, observation indicates a promising direction for future studies.

4.1.4 Seismic response of the slope: comparison of HVSR and directivity analysis from seismic noise and major EQ

The aim of this section is to analyze the reliability of the amplification functions previously presented (Volant et al., 1998; Bour et al., 1998) by comparing results obtained from the 7 months of continuous noise recording ($HVSR_N$) with those retrieved on the seismograms of 25 local earthquakes ($HVSR_{EQ}$) occurred within the same period (Trifunac and Todorovska, 2000).

Earthquakes were extracted from the Italian Seismological Instrumental and Parametric Data-base (ISIDe) catalog that provides the earthquake parameters obtained by integrating data from locations performed in near-real time with data from the Italian Seismic Bulletin. Imposing no filter on the magnitude, a total of 5241 events occurred in the period of interest, considering a 100 km-side square centered on the acquisition site. Splitting the main seismogenic sources into quadrants according to relative direction with respect to the test-site (Figure 39), it is clear that they are evenly distributed in three of the four sectors (I°, II°, III°), while just a few of them are located in quadrant IV°. The main characteristics of each event are listed in Table V.

The analyzed events are selected according to two main criteria:

(1) Adequate amplitude and duration at the acquisition site to obtain a representative HVSR evaluated on the event S- and coda waves (function of distance and magnitude)

(2) Representativeness of a large variety of seismogenic sources and time of occurrence.

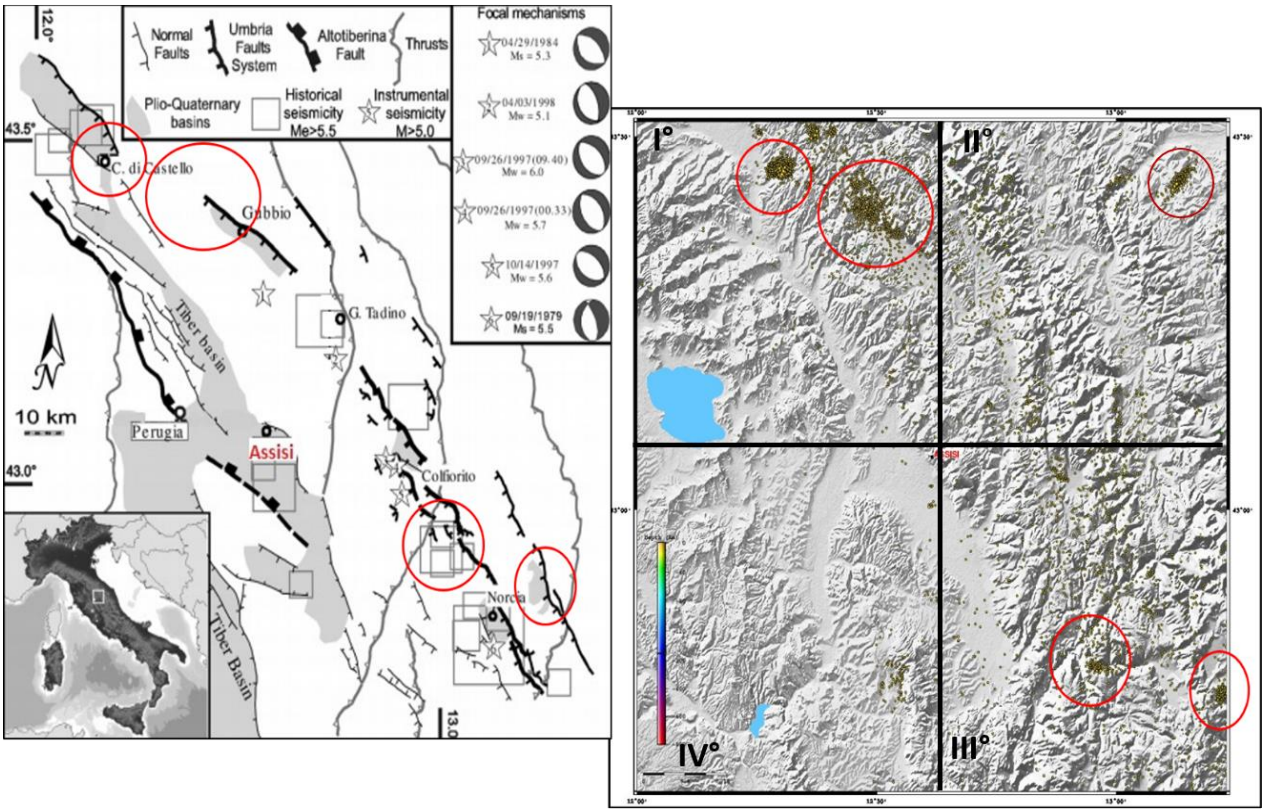

Figure 39 – Schematic structural map of the Umbria-Marche region showing the main seismogenetic structures belonging to the Umbria Fault System (on the left) and location of the events (D< 50 km; 0<M<10) occurred during the monitoring period (on the right, from ISIDE). See the text for details.

HVSR and its directivity are retrieved separately from the corresponding 6-hr file noise recordings ($HVSR_N$) and from the S and coda waves of the selected event ($HVSR_{EQ}$) using windows respectively of 120 and 5 second length. Results are summarized in Table V which also reports frequency, amplification and directivity directions of each pair of $HVSR_N$ and $HVSR_{EQ}$ measurements (Figure 40, 41, 42).

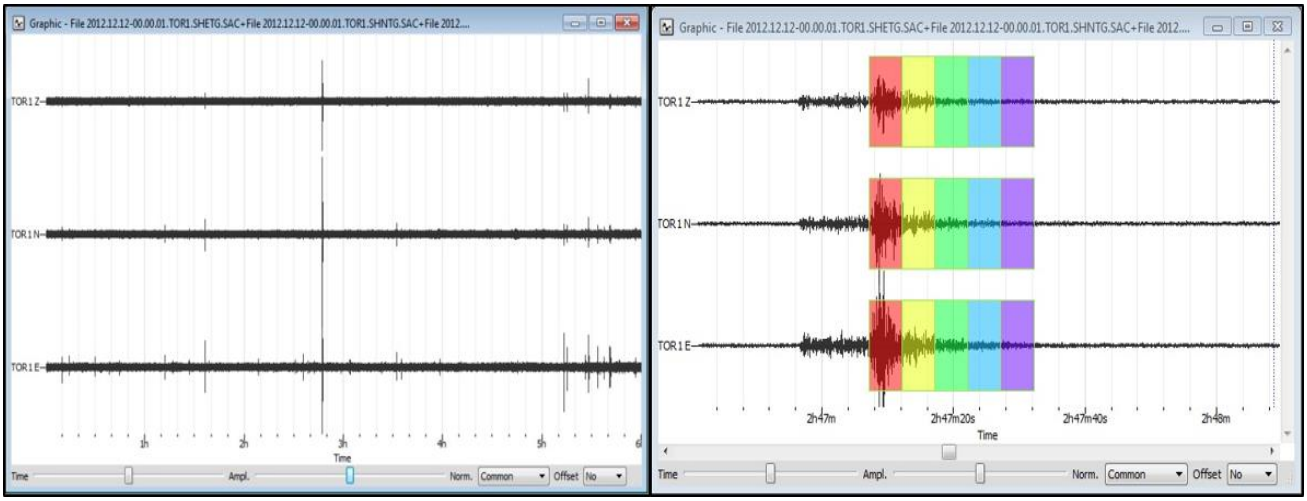

Figure 40 – Example of data acquired at TOR1: 6-hr file (left) and single earthquake event (right). Colored windows are the ones used for computing H/V and matching with colours of individual H/V curves presented in Figure 42.

Figure 41 shows $HVSR_N$ and $HVSR_{EQ}$. The black curves of both the left and right images represents geometrically averaged over all colored individual HVSR curves while the dashed lines are the HVSR standard deviation. The grey areas represent the averaged peak frequency and its standard deviation: the peak is at the limit between the dark grey and light grey area.

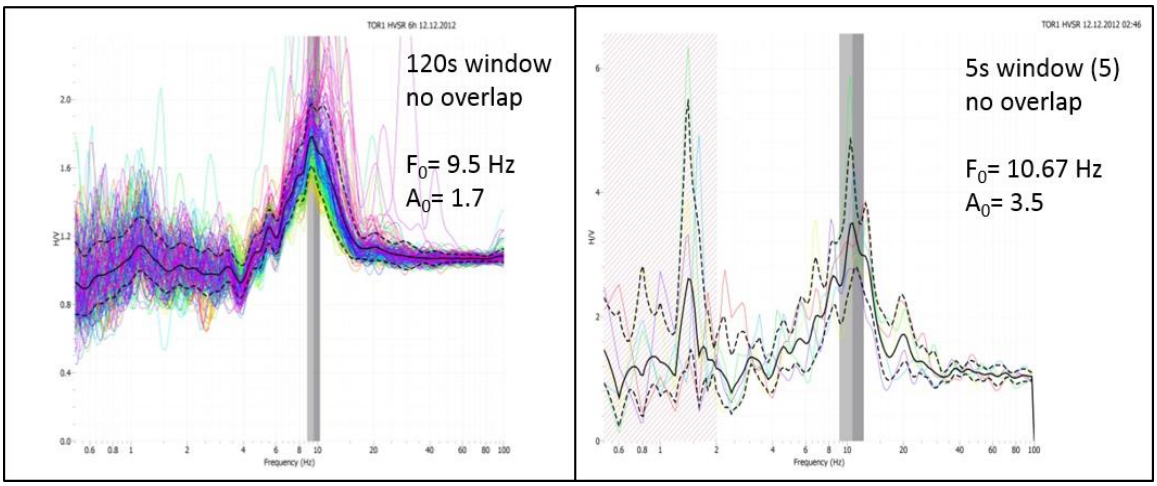

Figure 41 – Example of HVSR calculated both on 6-hr of noise recording (left) and on an earthquake S and coda waves (right) recorded at TOR1. Colored lines represent the HVSR obtained for each window.

After comparing and verifying the interchangeability of the Matlab script used in Section 3.1.2 and the Geopsy H/V rotate tool to calculate the directionality, I decided to proceed using the second technique which is faster to process small portions of acquired signals. A series of HVSR is calculated from 0° to 180° every 10° and is presented in a frequency-azimuth map (Figure 42).

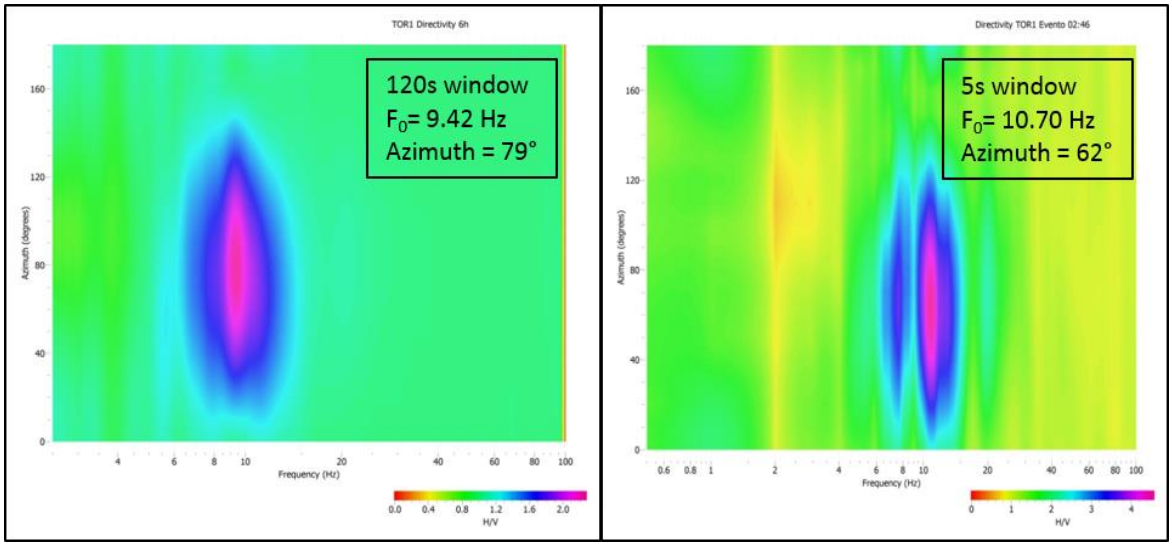

Figure 42 – Example of contours maps of the geometric mean of the HVSRs as a function of frequency (x-axis) and rotation angle (y-axis) obtained at selected 6-hr recording (left) and on an earthquake S and coda waves (right) at TOR1.

The same procedure is applied to stations TOR1, TOR3 and TOR4 for each selected event in order to evaluate the different seismic response respectively in the lower and upper part of the quarry area.

At TOR1, the $HVSR_N$ function is similar to the $HVSR_{EQ}$, but only regarding the frequency of the main peak, while the amplitude of the main $HVSR_N$ peak is systematically lower than that of the $HVSR_{EQ}$ function (Table V; orange row, column 6 and 7).
For most cases, both TOR3 and TOR4 (Table V: green and blue rows), show the onset of a secondary peak at lower frequencies, regardless the source magnitude and its direction. Also in these cases the $HVSR_N$ peak amplification value is lower than that observed for $HVSR_{EQ}$. TOR2, as expected, shows no significant peak even for spectral ratios related to earthquakes ($HVSR_{EQ}$ peak < 2) so that the directivity analysis is not representative for this station.

Event	Lat Lon (Source back-azimuth)	M	F Peak (Hz)		Amp peak		AZM Peak (°N)		Depth (km)	D (km)
			N	Eq	N	Eq	N	Eq		
01/06/2013 10:58:36	43.004 12.609 SW (206°)	2.6	10	11.4	2.1	2.6	70°	68°	8.3	8
			2.6	1.5	2.5	3.2	56°	60°		
			ND	ND	ND	ND	ND	ND		
17/02/2013 16:38:20	43.141 12.738 NE(39°)	2.1	10	11.4	2.1	2.9	69°	63°	9.2	10
			4.5	1.1	2.3	2.5	30°	60°		
			3.5	1.3	2.1	4.4	54°	66°		
26/05/2013 22:43:07	43.227 12.569 NW(333°)	2.6	9.5	10.5	1.8	2.1	74°	73°	11.1	18
			4.3	3.7	2.0	2.7	28°	60°		
			4.1	4.2	2.1	3.2	50°	90°		
25/05/2013 23:26:02	43.087 12.812 E(80°)	3.6	10.5	10	2.0	2.6	73°	69°	62.7	13
			4.6	3.7	2.5	2.9	27°	66°		
			4.4	1.3	2.4	6.7	55°	74°		
07/02/2013 01:19:15	43.121 12.825 N(16°)	2.1	10.5	11.9	2.0	3.4	70°	70°	9.6	15
			3.5	1.5	2.3	3.4	30°	60°		
			3.5	1.8	2.0	4.4	52°	70°		
02/02/2013 10:53:33	43.248 12.722 N(15°)	2.0	10.8	11.5	2.1	2.9	69°	68°	12.4	20
			2.7	1.2	2.5	4.4	57°	52°		
			2.9	3.4	2.7	4.1	66°	60°		

12/01/2013 16:18:24	42.932 12.807 SE(139°)	2.1	11.2	12	1.8	3	69°	73	6.9	20
			2.7	1.8	2.6	3.3	54°	49°		
			2.9	1.4	2.2	4	70°	111°		
03/07/2013 22:32:04	43.211 12.862 NE (50°)	2.1	9.3	12.4	1.7	3.1	69°	69°	10.3	23
			4	4.1	2	2.9	15°	165°		
			4.1	1.8	3.0	9.2	52°	90°		
07/06/2013 17:39:15	42.917 12.955 SE (124°)	2.0	10.4	11.4	2.2	2.6	69°	73°	9.7	30
			2.6	4.0	2.5	3.0	54°	(27°)		
			3.4	3.4	3.8	6.6	64°	57°		
30/05/2013 22:29:32	42.802 12.702 SE (170°)	2.2	10	11.2	1.9	3	67°	71°	6.9	30
			4.5	2	2.2	3.5	18°	72°		
			4.1	1.7	2.4	8.3	56°	90°		
05/05/2013 22:01:35	43.043 12.894 E (110°)	2.0	9.7	11.4	1.6	3.3	73°	66°	7.9	21
			3.5	1.3	1.9	3.5	21°	43°		
			4.3	3.3	1.9	6.2	47°	49°		
20/04/2013 04:36:31	43.006 12.87 E (113°)	2.0	9.8	10	1.6	3.0	72°	70°	7.9	21
			3.6	4.5	2.1	2.9	18°	137°		
			3.8	1.7	2.1	6.4	51°	78°		
31/03/2013 07:42:45	43.018 12.883 E (108°)	2.1	11.1	11	1.8	3.5	66°	70°	6.7	21
			2.7	1.8	2.2	3.2	57°	60°		
			3.5	1.6	2.1	5.0	56°	63°		

12/02/2013 14:37:16	43.028 12.885 E (105°)	2.0	10.8	11.4	2.4	3.2	71°	70°	6.7	21
			2.6	1.4	2.6	3.7	59°	68°		
			2.7	1.5	2.8	5.1	70°	76°		
21/12/2012 18:30:55	42.924 12.972 SE(130°)	2.0	10.4	11.8	1.5	2.5	67°	69°	10.4	25
			3.8	1.7	2.2	3.2	18°	49°		
			3.7	1.6	1.9	3.5	54°	66°		
			5.0	0.7	1.3	1.9	87°	74°		
31/01/2013 15:53:57	42.888 12.85 SE(140°)	2.4	11.0	11.8	2.0	3.2	68°	63°	9.5	26
			2.6	4.2	2.7	3.2	61°	14°		
			2.7	3.8	3.1	4.8	72°	63°		
18/12/2012 13:57:54	43.039 12.886 E(100°)	2.9	10.6	11.0	2.7	2.0	63°	67°	7.8	21
			3.7	3.4	2.6	2.9	15°	15°		
			2.9	1.3	2.9	4.7	64°	101°		
			4.6	1.0	1.6	1.9	85°	160°		
12/12/2012 02:46:42	42.545 13.298 SE (137°)	2.0	9.5	10.7	1.7	3.5	79°	68°	12.6	78
			4.1	4.4	2.1	2.7	20°	15°		
			3.5	1.5	1.8	4.1	70°	60°		
			5.2	3.5	1.4	1.7	86°	60°		
21/02/2013 13:56:14	43.052 12.871 E (99°)	1.1	11.1	11.9	2.1	3.4	65°	60°	8.5	19
			2.6	1.5	2.7	3.9	61°	60°		
			2.7	2.9	3.3	5.3	70°	50°		

01/05/2013 08:01:33	43.101 12.508 NW (284°)	1.8	11.1	3.3	2.1	3.6	67°	30°	8.0	10
			2.8	1.7	2.1	3.4	60°	63°		
			3.7	1.9	2.8	7.3	60°	40°		
18/12/2012 17:03:54	43.131 12.731 NE (48°)	1.2	11	10.2	2	3.8	65°	67°	9.1	9
			3.6	1.3	2.7	3.2	25°	42°		
			3.0	1.3	3.0	4.3	74°	40°		
			4.6	4.5	1.5	1.9	90°	90°		
08/05/2013 00:52:16	43.45 12.302 NW(325°)	3.6	10.3	11.6	2.1	3.4	77°	66°	7.7	51
			3.6	1.1	2.5	4.5	19°	32°		
			3.9	1.2	3.1	8.5	66°	29°		
18/05/2013 13:15:56	43.458 12.289 NW(325°)	2.2	10.4	11.6	2.1	2.6	69°	66°	8.5	53
			2.7	1.7	2.4	3.0	56°	40°		
			3.8	1.3	3.1	9.1	54°	60°		
21/04/2013 06:17:33	43.453 12.308 NW(325°)	3.2	10.9	11.1	2.3	2.7	71°	68°	7.8	50
			3.8	1.2	2.6	3.3	26°	65°		
			3.8	1.2	3.3	9.3	56°	45°		
24/04/2013 19:57:32	43.4 12.493 NW(340°)	1.1	10.2	9.8	1.7	2.3	69°	70°	8.7	38
			3.8	3.6	2.1	3.0	17°	20°		
			4.1	3.5	2.2	4.2	52°	60°		

Table V – Main features of selected earthquake: In the white column: EVENT, LAT/LON, M, DEPTH and D indicate earthquake date, back-azimuth, magnitude, depth and distance. In the coloured column: F peak, Amp peak and AZM peak represent the resulting frequency peak, the peak amplitude and the peak azimuth both for noise and earthquake. Each parameters is calculated for station TOR1, TOR2, TOR3 and TOR4 (respectively orange, red, green and blue raw).

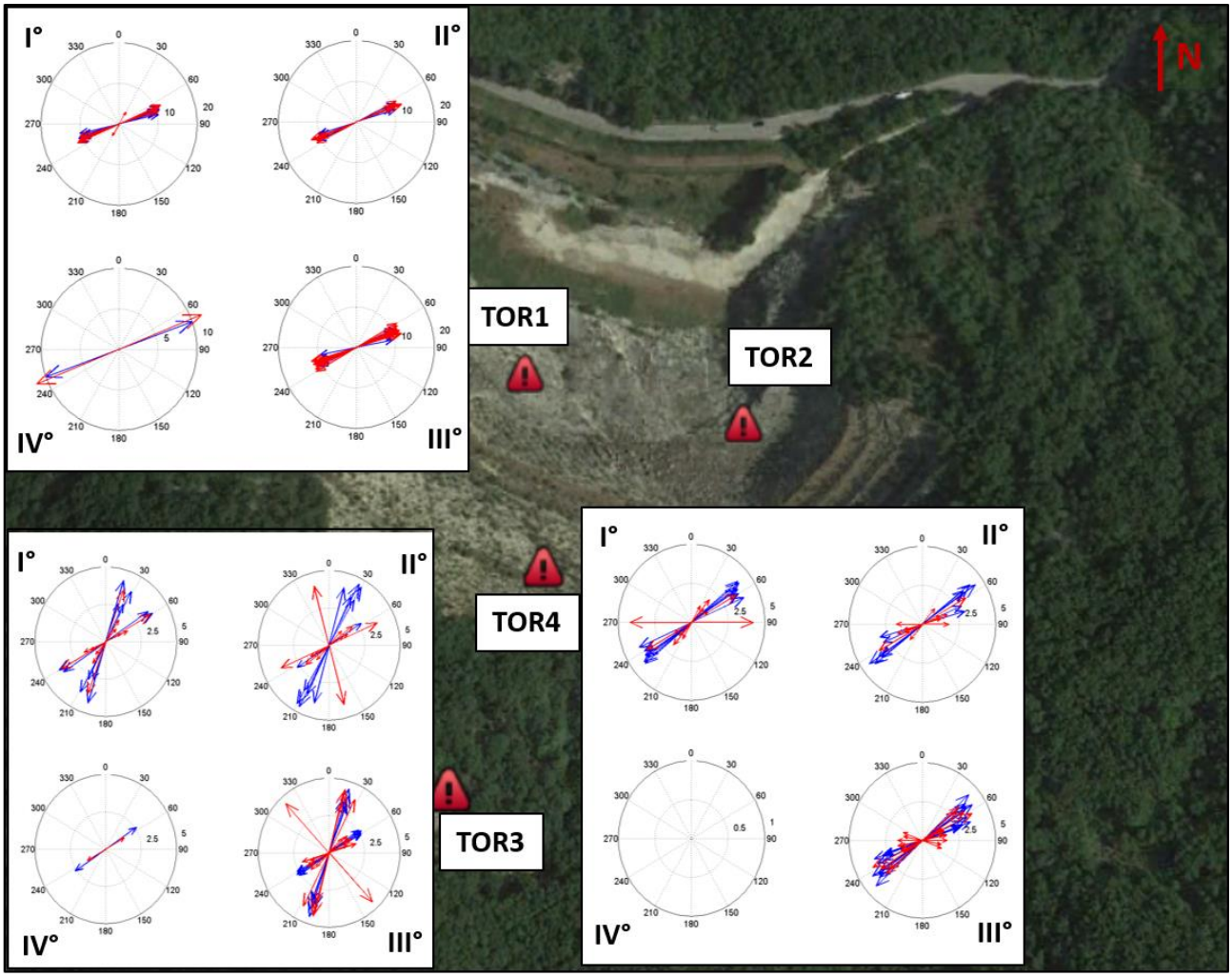

Figure 43 – Polarization plot of TOR1, TOR3 and TOR4. Blue arrows stands for $HVSR_N$ while red arrows are related to the $HVSR_{EQ}$; the arrow length is linked to the frequency peak amplitude value.

Site with TOR1 and TOR4 exhibit a similar directivity pattern, oriented at around N60°E. This pattern is common to both earthquake and noise wavefields and, for the case of earthquakes, it is insensitive to the source back-azimuth. These observations lend strong support to the hypothesis that the marked polarization observed at sites located within the quarry is mainly sensitive to and has a parallel relationship with the dominant fracture orientation (Figure 43).

Burjànek et al. (2010, 2012) point out that the ambient noise polarization is at about 90° angle to the observed fractures that are perpendicular to the sliding direction. Similarly, the polarization angle at TOR1 and TOR4 is perpendicular to the main fracture, which appears in accord to the above mentioned results but in contrast with the studies of Panzera et al. (2013). It is possible to conclude that the polarization angle at those stations is predominantly influenced by the fractures system. On the other hand TOR3, which is located at the top of

the quarry, and outside the unstable area, shows two different main polarization angles (30° and 60°). For this case, both topographic features and anisotropy of the medium are probably not sufficient to overwhelm the original polarization of the wavefield as resulting from variable source back-azimuth and/or mechanisms.

4.2 Monitoring of the temporal variations in medium properties

Using microseismic results delivered in continuously provides a 4D record of seismicity in the landslide area, rather than the individual time snapshots obtained through 2D or 3D active seismic methods. Continuous monitoring of the selected parameters offers a kind of "video recording" of what is happening nearby and in the monitoring area.

This section presents results from the temporal tracking of the wavefield parameters derived from application of HVSR and NCF methods to the continuous data streams. Changes in HVSR peak frequency and amplitude, or in the delay times of the NCF coda portions indicate variations in the seismic velocities, which in turn can be related to changes in the local stress condition, fluid content and/or cracking of the propagation medium. Unrevealing such variations is therefore a crucial step toward our ability to forecast failures of the unstable body under surveillance.

4.2.1 HVSR and HVSR directivity temporal variation

The resonance frequency peaks determined using the H/V method described above (Chapter 3.3.1) are shown for each station throughout the whole monitored period (Figure 44, 46, 48).

The HVSR evaluated at TOR1 exhibits the highest amplitudes for over the frequency band between 4.5 and 13 Hz with a stable peak around 10.5 Hz whose amplitude is generally slightly above 2 (Figure 45).

Throughout the observation period, both peak amplitude and frequency do not exhibit any particular trend, with the exception of a slight amplitude increase in between January and mid-March, 2013.

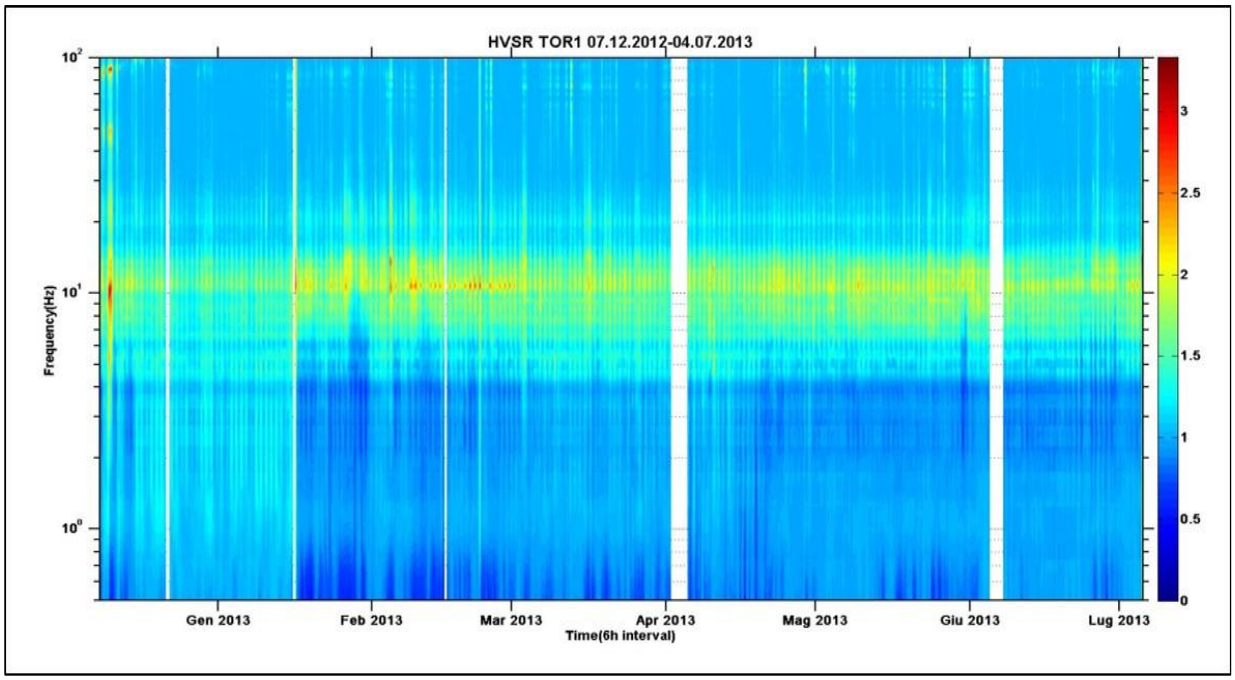

Figure 44 – Spectrogram of H/V ratio recorded at station TOR1 for the period between December 2012 – July 2013.

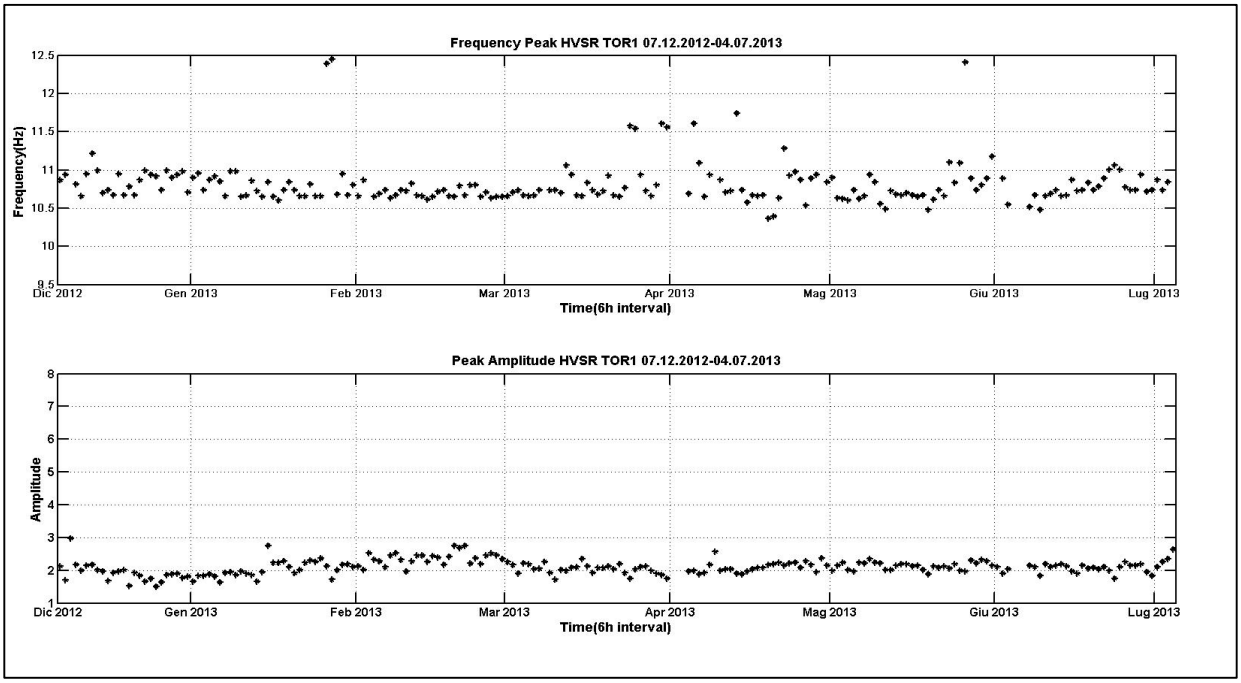

Figure 45 – Station TOR1**.** Top**: t**rend of HVSR frequency peak. Bottom: amplitude value.

The HVSR at TOR3 is characterized by more closely spaced peaks of amplitude higher than 2 and coalescent into a spectral plateau (spanning the 2.5 - 6 Hz frequency band).

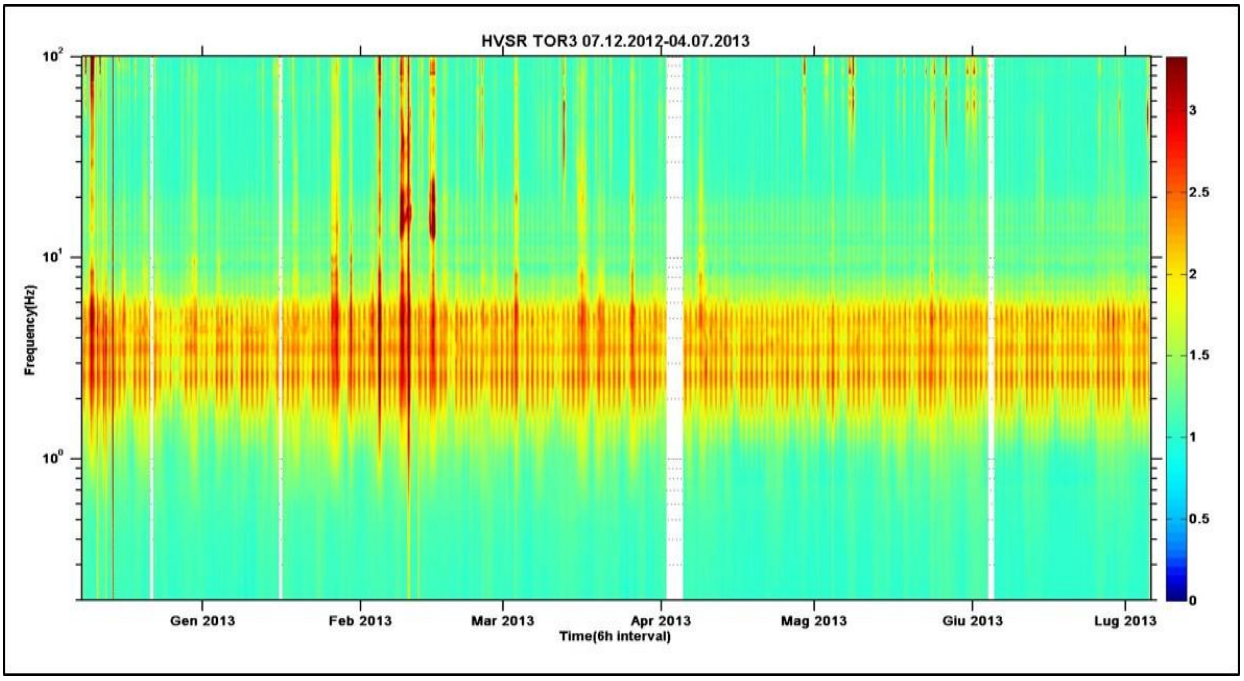

Figure 46- Spectrogram of the H/V ratio recorded at station TOR3 for the period between December 2012 – July 2013.

The main peak is generally at 2.5 Hz but occasionally it alternates with another peak at frequency 5 Hz (Figure 47), suggesting that the medium properties are likely subjected to slight, periodic variations potentially related to temporary fluctuation in water content that influences the propagation velocity.

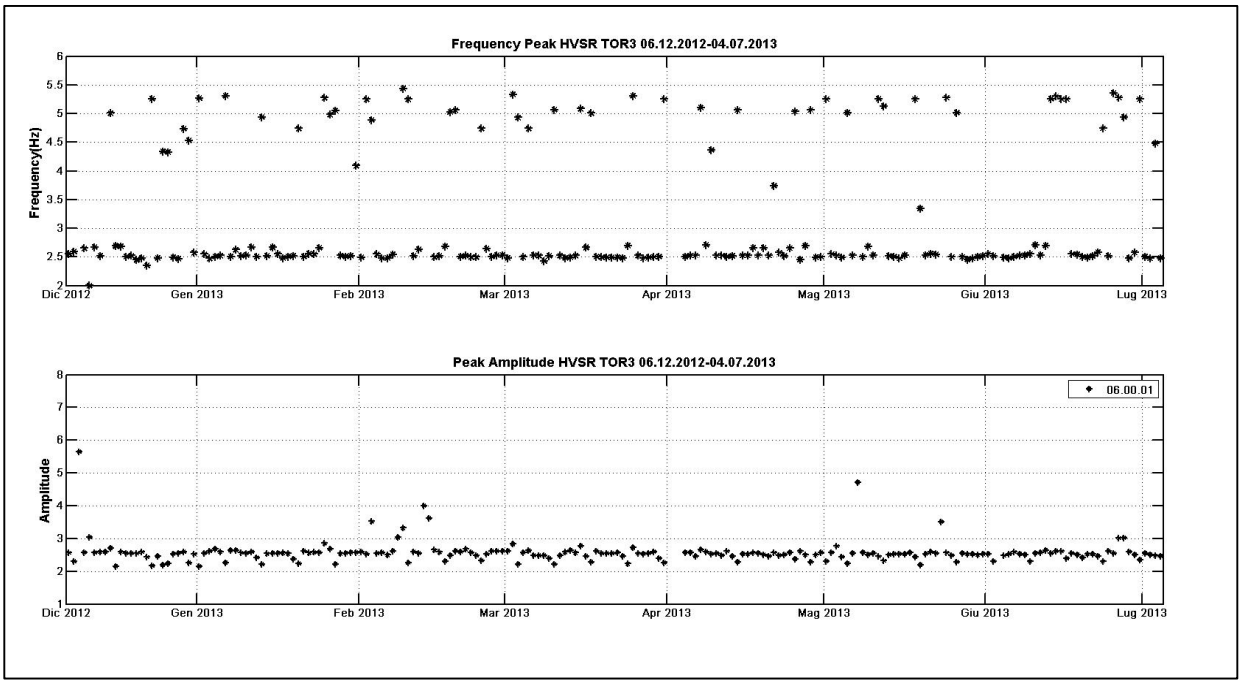

Figure 47 - Station TOR3**. Top: t**rend of HVSR frequency peak. Bottom: amplitude value.

At TOR4, the HVSR exhibits two main frequency peaks at frequencies of about 2.7 Hz and 5.5 Hz. The amplitude of these peaks varies according to a characteristic daily behaviour, in which the largest amplitudes of noise is larger. This could be related to (a) an artefact related to the internal electronic noise of the instrument, whose effects become relevant when the ground vibrations have very low amplitude, such as night time or during the week-end, or (b) variations of the noise wavefield, as a consequence of the activation of different sources related to anthropogenic activities.

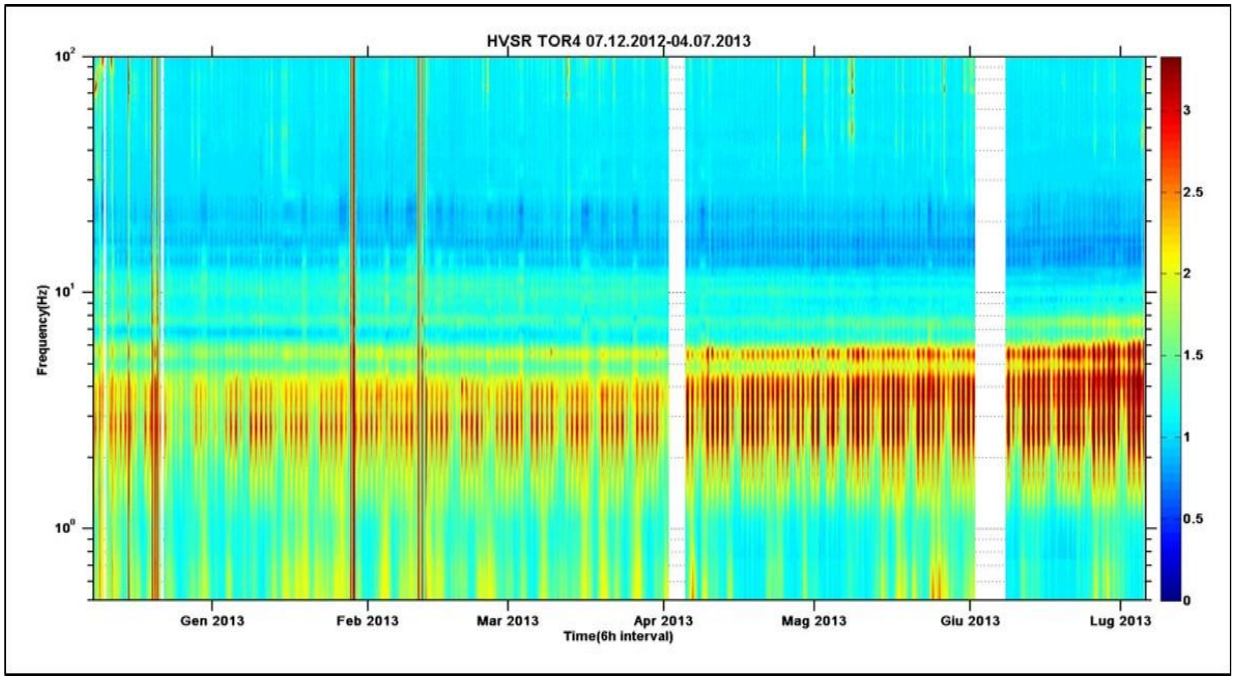

Figure 48 - Spectrogram of the H/V ratio recorded at station TOR4 for the period between December 2012 – July 2013.

Beginning on April, 2013, the amplitudes of these peaks start increasing, and by the end of the monitoring period they attain values around 5, i.e. about 65% greater than those observed during the early phases of the experiment (Figure 49). Such amplitude increase is likely to reflect a corresponding increase of the impedance contrast between the unstable mass and the underlying solid bedrock. However, the peak frequency remains stable in time, indicating that both thickness and velocity of the shallowest layer remain substantially unchanged. Thus, an increment in the velocity and/or density of the underlying layer must be invoked in order to explain the inferred impedance variations. Possible phenomena provoking the velocity increase will be discussed throughout the next section.

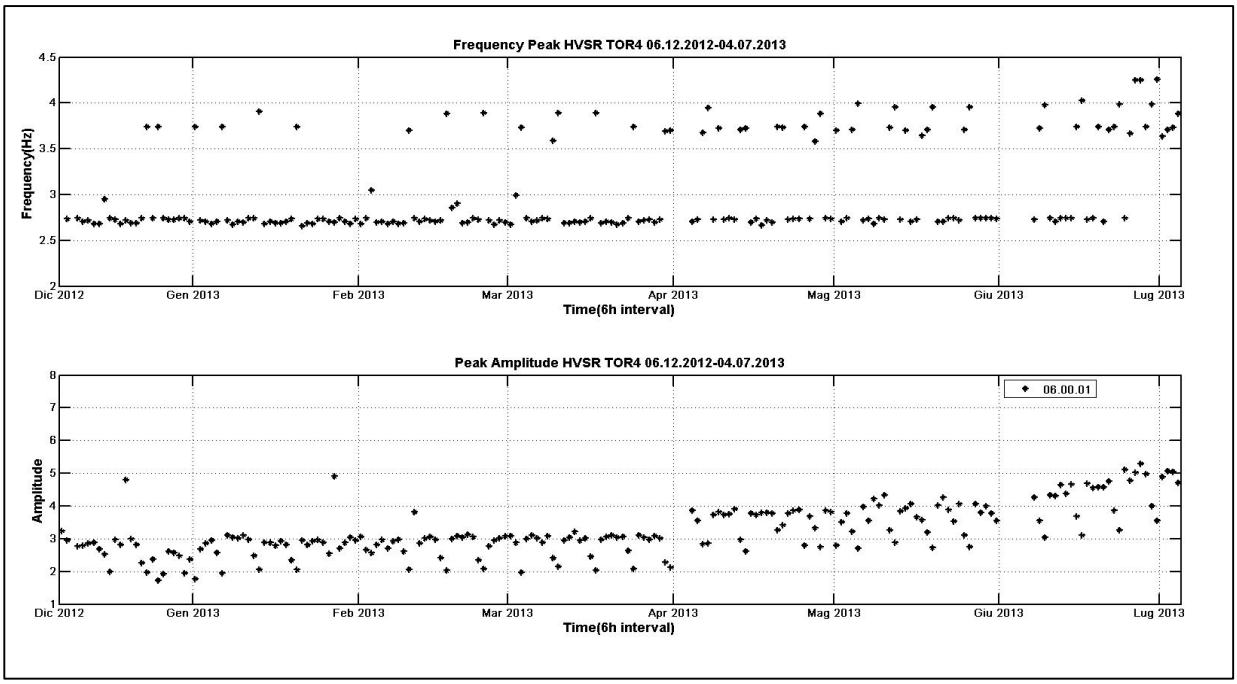

Figure 49 - Station TOR4**.** Top**: t**rend of HVSR frequency peak. Bottom: amplitude value.

I also evaluated the HVSR directivity throughout the 7 months of recording. As an example, contour maps in Figures 50 and 51 compare sample results obtained on December 2012 and July 2013, respectively. For the two different intervals, the directivity properties at stations TOR1, TOR2 and TOR3 are substantially unchanged. At TOR4 the polarization direction between the two periods change slightly, but for the later interval directivity is much clearer as a consequence of the amplitude increase of the horizontal components, as also manifested by the growing of the HVSR peak. This suggests that the observed temporal variations in the HVSR plots are not due to changes in the distribution of active sources; if this would be the case, the polarization direction should most likely have changed consequently.

Results from HVSR analyses can be summarized as follows:

(1) There are clear alignments of quasi-constant or slowly varying contiguous frequencies whose values depend on the considered station, denoting a coherent but peculiar situation for each acquisition point.

(2) The stations located on the sliding mass and at the head of it, potentially loosened section, show an amplitude peak which is sharper and larger than those observed at the stations settled downstream.

(3) At TOR4, the amplitude variations of the HVSR cannot be unequivocally interpreted; however, the overall stationarity of the polarization properties suggests that those

changes most likely reflect a variation in the acoustic properties of the medium, rather than a change in the distribution of noise sources.

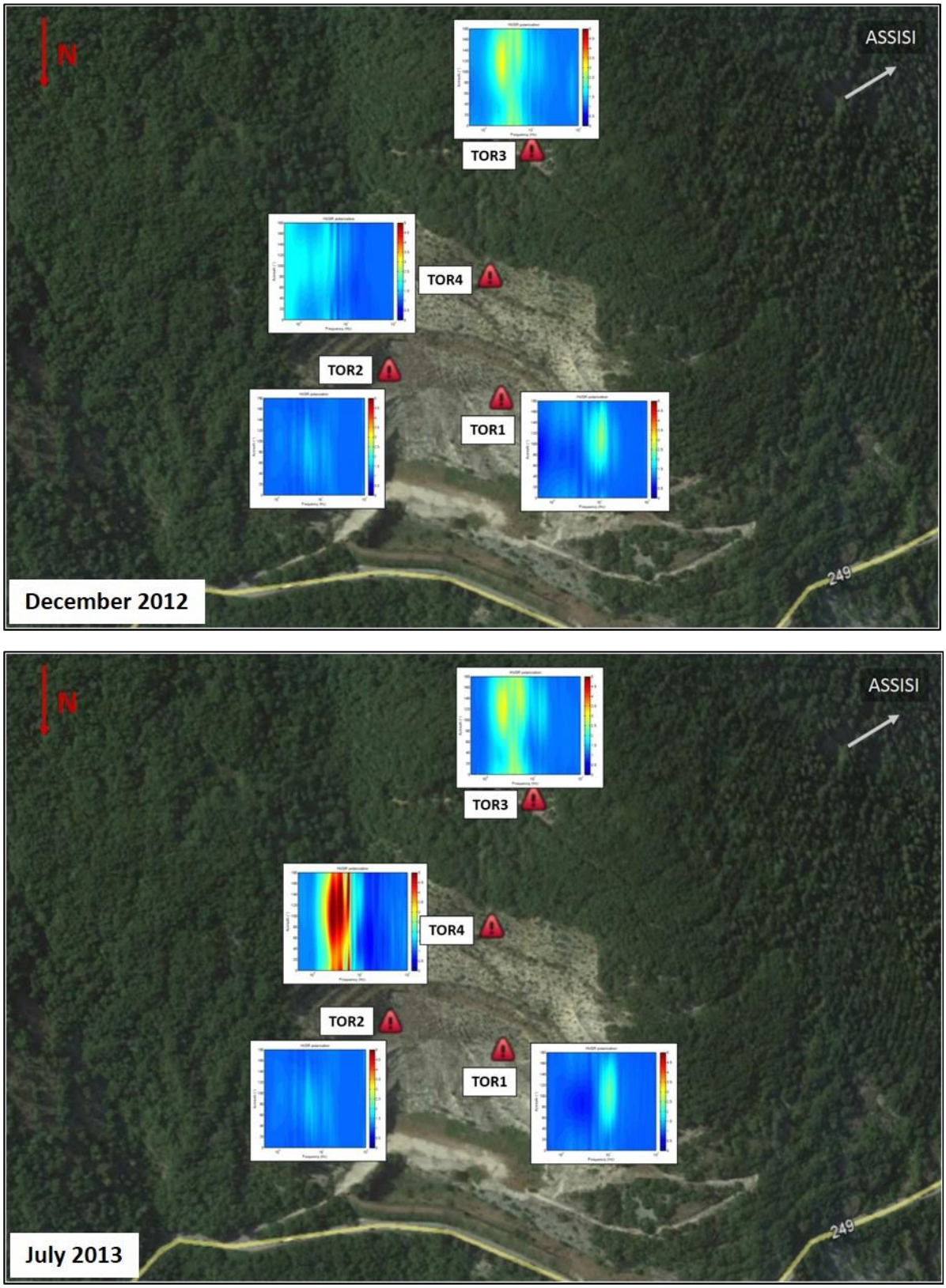

Figure 50 – Main peak directivity contour maps observed at the four stations in December 2012 (top) and July 2013 (bottom).

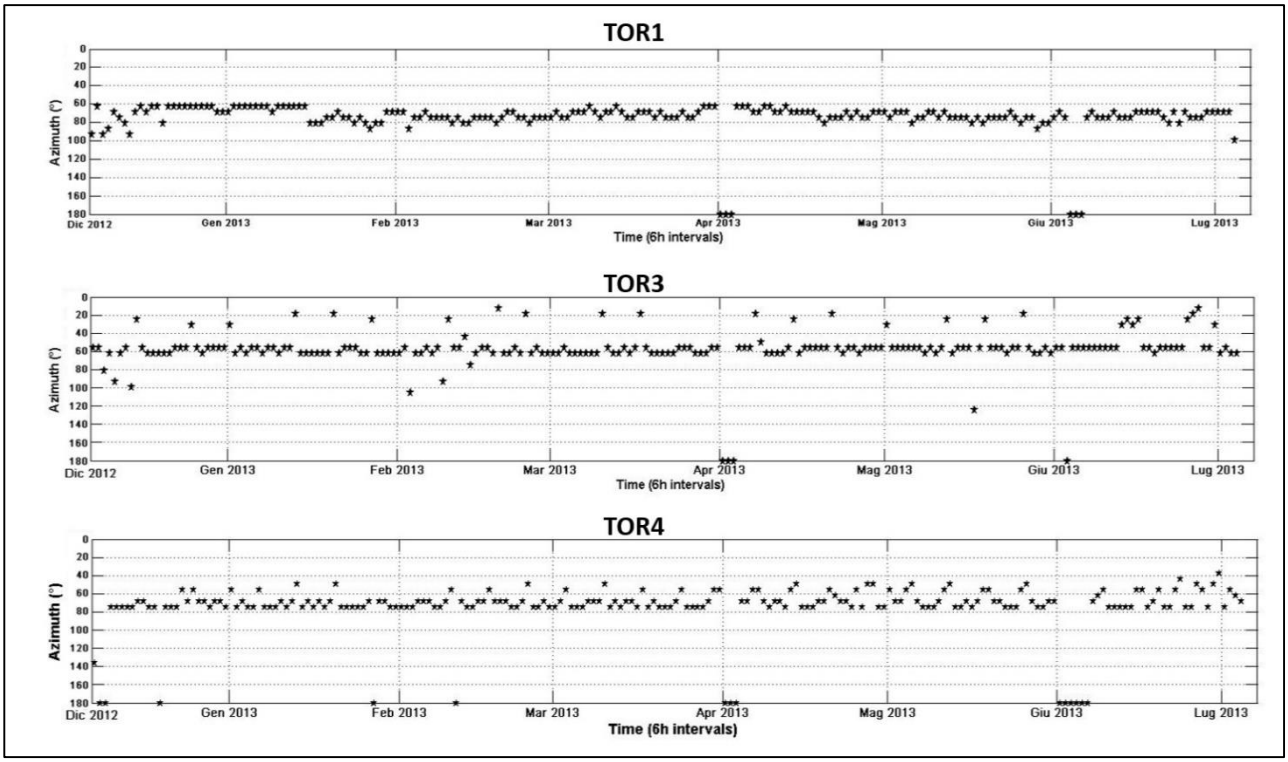

Figure 51 – Azimuth variation for the polarization angle observed at station TOR1, TOR3 and TOR4. No significant changes is recorded.

4.2.2 Coda Wave Interferometry of the NCFs

This analysis uses the vertical component signals of the four stations and consists of three main steps:

1. Computation of ambient seismic noise cross-correlation function (NCF) between signals from all possible independent station pairs
2. Average of the NCFs over 6-hour-long intervals for the entire monitoring period (840 intervals; Figure 52);

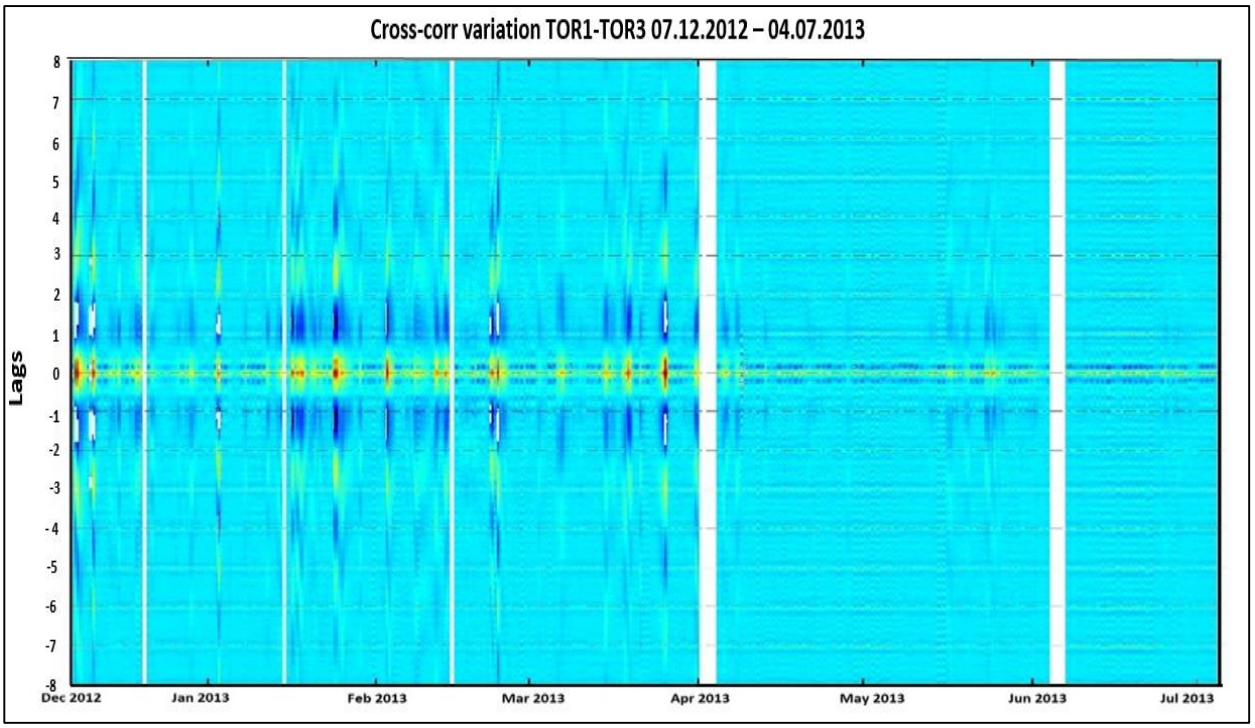

Figure 52 – Cross-correlation function evaluated between TOR1 and TOR3 from 07 December 2012 to 04 July 2013.

3. Coda-wave interferometry applied to daily-averaged cross-correlation functions for each pair of stations, in order to detect small velocity variations in the propagation medium within in between and around the two acquisition sites.

As in Brenguier et al. (2008b), I use continuous data recording from December 2012 to July 2013 to evaluate the possible application of this method in real-time monitoring of rockslide. In order to recognize temporal velocity variations in the medium, I compared the "current" CF (CF(i), i ranging from 1 to 840) with a "reference" CF (CF(1)) that corresponds to the NCF of the first day of monitoring considering a 5-40 Hz frequency band (Figure 53, top panel). The cross-correlation was evaluated on selected number of time window (0.5 sec length) sliding along the pair of NCFs: for each window position, the delay time between the two signals is retrieved from the lag at which the cross-correlation attains its maximum value. These delay times are then plotted versus the corresponding interval times (Figure 53, middle panel), and eventually least-square fitted by a line whose slope corresponds to the velocity variation for that particular pair of stations and recording times (Equation 1.3; see Figure 53, middle panel).

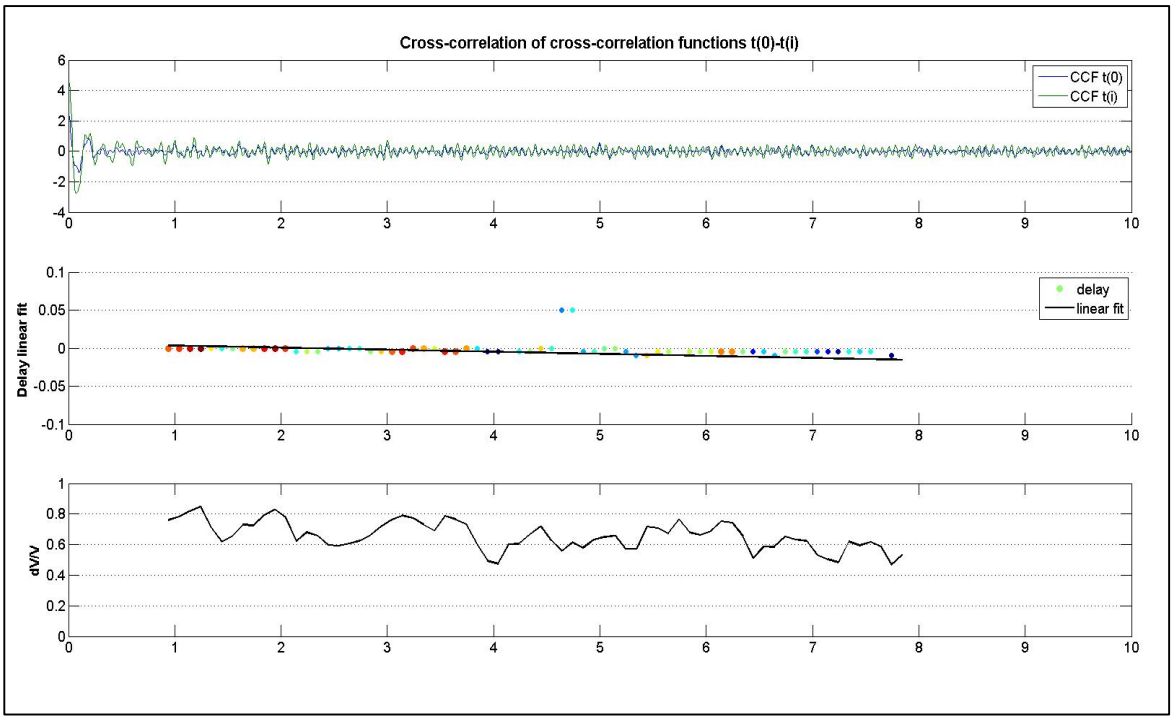

Figure 53 – Top: "current" CF (CF(i)) and "reference" CF (CF(1)) after averaging causal and acausal part. Middle: delay retrieved for each window through the chosen interval lag; the linear regression is shown as a straight black line. Bottom: maxima of the cross-correlation functions evaluated at different lapse time in the NCF coda.

The data were processed on different lag time intervals of the resulting NCF to detect the coda portion most influenced by the scattered wavefield. All the intervals are chosen in between 0 s and 10 s lags because of the very small stations interdistance and the high medium propagation velocity. Despite the evidence of a change in the shape of the cross-correlation function (Figure 52) that temporally corresponds to the TOR4 HVSR amplitude variation (deflection from 15 December 2012 to 15 January 2013 and the increase starting from early April 2013), the results obtained over the lag time intervals of 0.7-8 s, 3-8 s and 5-7 s (Figure 54, 55 and 56, respectively) show an extreme variability; in general, the highest velocity variation are observed for shorter interval lag.

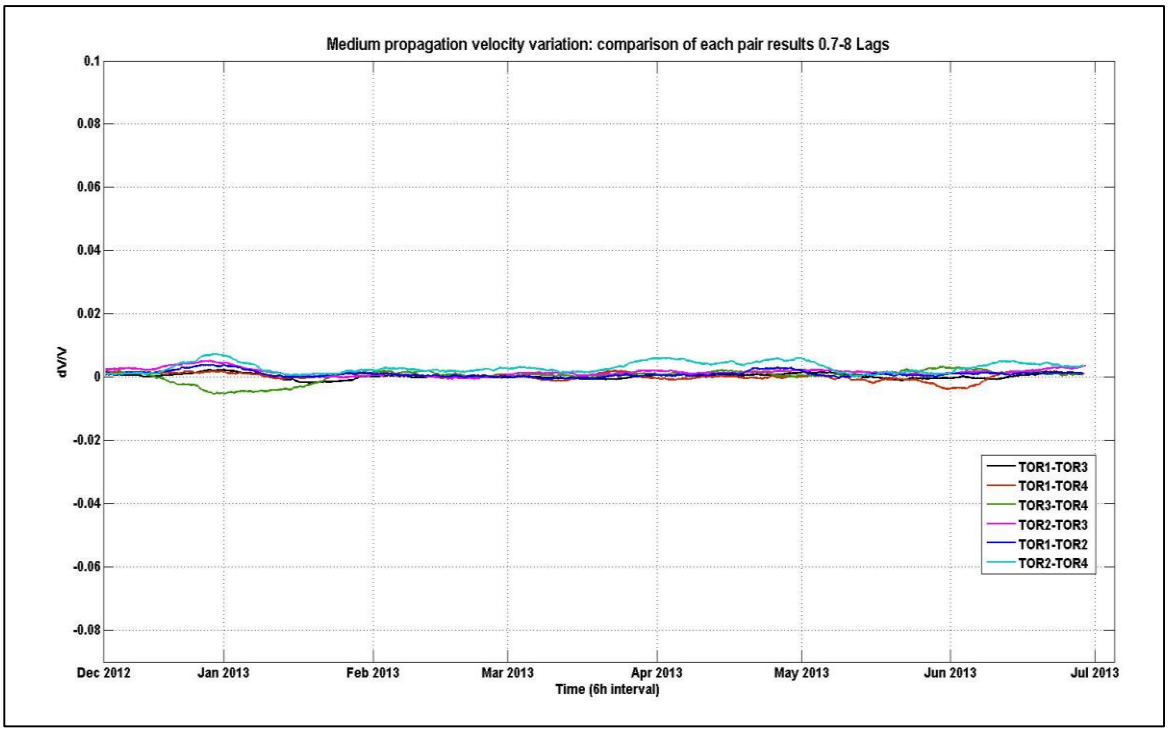

Figure 54 – Temporal velocity variation for each station pair over the 0.7-8 s lag time interval. Frequency band: 5-40 Hz.

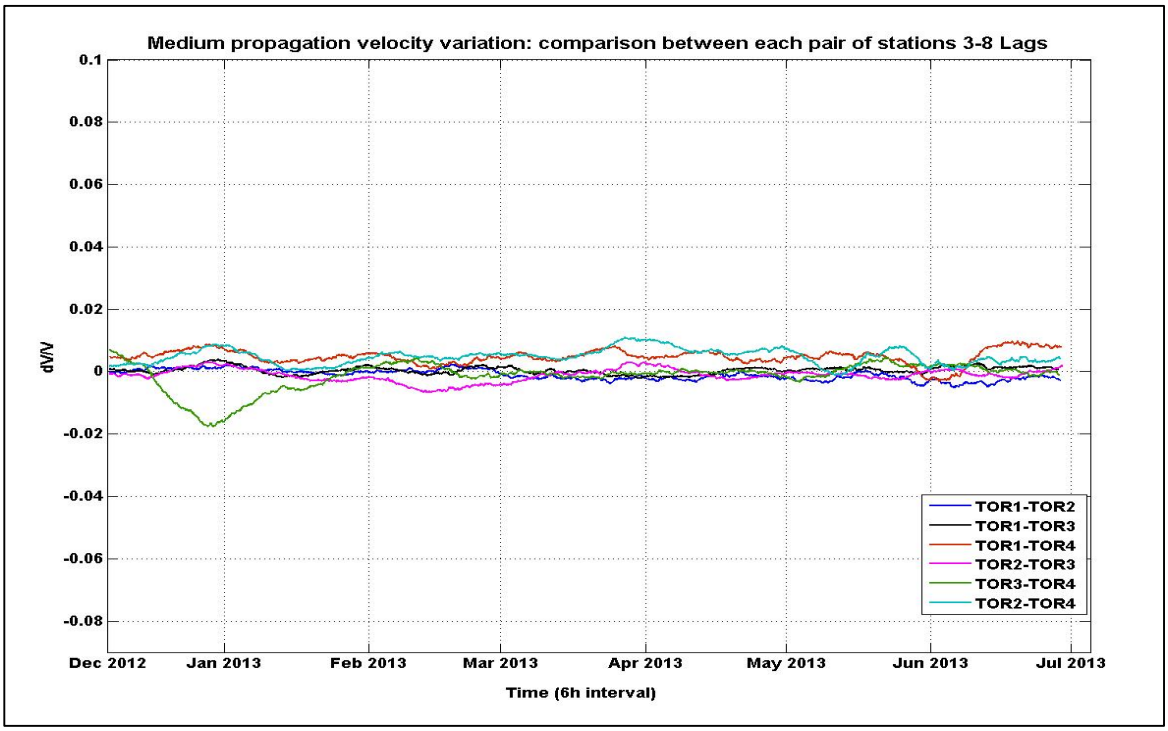

Figure 55 – Temporal velocity variation for each station pair evaluated over the 3-8 s lag time interval. Frequency band: 5-40 Hz.

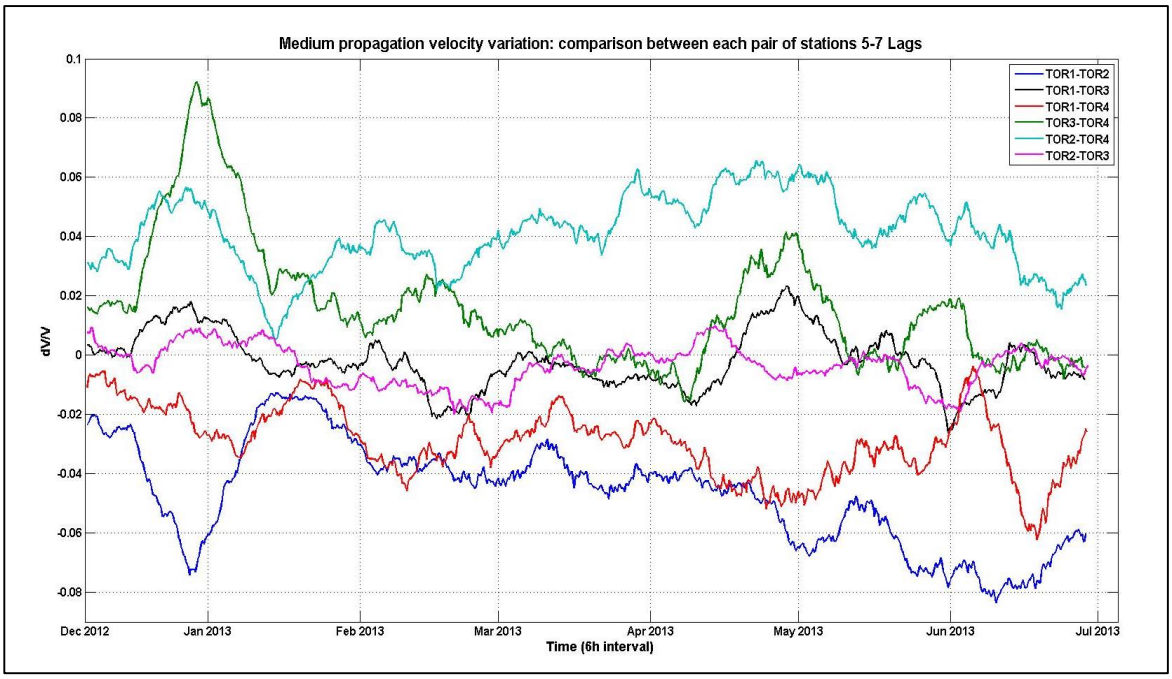

Figure 56 – Temporal velocity variation for each station pair evaluated over the 5-7 s lag time interval. Frequency band: 5-40 Hz.

I also tried to use different window lengths and frequency bands (Figure 57 and 58). For all the cases, there are no obvious evidences of velocity changes which can be directly compared to those inferred from monitoring of the HVSR amplitude at TOR4. Such variations would be expected at least in the analysis of the cross-correlation function between TOR1 and TOR3, whose joining line crosses TOR4.

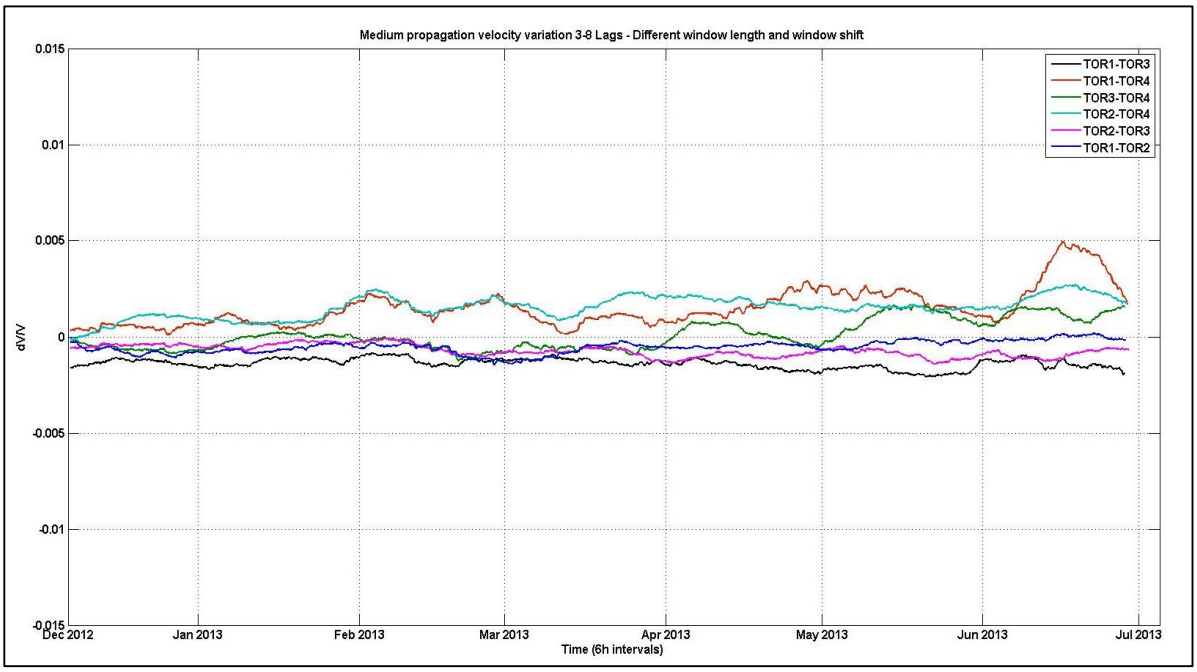

Figure 57 – Temporal changes in the medium propagation velocity inferred from cross-correlation technique for all station pairs using a 0.1 sec moving window instead of a 0.5 sec window. Frequency band: 5-40 Hz.

The best matches with previous results are obtained using: (1) a very short moving window (0.1 s) and, (2) a 2-10 Hz frequency band for the 3-8 s lag time interval for the TOR1-TOR4 pair (red line, Figure 57-58). These data indicate a velocity increase of about 0.5% starting on early April, 2013, and on early June, 2013 lasting to the end of the monitoring period in good agree with the dates on which is observed the upward trend of the HVSR amplitude at TOR4. Though the analysis previously shown indicate an extreme sensitivity of the interferometric method to the input parameters (window length, lag time interval and frequency band).

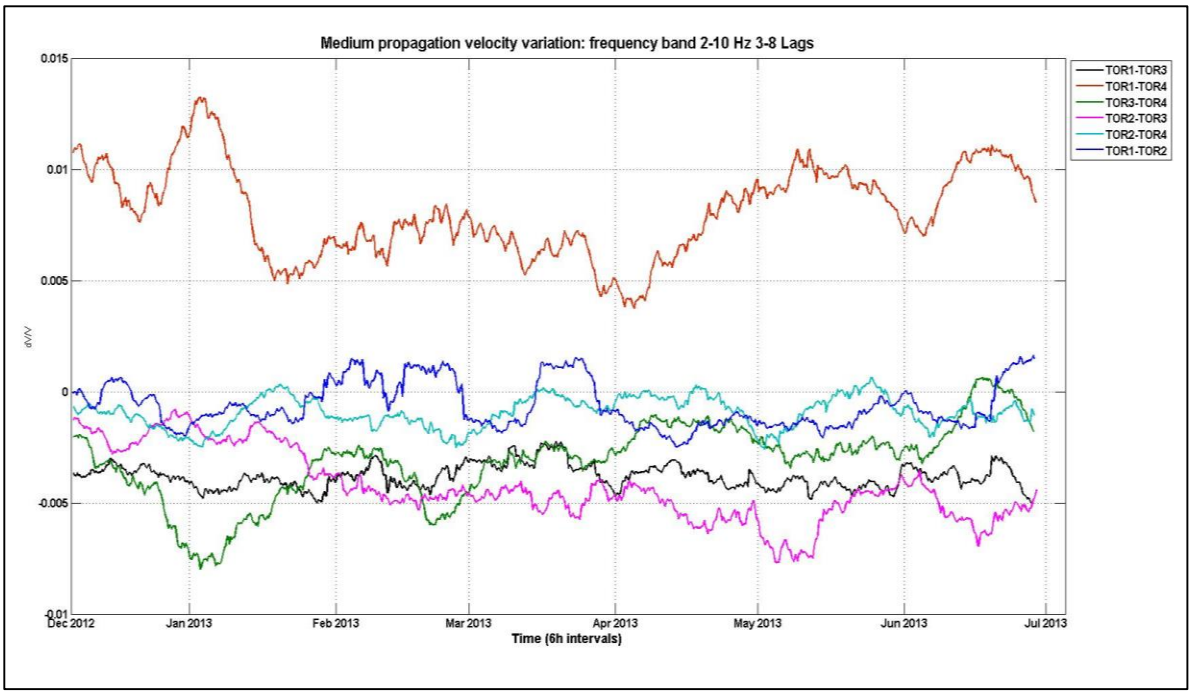

Figure 58 – Temporal velocity variation for each station pair evaluated over the 3-8 s lag time interval. Frequency band: 2-10 Hz.

4.2.3 Comparison with other available parameters (P, T, displacement, interferometric campaign).

At Torgiovannetto, the rain amounts and temperature variation were monitored with a meteorological station, located inside the quarry area on the right edge of the sliding wedge, equipped with an automatic rain gauge and a thermometer that stored data with a sampling interval of 5 minutes. At least other 3 meteorological stations or rain gauges are located within 20 km of the rockslide (Figure 59). The closest one is 5 km of the rockslide at Santa Maria degli Angeli (SMA), the second one is located at Palazzo Assisi, 7 km away from the

quarry and the farthest one is located in Perugia. Even if all of them has a sampling interval of 1 day they can be used to check the reliability of the Torgiovannetto station.

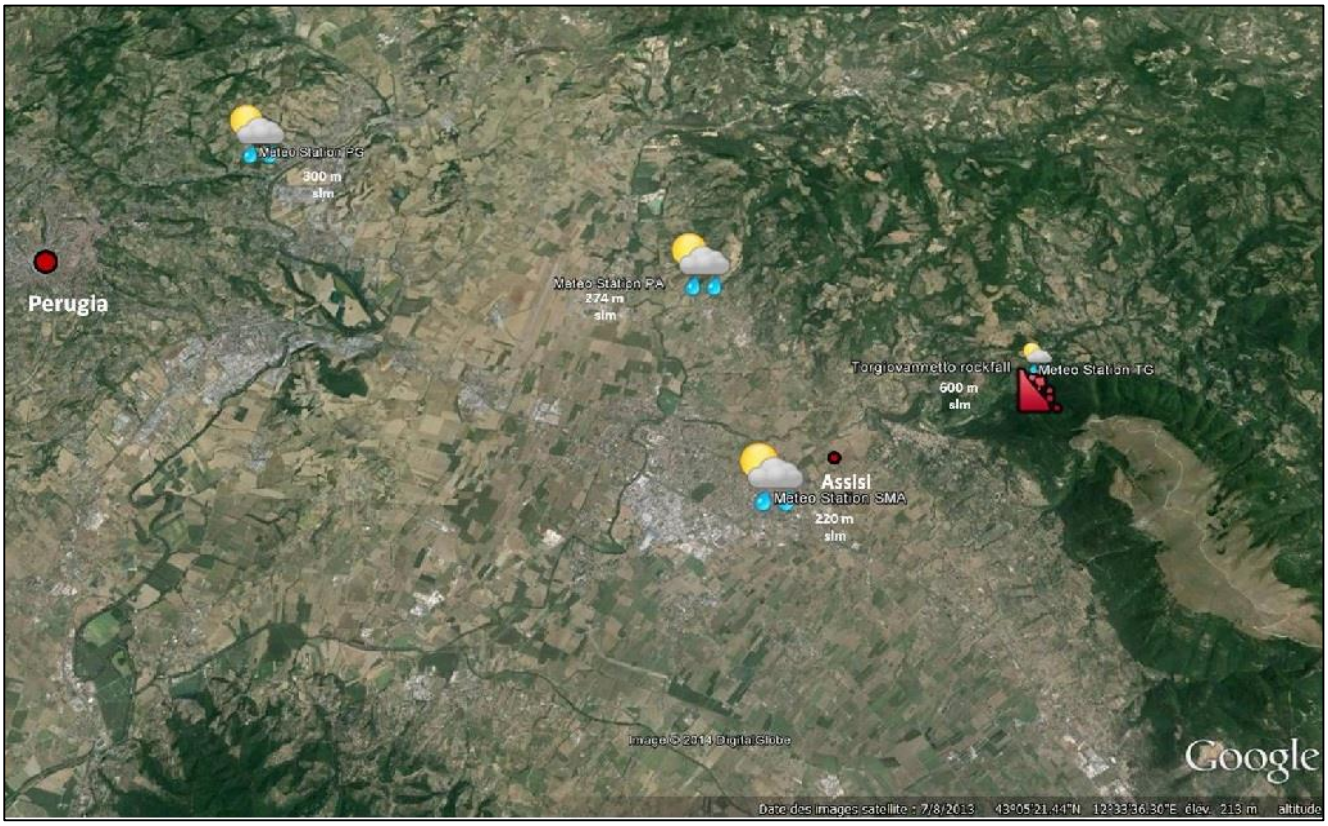

Figure 59 – Localization of the Torgiovannetto rockslide and metereological stations (SMA, PA and PG) used for the validation of the data acquired by the meteorological station located at the test site.

Figures 60 and 61 show the four datasets: both for precipitation and temperature the correlation among the different time series is very high, indicating the reliability of the data acquired at the test site. Therefore, then for the following comparison with the seismic data I will use the meteorological station deployed on the landslide area.

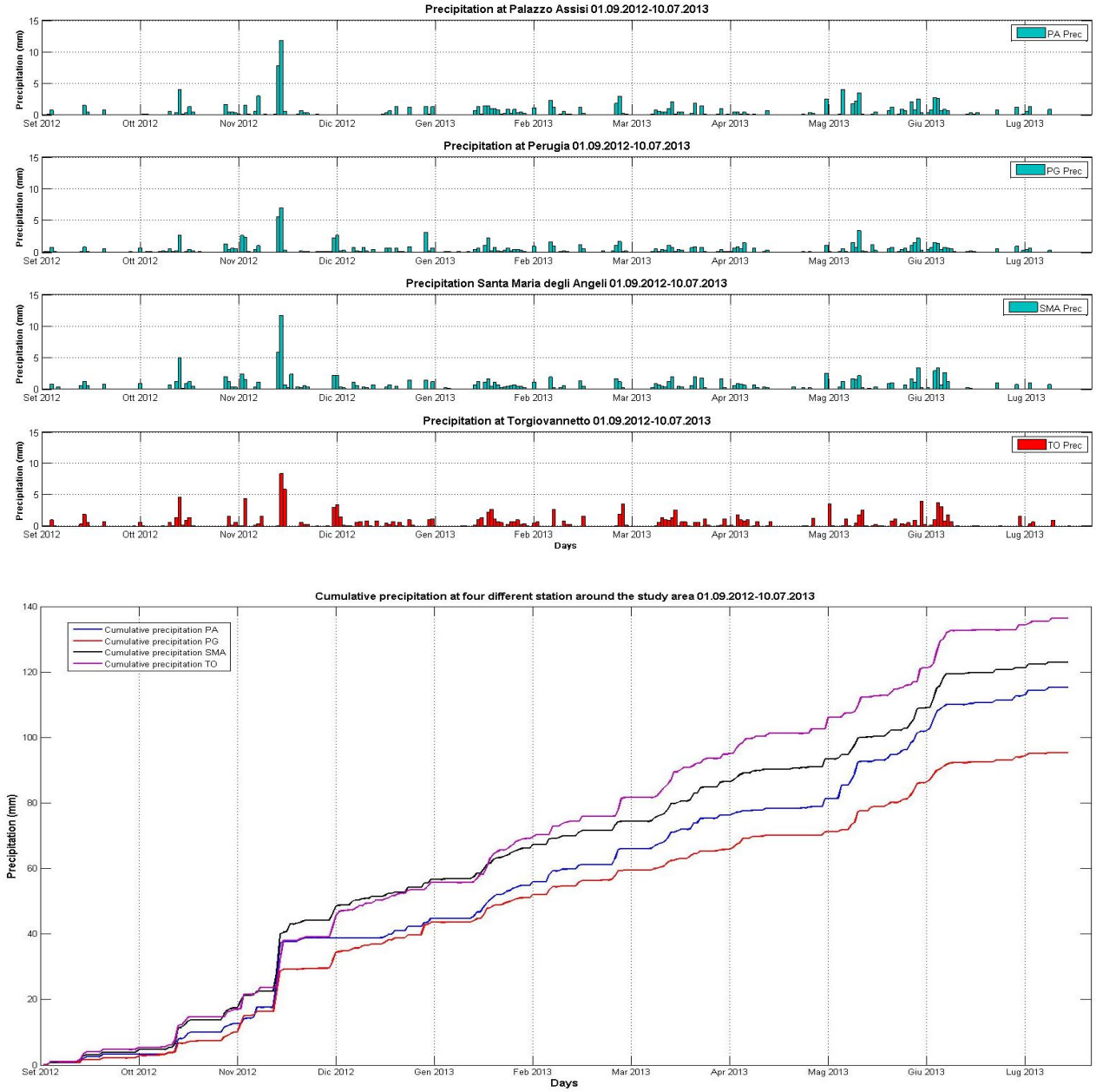

Figure 60 – Daily (upper panel) and cumulated rainfall (lower panel) at the four stations. Upper figure, from top to bottom: data recorded at Palazzo Assisi, Perugia, Santa Maria degli Angeli and Torgiovannetto.

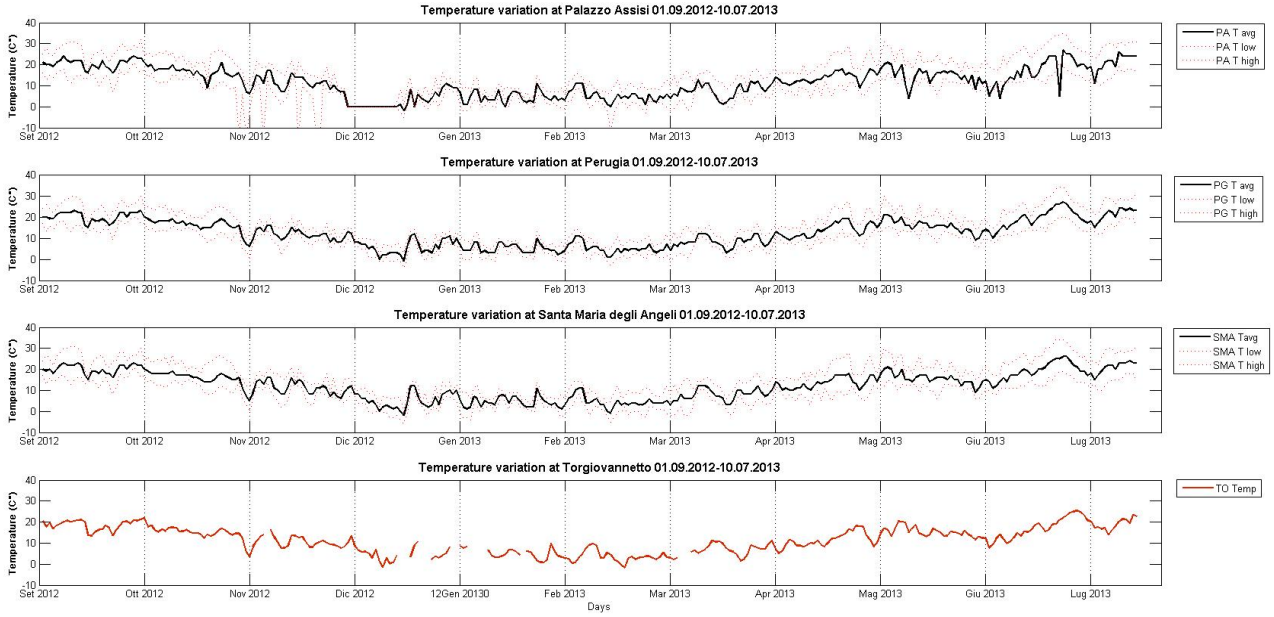

Figure 61 – Daily average temperature recorded at the four stations. From top to bottom: data recorded at Palazzo Assisi, Perugia, Santa Maria degli Angeli and Torgiovannetto.

The extensometric wire devices (Figure 62) installed at the quarry proven to be very useful in recording changes in the rate of displacements that can be directly related to the rainfall records (Intrieri et al., 2012).

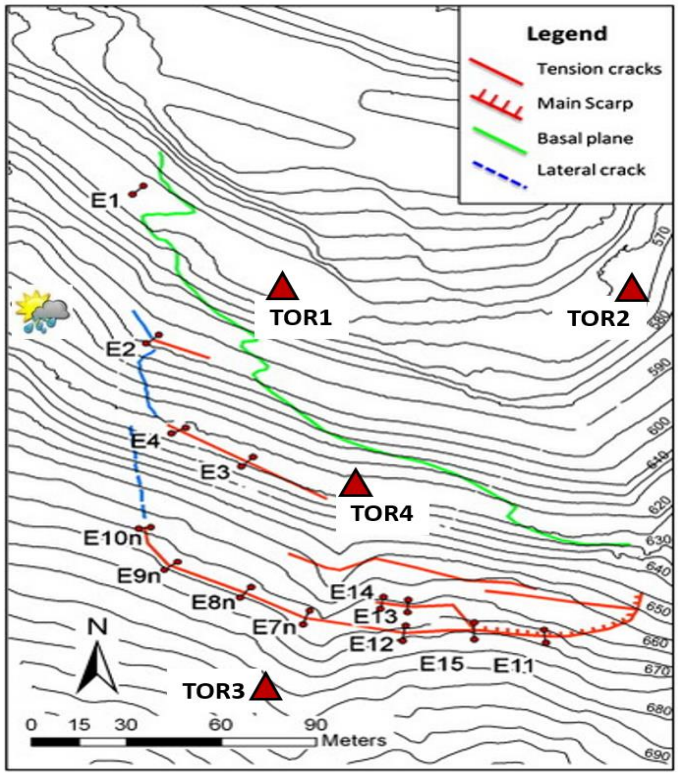

Figure 62 – Location of the extensometers network and of the seismic stations installed at the Torgiovannetto rockslide. The main fractures are also shown.

The whole data set covers the time span from December 2012 to July 2013, with few missing data due to power issues. Throughout the entire period encompassed by our measurements, the overall displacements are quite small (on the order of a few centimeters). The highest deformation rates are observed from February 2013 to the second half of April 2013, especially at E11 and E8.

The highest velocities are observed in the eastern sector of the back fracture (sensor E11) and decrease almost regularly toward sensor E10, located at the western border of the quarry; this is consistent with the results from two previous short-term ground-based interferometric synthetic aperture radar (GB-InSAR) monitoring campaigns performed in 2006 and 2008 (Figure 63). The only exception to this general pattern is represented by sensor E12 which, in the middle of the main fracture, is characterized by the total absence of movement.

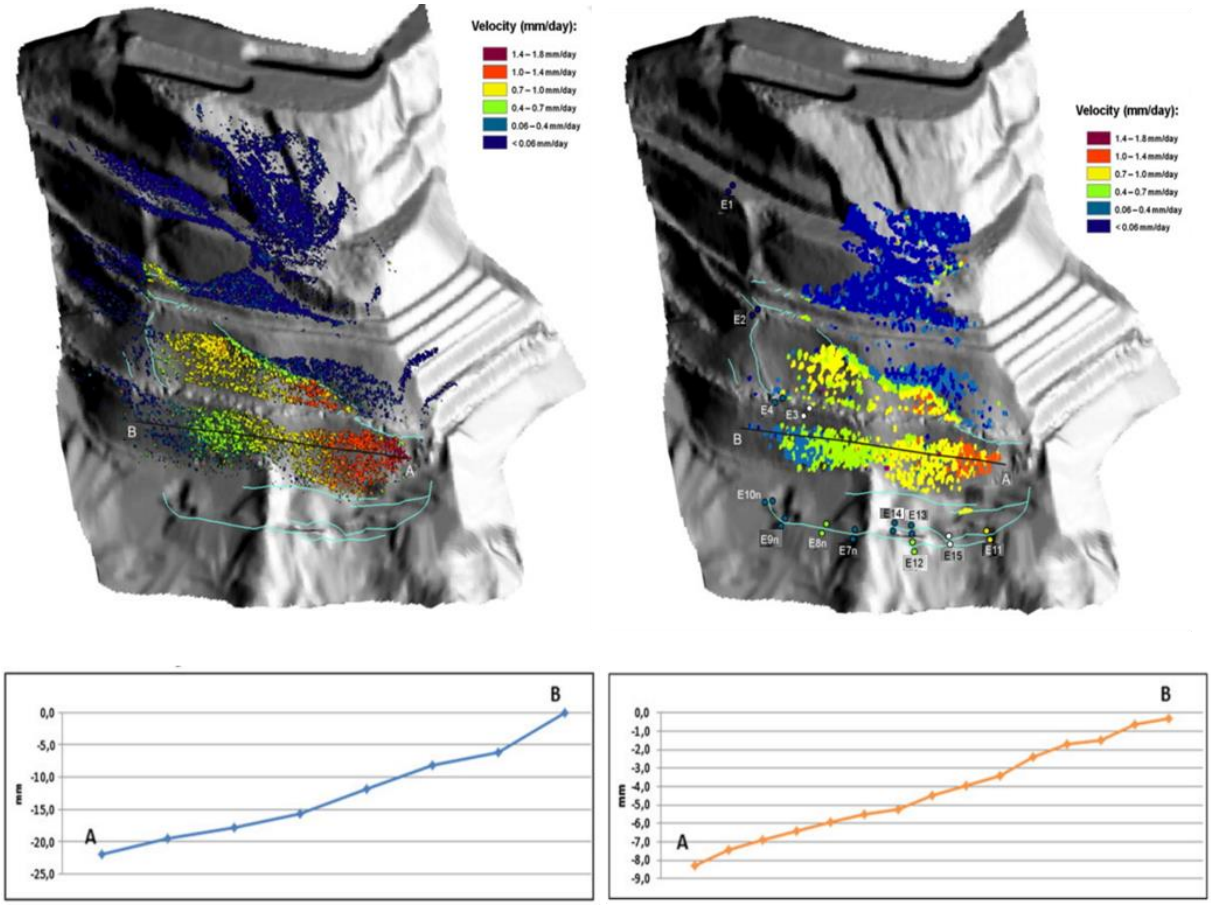

Figure 63 - GB-InSAR velocity map referred to the time intervals from March 29th to April 14th 2006 (on the left) and from 11th to 17th April 2008 (on the right) and longitudinal displacement profiles along the AB scan-line. The values are referred to the displacements along the line of sight. The circles represent the extensometers whose velocities are shown using the same color bar as the map (E15 and E3 are colored in white because they were not installed at that time).

The fracture monitored by E13 and E14 show displacements similar to those of E7 and E9 while E10, E3, E4 and E2 that monitored the fractures in the western and lower part of the quarry show smaller movements. Finally, a very small shortening has been recorded by the lowermost extensometer E1 (Figure 64) that it is compatible with a substantial roto-translation of the sliding block.

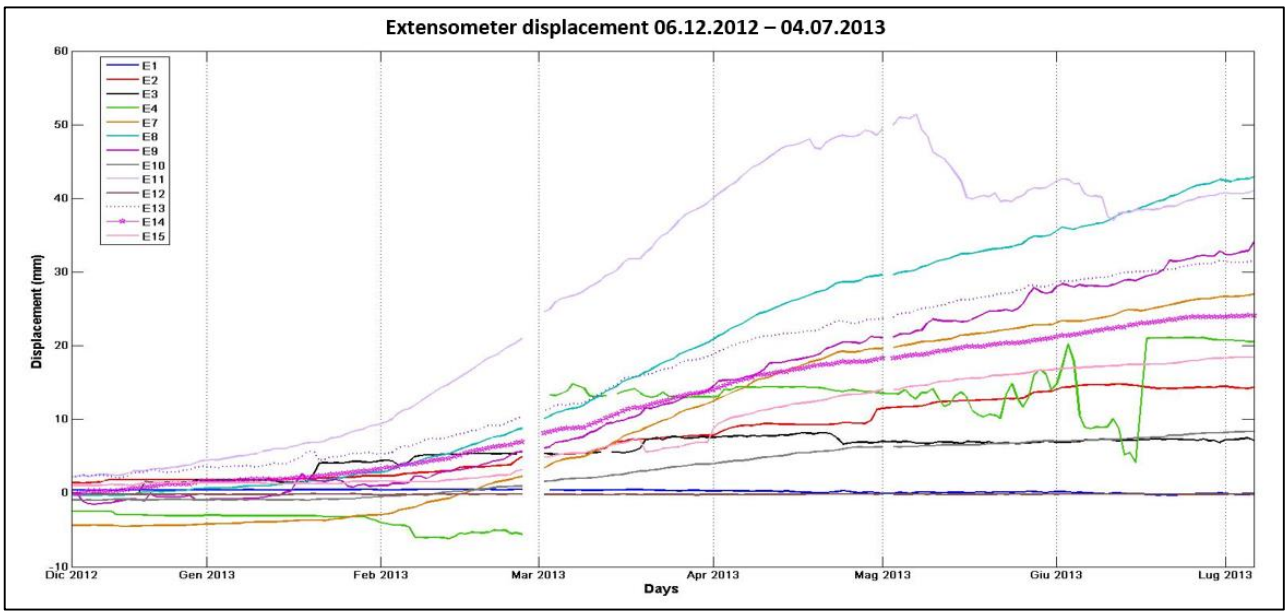

Figure 64 - Displacement data from the extensometers installed at Torgiovannetto. Data referred to the time interval spanning from 06.12.2012 to 04.07.2013.

All extensometer data were individually normalized and compared with the cumulative rainfall in order to highlight possible linear correlation between two different time series. The linear (or rank) correlation (Rho) is evaluated using corr function in Matlab that also provides the results for testing the hypothesis of no correlation against the alternative that there is a nonzero correlation (Pval) supposing that the correlation between two data is significant once if Pval is sufficiently small (< 0.05). Table VI shows the values obtained for each comparison.

Correlation test	Rho	Pval
Cum_RAIN – E1	-0.8674	$9.1381\ e^{-64}$
Cum_RAIN – E2	0.9822	$4.0970\ e^{-150}$
Cum_RAIN – E3	0.8326	$6.7328\ e^{-51}$
Cum_RAIN – E4	0.8296	$1.6040\ e^{-53}$
Cum_RAIN – E7	0.9746	$1.7970\ e^{-134}$
Cum_RAIN – E8	0.9826	$3.7711\ e^{-151}$
Cum_RAIN – E9	0.9833	$7.4087\ e^{-153}$
Cum_RAIN – E10	0.9724	$5.5739\ e^{-131}$
Cum_RAIN – E11	0.8782	$2.9209\ e^{-67}$
Cum_RAIN – E12	0.1336	0.0555
Cum_RAIN – E13	0.9860	$1.1666\ e^{-67}$
Cum_RAIN – E14	0.9845	$2.7311\ e^{-156}$
Cum_RAIN – E15	0.9633	$1.5301\ e^{-118}$
Temp – E12	0.1564	0.0312

Table VI – Correlation and hypothesis of no correlation values obtained for comparison between extensometric data, cumulated precipitation and temperature variation.

By the results it is clear that the deformational field in the upper section of the quarry (E7, E8, E9, E10, E13, E14) and that corresponding to the movements recorded at E2 is strictly related to the seasonal rainfall (Figure 65).

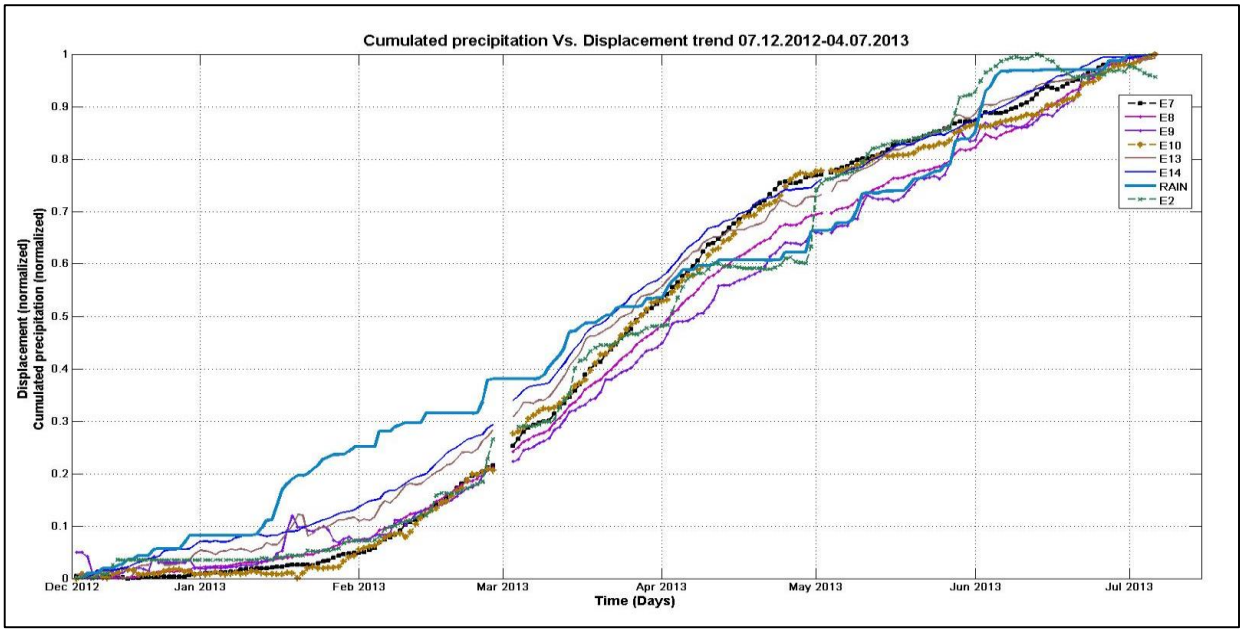

Figure 65 – Comparison between displacement data recorded by the extensometers settled in the upper part of the quarry and cumulated precipitation (normalized data).

Rainfall also seems to have a weaker, but still significant influence, on the deformations measured by E11, E3, E4 and E15 (Figure 66) while an inverse correlation exists with the data recorded by E1 (Figure 67). There is no evidence of correlation for E12 data with the rains trend or with temperature variation (Figure 67, 68).

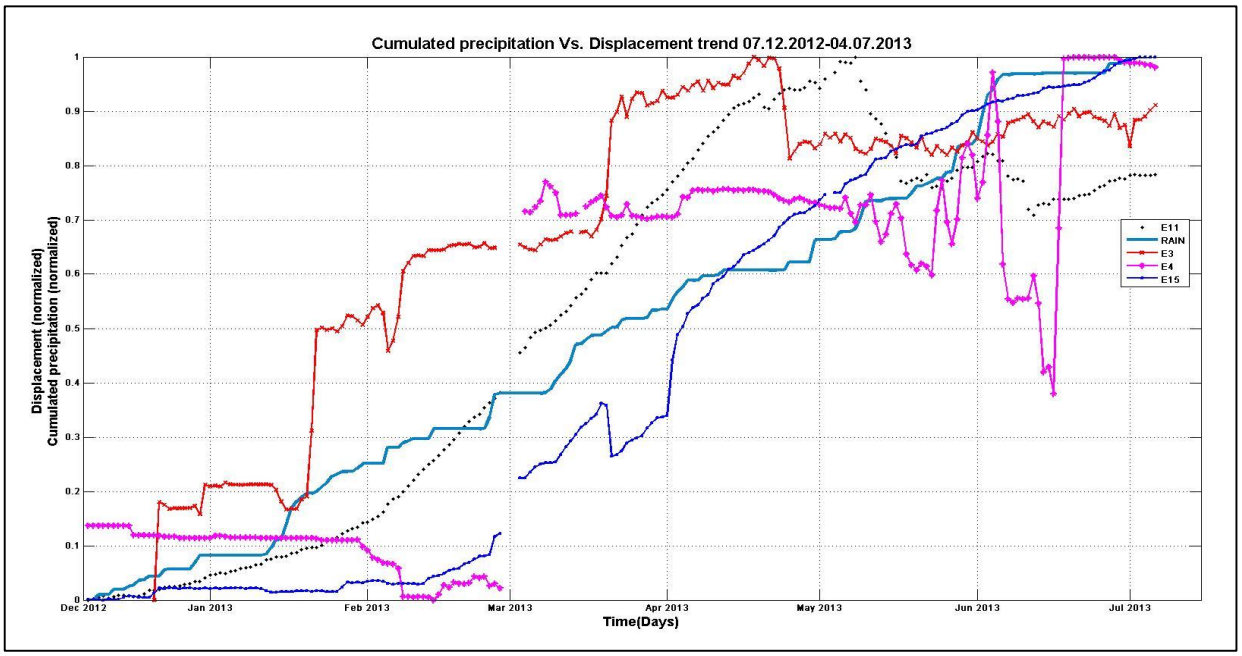

Figure 66 – Comparison between displacement data recorded by the extensometers located in the upper and middle section of the quarry showing a more complex trend and cumulated precipitation (normalized data).

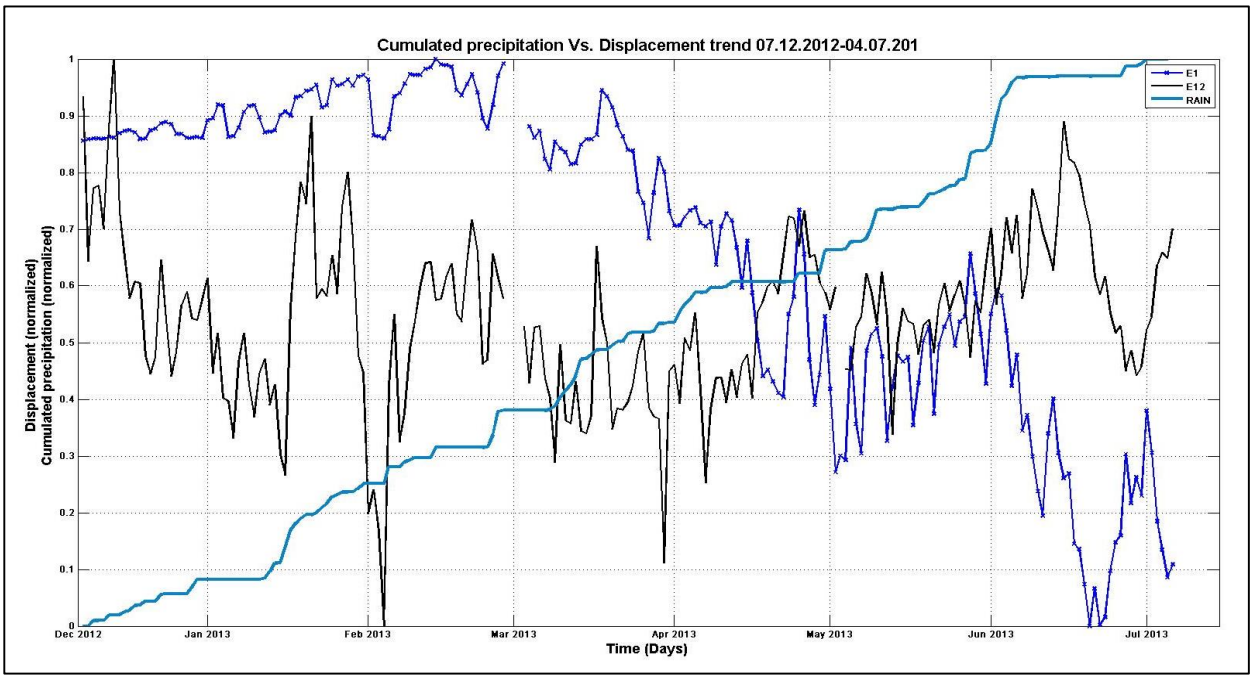

Figure 67 – Comparison between displacement data recorded by the extensometer E1 located in the lowermost portion of the quarry and cumulated precipitation (normalized data): a clear inverse correlation between these data is observed. E12 is also shown but this trend has no correlation at all with precipitation data.

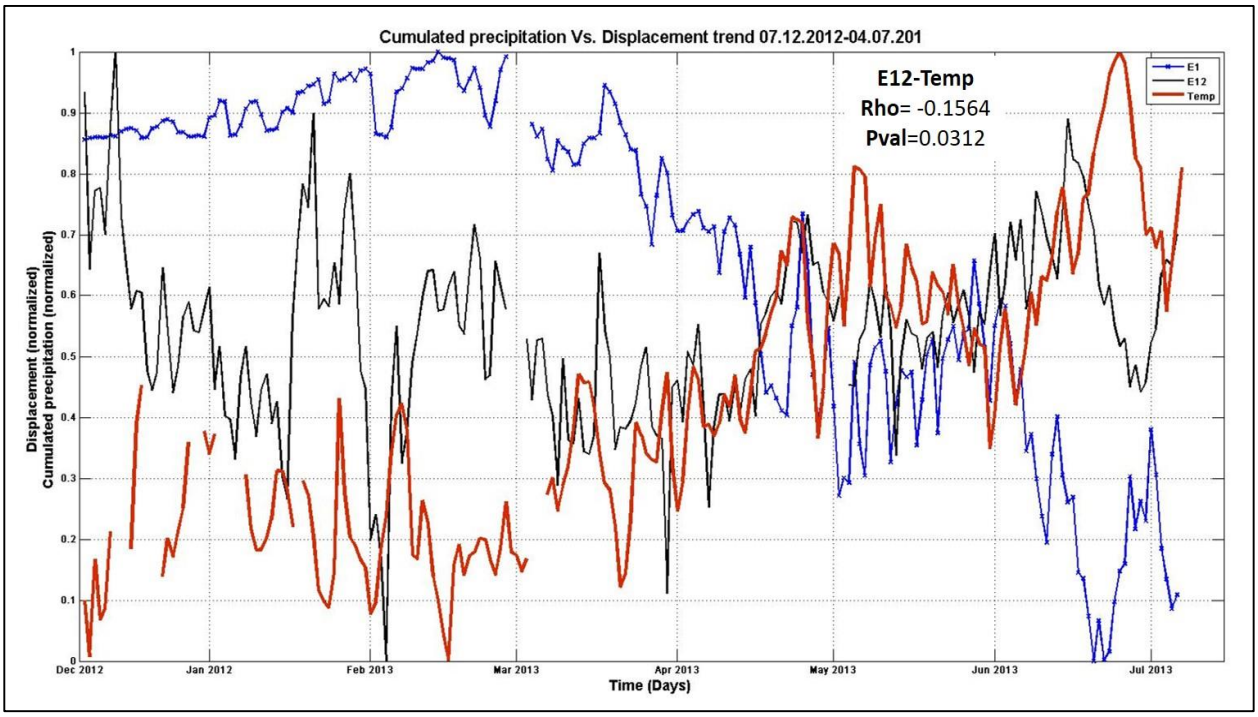

Figure 68 – Comparison between the anomalous displacement recorded by the extensometers E12 (central section of the main fracture in the upper part of the quarry) and temperature variation (normalized data): no correspondence with the available independent data is observed.

Table VII displays the **Rho** and **Pval** values for comparison between

- TOR4 HVSR amplitude trend Vs. temperature variation (Figure 69);
- TOR4 HVSR amplitude trend and velocity variation (dV/V) by Coda Wave Interferometry of NCFs (Figure 70).

Correlation test	Rho	Pval
Amp_HVSR_TOR4 – Temp	0.7147	$9.3923\ e^{-30}$
Amp_HVSR_TOR4 – dV/V_TOR1-TOR4	0.1650	0.0222

Table VII – Correlation and hypothesis of no correlation values obtained for comparison line 1: temperature variation Vs. HVSR amplification value at TOR; line 2: percentage of velocity variation for the station pair TOR1-TOR4 (2-10 Hz) Vs. HVSR amplification value at TOR4.

Excellent match is obtained by comparing the TOR4 HVSR amplification value and temperature variation (Figure 69) which in fact could cause the water content variation of the

propagation medium and consequently the relative V_S, first responsible for the change in the HVSR amplification value.

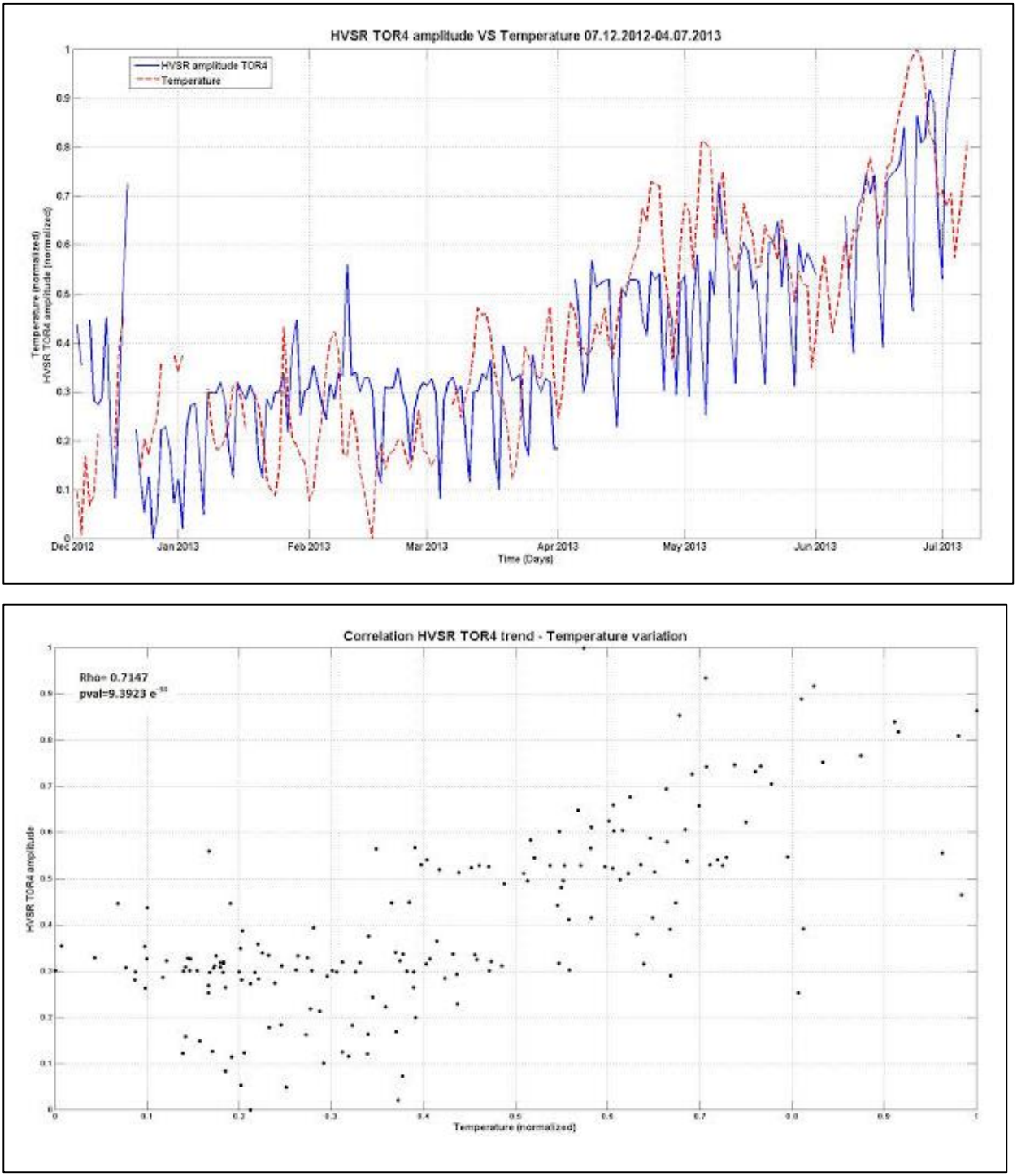

Figure 69 – Correlation between daily temperature variation and TOR4 HVSR amplification value: the trend is very similar for both the chosen parameters.

As already mentioned in the previous chapter, no significant degree of correlation results from the comparison between metereological, extensimetric or HVSR amplitude trend and the dV/V variation retrieved by NCF analysis (Figure 70).

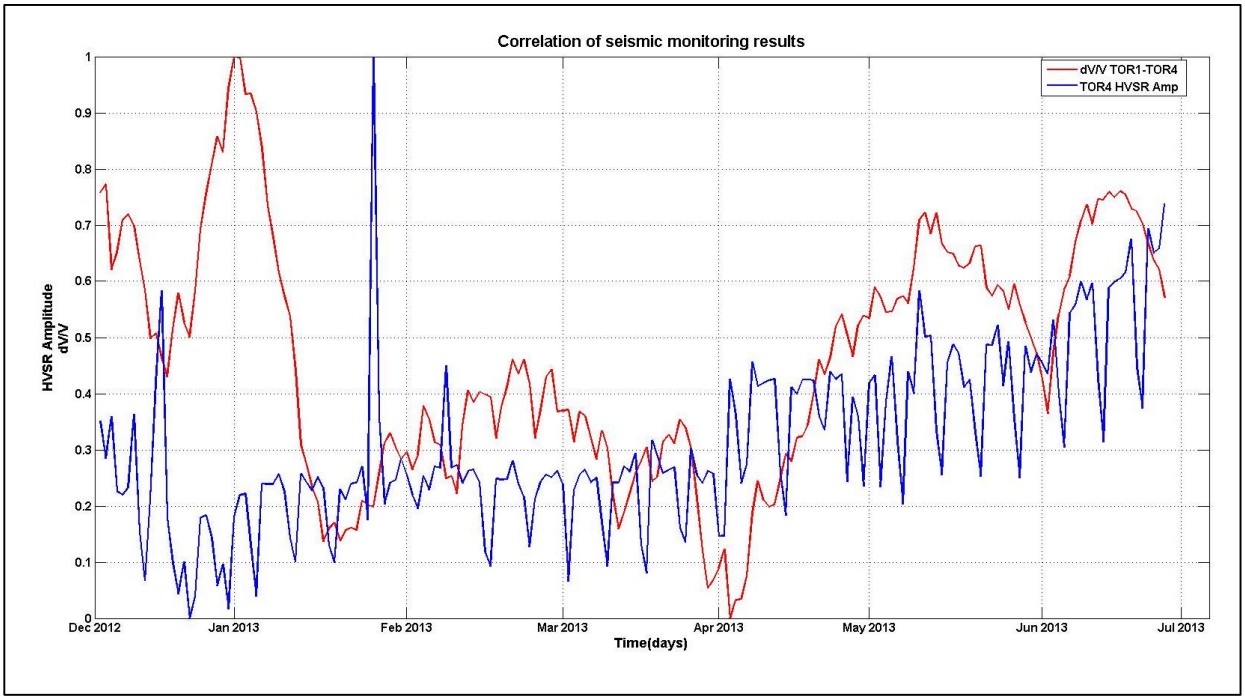

Figure 70 – Correlation between TOR4 HVSR amplification value and the most similar velocity variation trend obtained by Coda Wave Interferometry of NCFs for the station pair 'TOR1-TOR4' (2-10 Hz).

4.3 Semi-automatic detection of local fractures/cracks/collapses

4.3.1 STA/LTA: a first discrimination throughout the entire data set

Because of a huge amount of events occurred at the site since the installation of the seismic network, a semi-automatic procedure was applied to the continuous data streams in order to detect transient signals. This procedure is based on the STA/LTA algorithm applied to the vertical component of all the stations. The ratio between the average of the two sliding windows is evaluated in the frequency range 2.5-100 Hz. The first step of the analysis consisted in the search of the STA and LTA window lengths; the overlap of the windows (WS) was kept fixed to 50% of their respective length. I thus proceeded testing different window lengths, and then comparing manual and automatic results.

The trigger shows a good recognition capability for earthquakes that are recognized whatever is the length of the windows (Figure 71).

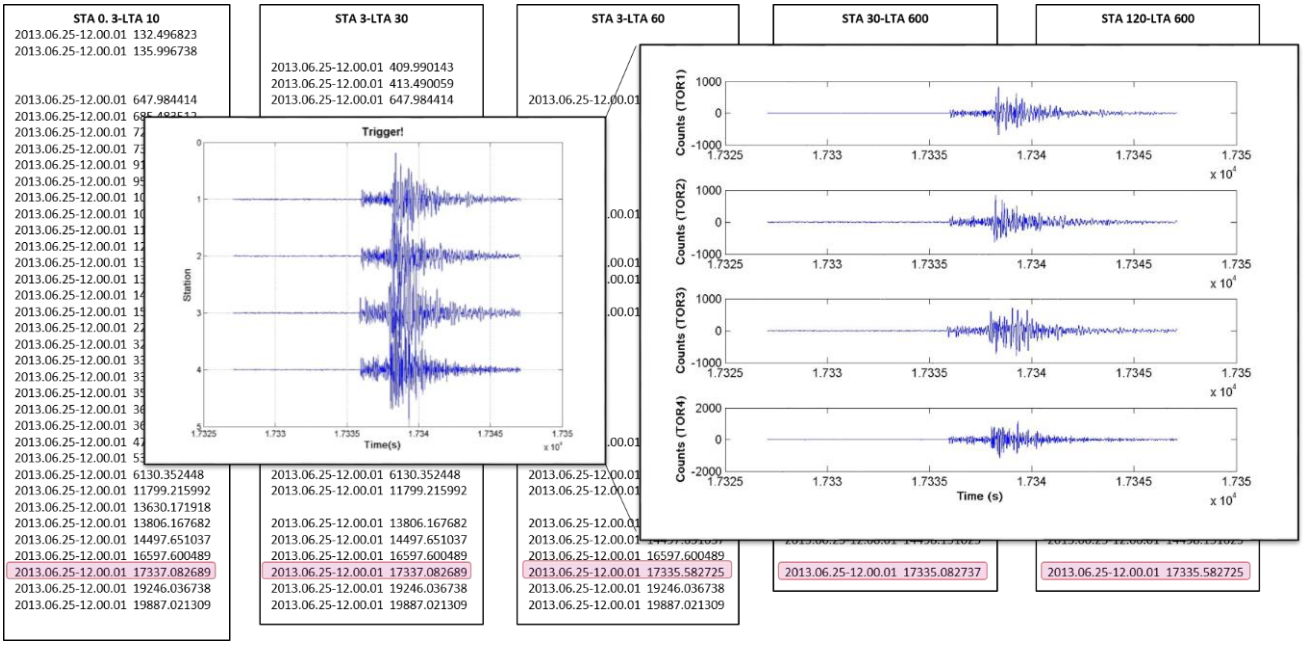

Figure 71 – Detection of an earthquake (EQ) event using different STA and LTA windows length. Each column correspond to the 6-hr event list generated by the code for the relative window length (reported at the top of the column); red rectangle highlight the visualized event.

The shorter events and those characterized by an instantaneous release of energy, such as rockfall and microcrack require the use of a shorter STA window (Figure 72).

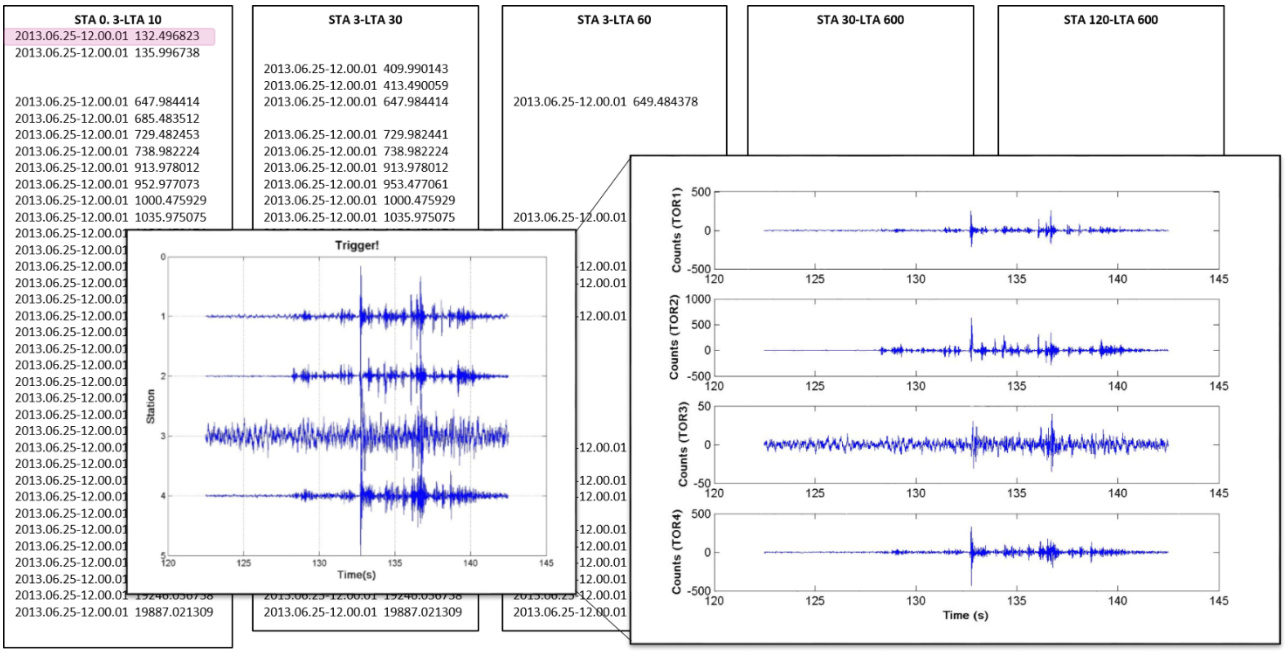

Figure 72 – Detection of a rockfall (RF) event using different STA and LTA windows length. Each column correspond to the 6-hr event list generated by the code for the relative window length (reported at the top of the column); red rectangle highlight the visualized event.

The best results were obtained using an STA length of 0.5 sec (WS=0.25 sec), an LTA length of 30 sec (WS=15 sec) and a threshold ratio fixed to 3, which means that the amplitude of the seismic signal must be at least three time greater than the noise to define a seismic signal. Every time that the threshold is exceeded a trigger is declared.

The analysis was carried out over 6-hour-long recordings from each station. An event is declared when a trigger is detected by at least three of the four acquisition point with a maximum delay of 1 sec; when this condition is met, the code chronologically list it, with its time reference and date, in a text file (Figure 73) so that in the end a text catalogue of events is available.

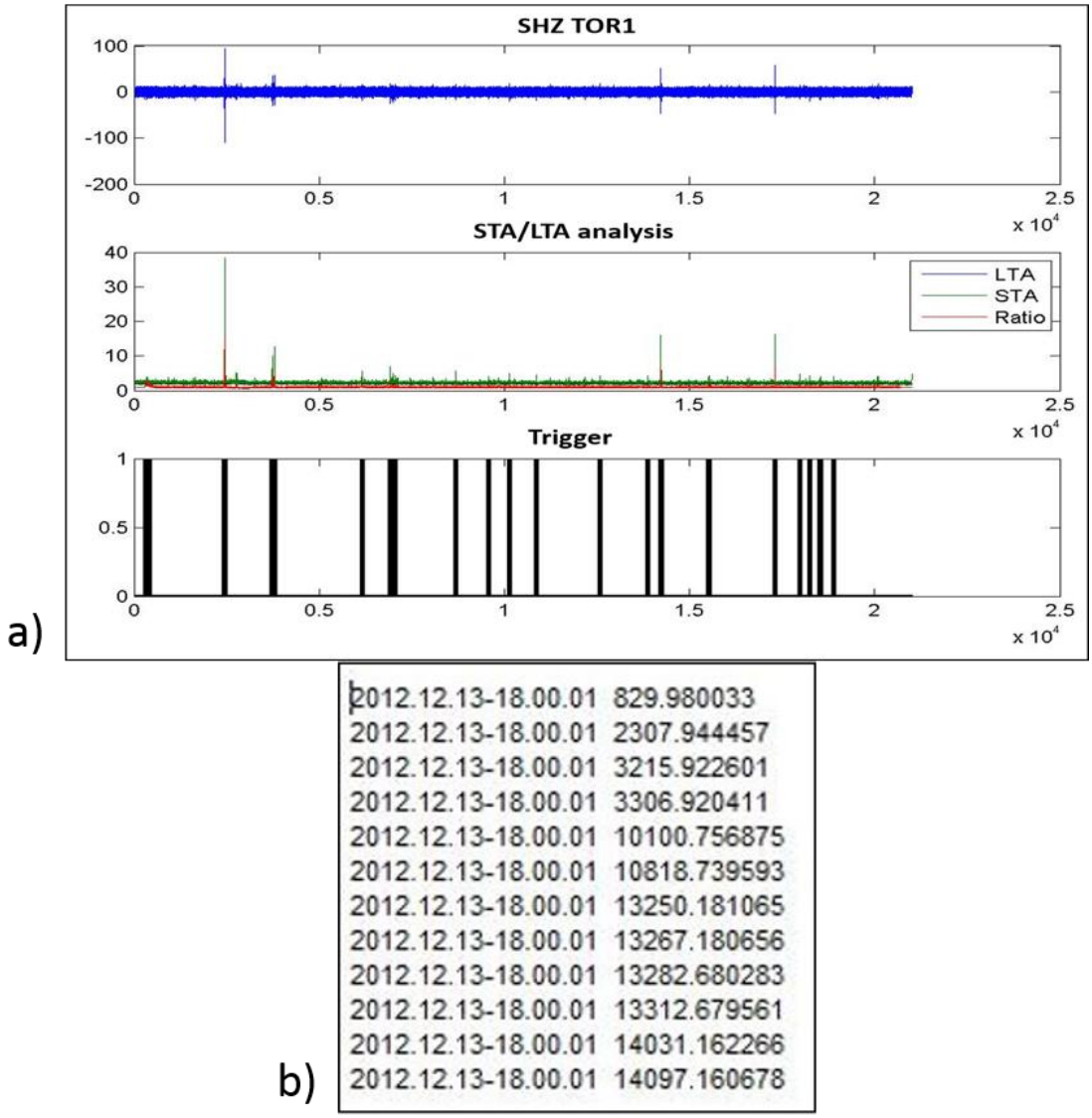

Figure 73 – STA/LTA analysis results: a) Top - 6-hr recorded SHZ component; Middle - STA/LTA ratio: values observed for each time window; Bottom – events characterized by an STA/LTA ratio higher than 3. b) Chronological list of detected events for each 6-hr file.

During the recording period the total number of events was 22785 with mean value of 28 events per 6-hour-long interval. The total trigger number has been integrated on a daily basis to have a first overview of the seismic activity rate at the acquisition site during the monitoring period and then the trend was compared to the rainfall and temperature variation (Figure 74): no correspondence is highlighted by these comparisons. The distribution is quite homogeneous with small anomalies observed on 8th March (301 events recorded in one day), on 9th and 29th April (respectively 409 and 305 events) and on 8th May (332 events). It is possible that these events were associated with small detachments of blocks or to the opening of small cracks in the medium but no evidence was observed at the research site so that I can not exclude an anthropic origin for these signals.

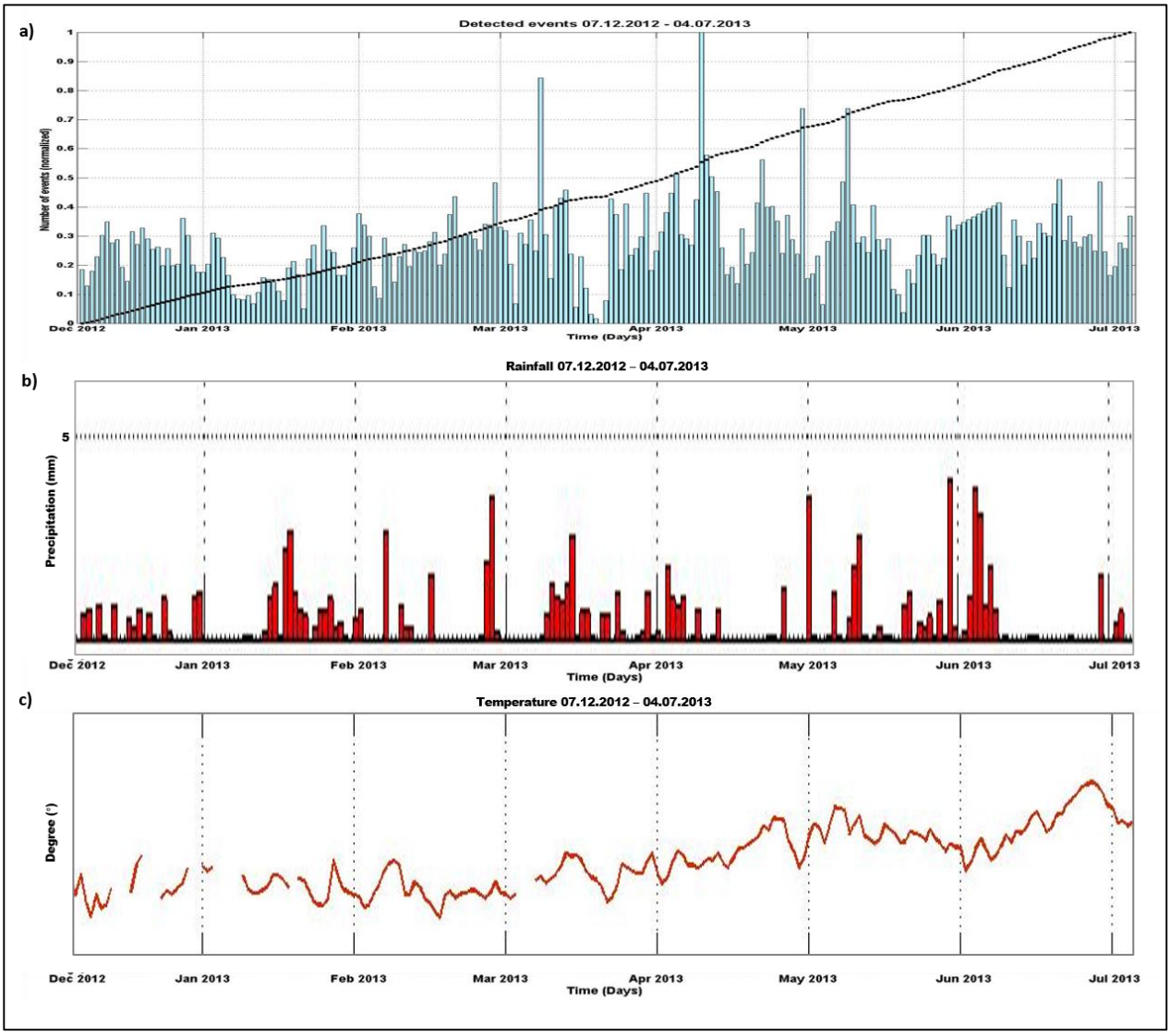

Figure 74 – a) Number of seismic events per day recorded during 7 months of the monitored period and cumulative curve; b) Rainfall trend (mm/day) for the monitored period; c) temperature variation in the same range of time.

Although the chosen method has proved to be rather accurate for events detection, the comparison with manual detection point out some key issues that have to be taken into account:

- many microseismic events, probably associated with microcraks or small relative movements of the rock blocks are discarded because were triggered by only one or two stations (Figure 75) even if the distance between them is very small (on the other hand, the condition of multiple stations detection automatically removes a huge number of signals due to local disturbances or electronic problems);

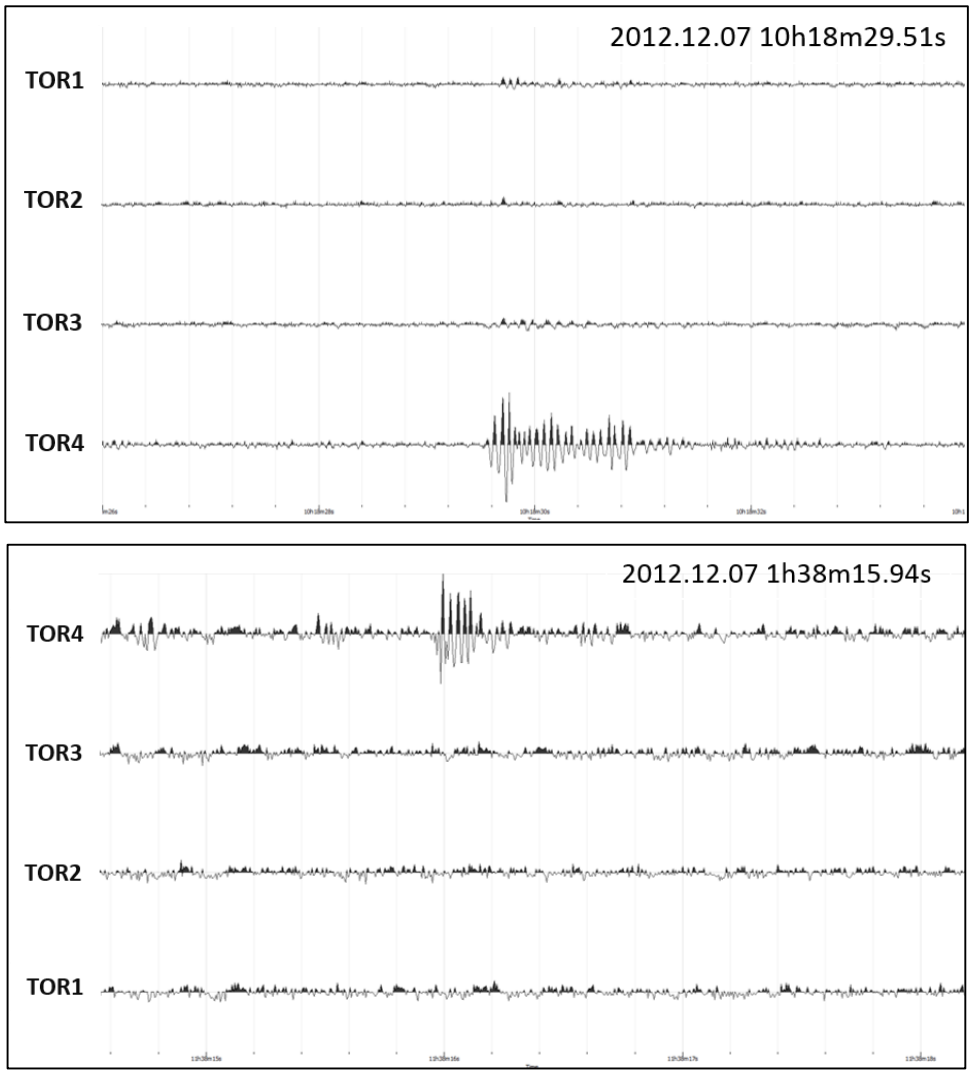

Figure 75 – Examples of two microseismic events recorded the 07.12.2012 (vertical scale in counts and horizontal scale in seconds). These seismic signals are detected by one only sensor (sensor TOR4 at the examples).

- the selected STA length, chosen to be sensitive to very short and small events, leads to a large number of false trigger due to rockfall event. This type of signals are characterized by many spikes, thus, they may be divided into several events corresponding to successive rock impacts on the ground (Figure 76).

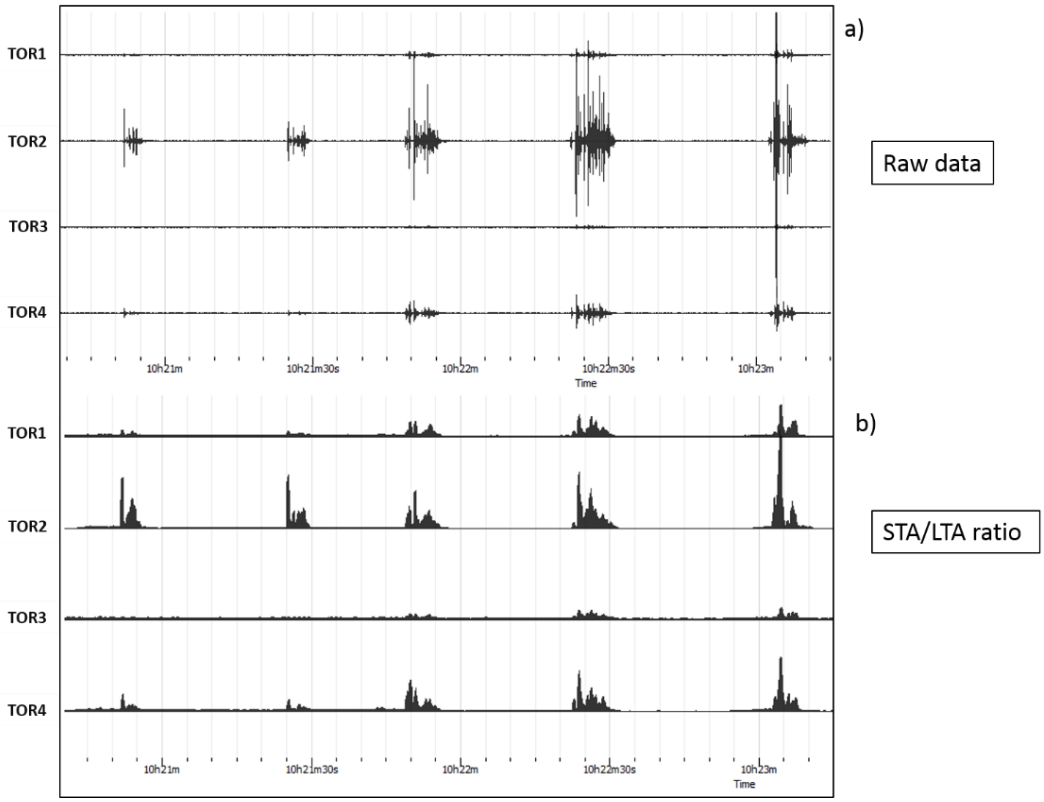

Figure 76 – a) Example of a rock fall event recorded the 25.06.2013 during an experimental test of manual rocks throwing (vertical scale in counts and horizontal scale in seconds); b) STA/LTA ratio results for the visualized section: the threshold is exceeded multiple time for each rockfall event at least at three stations.

4.3.2 Classification of different waveforms associated with some representative events detected using STA/LTA ratio

The last section of this chapter is devoted to classify all the listed events in four main categories:

- Local and regional earthquakes (EQ)
- Microquakes (MQ)
- Rock-falls (RF)
- Noise (N - helicopters, storms, anthropic activity, cars, etc.).

I first attempt to classify the recorded events using different amplitude thresholds, regardless their duration or frequency content but it is easy to see that there are infinite combination of signals with different origin that show the same amplitude at the recording site. Since the signal amplitude at the acquisition point is a function of both the amplitude at source and the epicentral distance, the classification based exclusively on this feature lead to big mistakes: for example, signals originated by a major distant earthquake can be easily exchanged with those related with a small local microquake or microcrack and conversely.

Thus, individual seismic signals has been visually checked individually and classified in the corresponding group. Figure 77 shows a selection of eight signals belonging to three different event types (a.): earthquake, b.): microcrack and c.): rockfall).
Data have not been corrected for the instrument response so signal amplitude is expressed in counts (see peak amplitude of each plot). The first examples are earthquakes (77a-77b), seismic signals of Figure 77c-77e are local microearthquakes while the last three signals are associated with rockfall events (77f-77g natural; 77h man-made during an experimental test of rock throwing).

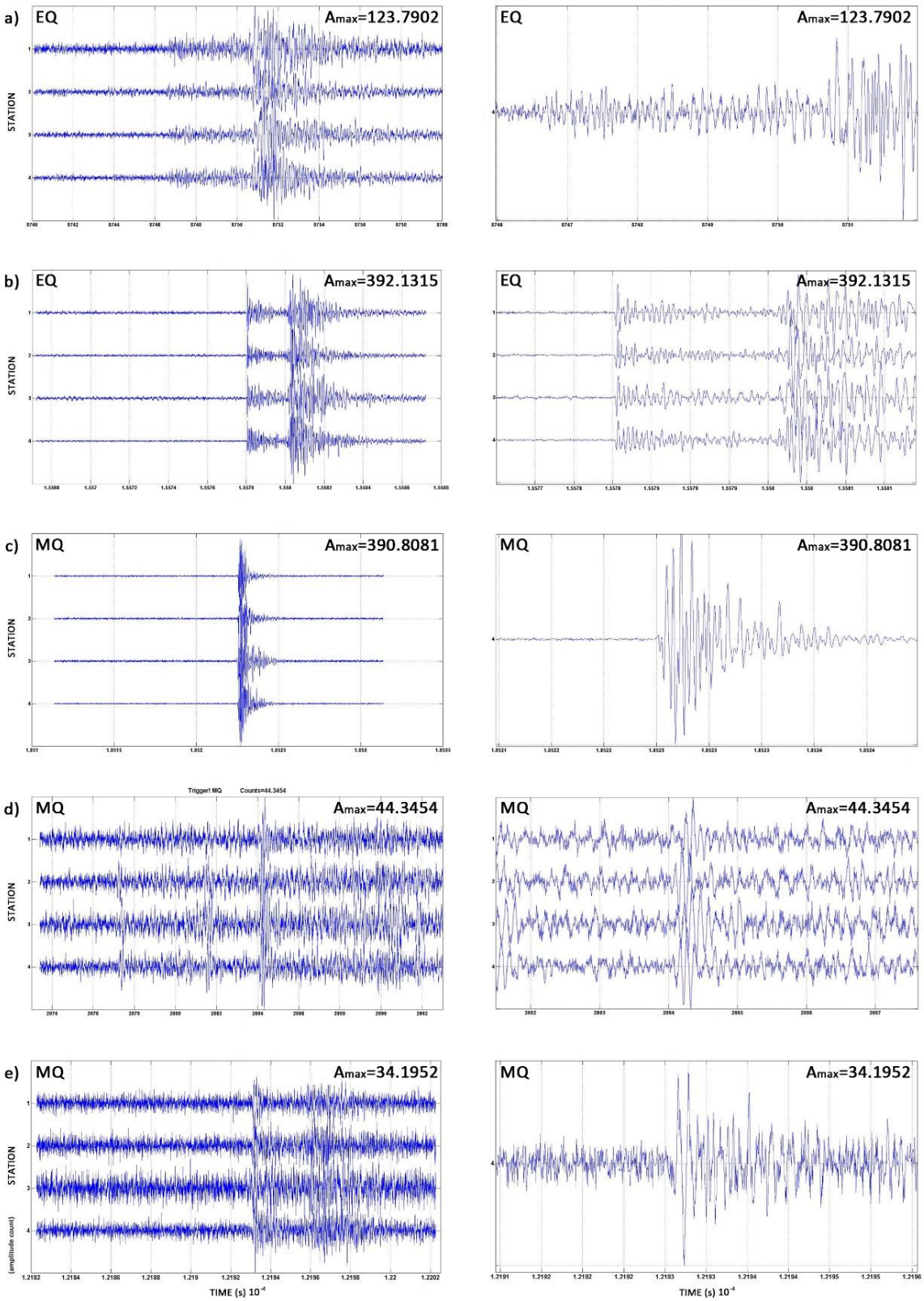
a)
EQ
Amax=123.7902
STATION
EQ
Amax=123.7902
b)
EQ
Amax=392.1315
STATION
EQ
Amax=392.1315
c)
MQ
Amax=390.8081
STATION
MQ
Amax=390.8081
Trigger! MQ Counts=44.3454
d)
MQ
Amax=44.3454
STATION
MQ
Amax=44.3454
e)
MQ
Amax=34.1952
STATION
(amplitude count)
TIME (s) 10-4
MQ
Amax=34.1952
TIME (s) 10-4

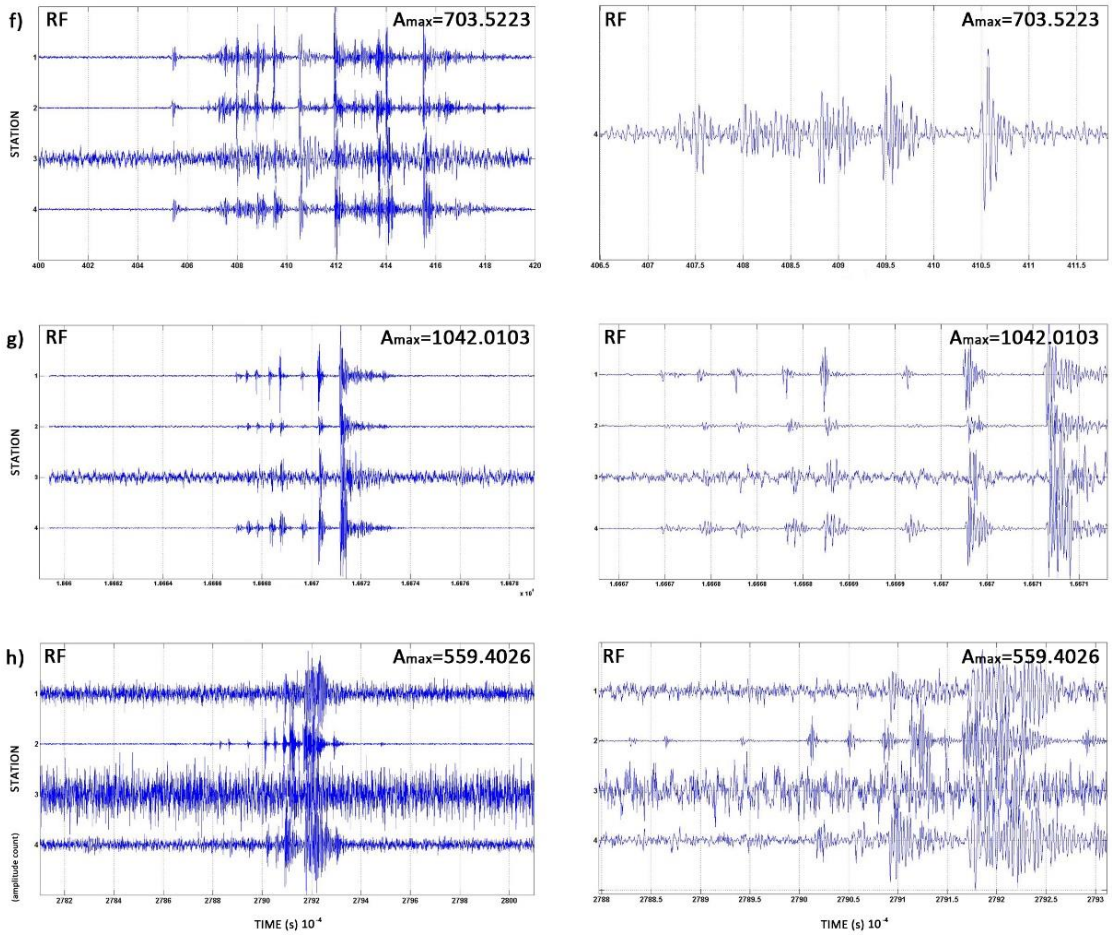

Figure 77 – (a-h) A selection of different types of signals. Left: Seismogram recorded for SHZ component of the four station; Right: zoom for a window of 5 s around the peak of amplitude. The maximum amplitude (in counts) is given at the top of each plot together with the corresponding category.

Large part of the recorded events consists of earthquakes, both regional and local but rockfalls are also frequently detected.

The experimental test carried on June 25, 2013 as part of another thesis project allowed the calibration of our network. Some small instable rocks were collected and thrown from the middle section of the quarry, since the upper part is covered by vegetation and is improbable that rocks fall down from there. In terms of amplitude the peaks range from 479,3408 counts to 7123,7445 counts with one only exception of amplitude of 355,1901 counts. Assuming an amplitude threshold of 400 counts almost all the rockfall events are properly classified. However, for the aforementioned reasons, a subsequent manual check is necessary to reclassify some events related with microcracks or local earthquakes improperly classified in this category. Due to the lack of major seismogenetic sources in the neighbourhood of the

test site the events characterized by an amplitude similar or higher to that of the rockfalls are very few.

A different procedure was adopted to automatically discriminate microcracks and microquakes.
An event list for the microcrack classification procedure was manually selected in order to identify the majority of event shapes.
The manual selection of the microearthquakes events allowed the recognition of different waveform families (Figure 78 shows the two type of waveforms more frequently observed: family 1 on the left-hand panel and family 2 on the right-hand panel). Each waveform type could be related to the activation of different system of fractures or to different phase of cracking mechanism (opening of existing fractures, initial phase of fracturation, growing or coalesce of existing micro-fractures into larger fractures, etc).

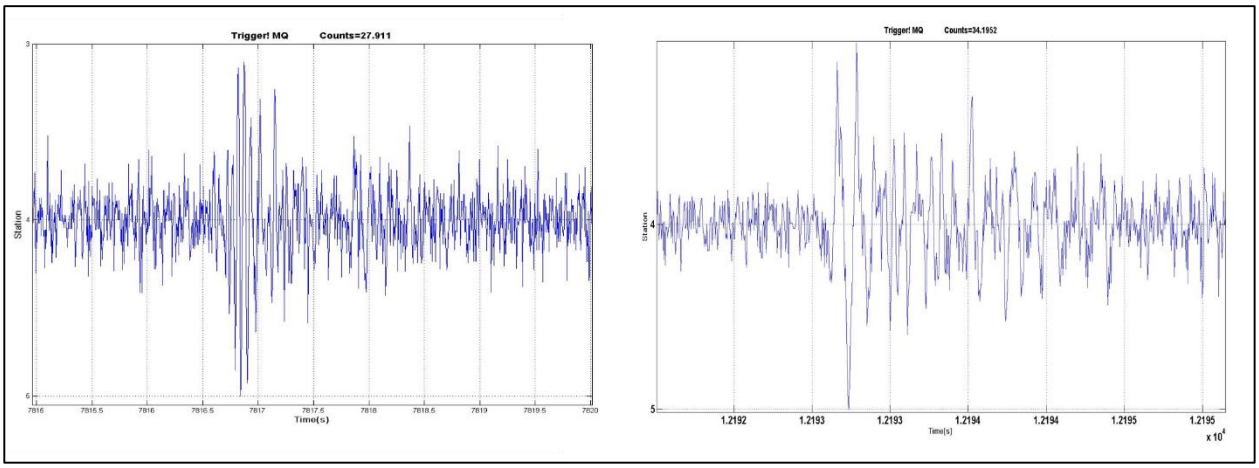

Figure 78 – Example of multiplet waveforms recorded at the station TOR4. Left: waveforms of the family 1; right: waveforms of the family 2. Horizontal scale in seconds. Vertical scale in counts.

After isolating some template wavelets (manually selected from those discriminated by the STA/LTA trigger) and assuming those as representative for the b) group I proceed using a Matlab code that tests each wavelet sliding it by half of its length over each 6-hour-long trace recorded at the corresponding station and evaluating the cross-correlation at each time lag in order to recognize other similar waveforms through the trace. For the cross-correlation, an empirically selected window length of 6 s was chosen. It is noted that the correlation function only measures the relative similarity of the waveform shape and not the amplitude of the events, thus giving a measure of the path which the seismic energy takes, not the magnitude of the trigger. Both the trace and the sample wavelet were filtered with a zero-phase band-

pass Butterworth two-pole filter. A low-frequeny cutoff of 20 Hz and a high-frequency cutoff of 100 Hz were initially selected. To test that the classification is robust, regardless of the low-filter characteristics, the procedure was conducted with a series of cutoff levels ranging between 2.5 and 20 Hz: this produced no significant changes in the results obtained confirming that the majority of the signal power is concentrated between 20 and 100 Hz for this type of event. The code selects all the events similar to the template wavelet considering significant the peak of cross-correlation coefficient when it exceed a certain threshold correlation coefficient value (ψ) and writes down a text file which reports starting and ending time of the similar event, with the condition that, to be scheduled, an event must be separated by the preceding one by at least 1 second. An additional problem is the choice of ψ that have to be chosen in order to extract events within the selected waveform (similar to that of the sample wavelet) from the entire trace. If ψ is too low, waveforms which have slightly different structure can be considered as similar to the first one, if ψ is too high, many events not being recognized at all. I tried to apply various threshold value, ranging from 0.60 to 0.80 obtaining very different results: from no or few correspondences (ψ=0.80) to a huge number of false matching events (ψ=0.60). Figure 79 shows the results obtained for 6-hour-long trace at TOR1 using a selected wavelet for different threshold (a.): ψ=0.60; b.): ψ=0.70; c.): ψ=0.80). Each red dot signals a discriminated event.

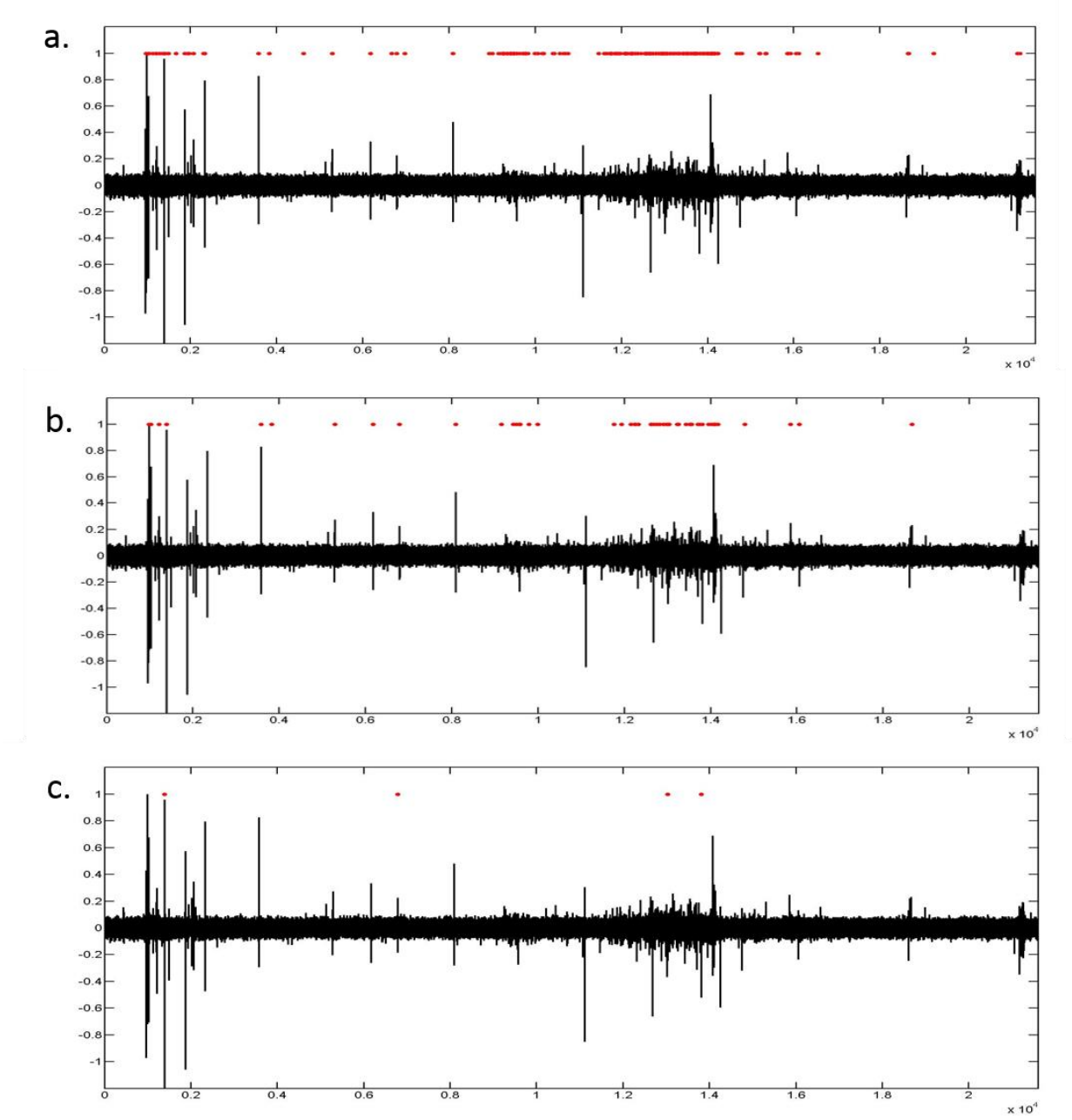

Figure 79 – Application of the automatic code for the microcrack discrimination over a 6-hour-long trace, station TOR1, using the same sample waveform and different threshold value (a.): ψ=0.60; b.): ψ=0.70; c.): ψ=0.80); red dots correspond to the events similar to the sample waveform Horizontal scale in seconds. Vertical scale in counts.

The threshold value of ψ=0.70 allows the detection of many events discriminated by the manual check but the majority are not yet correctly identified by the use of any of the more frequently chosen waveforms even if the code found some false matches of the wavelet with events not related to this group of signals. With the above consideration taken into account, a lower threshold value is definitely not recommended.

The results obtained from the application of the automatic code suggests that the great variability in the observed waveform types and the chosen sampling frequency (200 Hz), that caused a lack of information in the recording of these signals that generally exhibit the greatest amount of energy also at frequencies above 100 Hz, not allowed to determine one or more reference wavelet able to automatically discriminate the overall of the microcrack events occurred during the monitoring period.

Therefore, automatic discrimination of such events is not possible within this code even providing more sample wavelets; nonetheless, the choice of a number of representative waveforms, requires long-times and results in unsatisfactory advantages respect to manual discrimination. Further analysis on the frequency content or on the event duration are recommended to define other parameters more fast and practical for improving the automatic classification but this part is beyond the scope of this work.

CHAPTER 5 – DISCUSSION AND CONCLUSIONS

5.1 Results interpretation and final conclusions

Landslides are complex phenomena whose study necessarily requires a multidisciplinary approach based on a wide range of observations including geological and geomorphological mapping, geotechnical and geophysical investigations, geodetic surveys, satellite observations and meteorological data analysis. The integration of different techniques should allow us to obtain useful information for all the phases of the landslide disaster cycle, overcoming drawbacks and imitations of each single method applied individually.

In complement to other techniques, passive seismic monitoring can be used as a non-invasive and low-cost investigation tool easily applicable to very diverse geological context in turn allowing for monitoring the progressive damage and deformation of unstable slopes besides the classical prospecting applications.

This work presents the results from a small-scale seismic network which was deployed at the Torgiovannetto quarry (Central Apennines, Italy) from December 2012 to July 2013, in order to evaluate the possibility of improving the early-warning monitoring system of a rockslide by means of seismic observations. Four seismometers, acquiring data in continuous mode, were set up inside and at the edge of the quarry, with an average spacing of about 100 m. The entire data set (7 months of continuous recording) was analysed through various procedures: HVSR (Horizontal to Vertical Spectral Ratio) and HVSR directivity were adopted for investigating the local seismic response; Coda Wave Interferometry of the NCFs (Noise Correlation Function) was used to detect possible changes in the seismic velocity within the unstable rock mass; STA/LTA (short-time-average/long-time-average) trigger was applied to detect the occurrence of transient signals.

As for the background seismic noise its overall amplitude trend does not show any major variation during the recording period; daily and weekly fluctuations of the signals reveal the dominant role of the anthropogenic and meteorological effects.

With respect to the HVSR curves, the different shapes observed at the four stations agree well with the structural model of the investigated area retrieved by previous morphotectonic investigation and geological field survey that identified a portion of fractured *Maiolica* limestones overlying the compact rock. The HVSR technique shows resonance peaks related to an impedance contrast that could be referred to the interface between the fractured

superficial layer and the underlying compact rock. This feature is observed at least three of the four stations (TOR1, TOR3 and TOR4), implying that the fractured area extends beyond the limits of the unstable wedge as detected by traditional monitoring techniques. With respect to the HVSR peak frequencies and amplitudes, the 2D impedance contrast map obtained through the passive seismic prospection is consistent with the available geophysical investigation confirming a complex structural and stratigraphic asset of the slope. These results proves that, performing a sufficient number of measurements, evenly distributed on the landslide body, the HVSR single station acquisition, fast, cheap and non –invasive technique, is a robust method for a first approximation of the rockslide seismo-stratigraphic characterization. Thus, the HVSR can be used to: (1) locate the sliding surface; (2) estimate the thickness of the landslide body and (3) characterize the geometry of the landslide.

Moreover, the temporal change of the HVSR and its peak value observed at station TOR4 provides information on the temporal variation of the acoustic characteristics of the medium, suggesting the constant increase of the impedance contrast (velocity and/or density variation) between the unstable mass and the underlying solid bedrock.

The HVSR shape at TOR3 and TOR4 show a sharp resemblance probably due to a similar seismo-stratigraphic asset at the two acquisition points. However, the temporal trend of HVSR peak amplitude at the two sites is substantially different: almost stable at TOR3, increasing at TOR4. The first hypothesis for the explanation of that result is based on the water content variation in the superficial layer, whose effects rapidly vanishes at TOR3, causing temporary shift of the main frequency, and a seasonal change in the same parameter at TOR4. With varying water content in the pore, seismic velocities change from day to day and also from season to season but the main discordance for this hypothesis is the different trend observed at two stations so close in space. A relevant role could be played by a more complex and articulated fracture system that affect the sliding wedge on which is located TOR4 (secondary porosity well interconnected in the upper part of the slope and no outlet towards downstream) associated to its lower altitude that requires longer times for the conveyance of the precipitation water and the eventually return to the initial condition of saturation. By the way one can not exclude a permanent modification of the seismic velocity in the medium under TOR4 due to a long dwell time of the fluids in the surficial fractured zone. This extended increase of the pore pressure could result in changes of the medium properties to which seismic velocities and density (and, consequently the seismic impedance

contrast) tend to be sensitive (Oubaiche E.H. et al., 2012). Unfortunately, no data could be retrieved to support this thesis by the piezometers in the quarry because they have been destroyed from previous collapses but further information come out from the traditional surveillance network.

The comparison of the rockslide displacements, (as monitored by the extensometric network) and the precipitation trend shows a good correlation while no match can be found with the seismic data retrieved by continuous monitoring of the HVSR. Thus, assuming that the water content variation is mainly responsible for the H/V amplitude changes one could explain this fact in two different ways:

- the current water content in the subsoil does not reflect the temporal trend of precipitations;
- the medium properties modifications, due to changes in the pore pressure, require variable time to occur and, in some cases, they could not occur at all.

Unfortunately, the lack of evidence of surface displacements corresponding to the observed variations in the HVSR amplitude trend foreclosed any possibility of threshold identification that could be used as an early warning system. It could be interesting to evaluate this technique as a surveillance method when it can be calibrated on monitoring intervals characterized by a high rate of surface activity.

On the other hand, in order to justify the strong resemblance that emerges by comparing the temperature trend and that of the H/V recorded at TOR4 one could suppose a direct dependency of this latter parameter on the meteorological conditions, as for instance suggested in Albarello (2006) that ascribes a fundamental role to barometric conditions variation concerning the composition of the noise wavefield (Tanimoto et al., 2006). Lee et al. (2014) observed a similar situation at very high latitude but in that case the variations could be explained by the cycles of freezing and thawing that crumble the surface rocks changing their acoustic properties. If this were the case, an extended dataset (> 1 yr) would be necessary in order to clarify whether the observed variation at TOR4 are part of cyclical phenomenon occurring over longer periods, as a consequence of seasonal changes. Unfortunately, the harsh acquisition conditions prevented from extending the experiment over longer time intervals. In my opinion, the hypothesis that the HVSR amplitude value is directly related to metereological factors can be excluded. If this were the case, all the stations, given their small spacing, should have exhibited the same amplitude increase.

Mavko (1992) points out that strong changes in the value of temperature directly affect the propagation velocity of the medium modifying the compressibility and/or the viscosity of the fluid trapped in it especially when the rocks contain liquid hydrocarbon but in my case (with no evidence of oil trapped in the rocks and a maximum variation of 25°C), temperature variation could contribute in a more meaningful way through other mechanisms:

- provoking an higher fracturing degree of the medium acting directly on the dilatancy of the rocks. An increase in the fracturing of the medium in turn may result, directly or, more often, indirectly, in density or velocity of propagation variations;
- influencing the water content of the superficial layer toward drier conditions, thus leading to an increase of the propagation velocity of this portion of the slope. This hypothesis is supported by the fact that the variation in the impedance contrast occurs with the approach of the hot season and higher temperature (early April, 2013).

In the case of Torgiovannetto seismic network the different trends observed at TOR3 and TOR4 could be due to the different vegetation cover surrounding the stations: the first is placed in the wooded area upstream of the quarry while the second is on bare rock and, therefore, more susceptible to be influenced by temperature variations.

It is worth noting that is impossible to unequivocally identify the reason for such amplitude variations using only the seismic data because there are many factors that could cause velocity or density variation (as examples: (1) opening of new or pre-existing fractures, cracks and flaws; (2) rocks diagenesis or its inhibition and/or (3) variation in the percentage of saturation) that could be generated by many phenomena that can not be directly detected by the sole analysis of seismic traces.

The HVSR directivity, that shows an overall stationarity throughout the monitoring period, has the same orientation regardless of source position and type: this result proves the existence of a marked anisotropy of the medium due to the presence of an oriented fractures system that strongly affect the seismic wavefield especially at sites TOR1 and TOR4. The resulting polarization angles are parallel to the main fractures system as derived from previous field surveys and clearly recognizable at the surface thanks to the outcropping of the main fracture. This demonstrates the robustness of the passive seismic technique as a tool to identify and characterise the main pattern of the fracture field.

The Coda Wave Interferometry of the NCFs provides information about possible velocity variations of the medium between each station pair throughout the entire recording period but the results seem to be strongly dependent on the choice of the input parameters.
None of the examined pairs of stations shows a significant correlation between the trend of velocity changes and that obtained from the traditional monitoring network (extensimetric and meteorological stations) or the one derived from the HVSR analysis. I tried several different input parameters expecting a positive match in at least the analysis of the cross-correlation function between the station pair whose joining line crosses TOR4 (TOR1-TOR3) but there is no trace of the variation recorded at this station. The best match is obtained for the TOR1-TOR4 pair in two cases: (1) using a very short moving window (0.1 s) and, (2) using a 2-10 Hz frequency band. In both these cases the data analysis reveals a different trend for the first period of the acquisition but the velocity increases on early April, 2013, and on early June, 2013 lasting to the end of the monitoring period are consistent with the upward trend observed in the HVSR amplitude at TOR4.
Two main things should be taken into account once interpreting results from the coda-wave interferometry together with those from the H/V spectral analysis. This last procedure provides punctual information, related to the seismo-stratigraphic setting beneath the acquisition point. The Coda Wave Interferometry of the NCFs approach gives an estimate of the possible changes in the propagation velocity for a more extensive portion of the medium, that in this case includes one section of the unstable wedge (from TOR4 towards TOR1) and one part outside it (from TOR1 toward TOR4). The overall result could therefore mask very local variations and partially differs from the previous one because it results from the combinations of variations experienced by different portions of the medium.
Moreover, the seismic velocity variation may not be the only one to contribute to the change in seismic impedance of the surface layer as previously mentioned.

The detection of transient signals is based on the analysis of the continuous data streams recorded at the four sensors. I checked the efficiency of the semi-automatic STA/LTA detection using different combinations of window lengths and imposing the coincidence of the detection for at least three of the four stations. The software package *Geopsy* was used to compare the visual recognition of the events and the semi-automatic detection. The method has proved to be an efficient way to detect all the type of events that occurred within the monitoring period and a time-saving solution. After visual inspection of all the detected events, the signals were grouped into four main categories of events: (1) microcracks; (2)

rockfalls; (3) earthquakes and (4) noise. Microcracks and rockfalls ('local events') are due to the dynamics of the rockslide by itself while the other two groups are not directly related to it.

Since the earthquakes are located at least several kilometres away from the array, their recognition is quite easy. In fact this type of signal shows distinct P- and S- waves and no significant variations of amplitude among all sensors.

On the contrary the 'local events' show strong variations of amplitude values at the four sensors due to the proximity of the source.

For the classification of rockfalls I used a criteria based on: (1) duration; (2) amplitude: (3) and concentration of peaks due to the subsequent impacts of the boulder on the slope during the free fall. Moreover, since the ability of rockfalls to produce seismic signals is expected to be greater in the lower section of the quarry, which is completely free from vegetation, one can expect a higher amplitude at stations TOR1, TOR2 and TOR4. A great help came from the comparison of the selected event with those generated during a stone-throwing test conducted within the monitoring period for another research project. The amplitude threshold of 400 for the STA/LTA trigger seems to be a good discriminant at least for events generated by blocks with relevant dimension.

I also attempted an automatic discrimination of the microcracks events through a cross-correlation procedure. Some types of waveforms ascribable to this category are selected on these bases: (1) short duration (from fractions of a second to two seconds); (2)and no distinction between P- and S-waves arrival times due to the short distance between the source and the sensors.

Thus, I selected some sampling wavelets to use as a template for the cross-correlation procedure through the entire dataset in order to develop an automatic technique for the discrimination of this type of event. Unfortunately, the procedure has not provided the expected results probably because of the great variability of the waveforms attributable to such events.

A further limitation to the automatic classification could also result from the choice (dictated by the need to proceed with a continuous acquisition) of a low sampling frequency (200Hz). This involved the loss of information above 100 Hz that could have lead to a significant improvement in the discrimination ability of the adopted technique.

In conclusion, it is reasonable to hypothesize that for an efficient seismic monitoring of an unstable area such as the one presented in this work, the best solution would be the use of

two distinct seismic networks: the first, similar to Torgiovanetto one, dedicated to the continuous acquisition and monitoring of the general characteristics of the landslide body and its elastic properties through techniques such as HVSR and NCF. The second, operating in trigger mode with a higher sampling frequency, was dedicated to providing information on high frequencies of the signals and strictly dedicated to the transient analysis.

Furthermore, some key considerations can be inferred starting from the results:

(1) the passive seismic technique is definitely an effective, cheap and relatively quick tool for the stratigraphic characterization of an unstable body;

(2) regarding the surveillance purpose, the variations highlighted through HVSR and NCF technique would need: (a) longer acquisition times, and (b) a comparison with many other parameters to be modelled and interpreted quantitatively;

(3) the real-time monitoring of rock falls and microcracks is very challenging in terms of the technological approach, and also extremely site-dependant because it requires the characterization of the waveforms ascribable to the various phenomena. Furthermore, the same type of event can cause very different waveforms (e.g., rock falls in different portions of the landslide that result in traces composed by several differently spaced seismic impulses).

Nonetheless, the rapid technological advances that allow increasing speed in acquisition, transmission and processing of data suggest that it is definitely worth proceeding with the seismic monitoring of unstable slopes.

AKNOWLEDGEMENT

These are the people and institutions that for different reasons having to do with this dissertation as well as with myself and that I would like to thank.
Special thanks go to my supervisors, Prof. Nicola Casagli, Prof. Sandro Moretti and Gilberto Saccorotti for the opportunity to undertake this research and for their thoughtful guidance throughout. Gilberto, I really appreciate your help and the multiple email exchange as well as the revision and corrections that drove me in this adventure!

I would like to thank all my friends and colleagues at DST – *Dipartimento di Scienze della Terra*, from UNIFI – *Università degli Studi di Firenze*, for always being present when I needed help.

I gratefully acknowledge the support and the constant presence of Andrea Fiaschi and Luca Matassoni from FPR - *Fondazione Prato Ricerche* who welcomed me into their office and shared with me their knowledge as well as countless field trips.

Je voudrais aussi remercier Dr. Jean-Robert Grasso, pour le temps précieux qu'il a consacré à la lecture de cette thèse.
Merci aussi à Prof. Stephane Garambois et Christophe Voisin de l'ISTerre – Institut des Sciences de la Terre, de Grenoble pour les explications du fonctionnement du programme Geopsy et pour la guidance dans le labyrinthe du code de ce programme.

Lastly, my heartfelt thanks go to my partner Fabrizio Iuliani and my adorable baby Gregorio whose faithful support during the final stages of this Pd.D. is so appreciated. And most of all for my loving family, close relatives and friends who have always given me considerable support and encouragement.

REFERENCES

Adamczyk, A., Malinowski M. and Malehmir A. (2013) - Application of first arrival tomography to characterize a quick clay landslide site in Southwest Sweden: Acta Geophysica, 61, pp. 1057–1073, doi: 10.2478/s11600-013- 0136-y.

Adamczyk, A., Malinowski M., and Malehmir A. (2014) - High-resolution near-surface velocity model building using full-waveform inversion: A case study from southwest Sweden: Geophysical Journal International, doi: 10.1093/gji/ggu070.

Agnesi V., Camarda M., Conoscenti C., Di Maggio A., Diliberto I.S., Madonia P. and Rotigliano E. (2005) – A multidisciplinary approach to the evaluation of the mechanism that triggered the Cerda landslide (Sicily, Italy). Geomor., 65, pp. 101-116.

Aki K. (1957) – Space and time spectra of stationary stochastic waves, with special reference to microtremors. Bull. Earthq. Res. Inst., 35, pp. 415-456.

Akram J. and Eaton D. (2012) – Adaptive microseismic event detection and automatic time picking. Geoconvention 2012: Vision.

Al Yuncha Z. and Luzòn F. (2000) - On the horizontal-to-vertical spectral ratio in sedimentary basins. Bull. Seism. Soc. Am., 90, pp. 1101-1106.

Albarello D. (2006) – Possible effects of regional meteoclimatic conditions on HVSR. NATO SfP 980857 – II° Intermediate Meeting. Dubrovnik 25-27, November, 2006.

Albarello D. and, Lunedei E. (2013) – Combining horizontal ambient vibration components for H/V spectral ratio estimates. *Geophys. J. Int.*, 2013, 194, pp. 936-951.

Allen R. (1978) - Automatic earthquake recognition and timing from single traces. Bulletin of the Seismological Society of America, 68, pp. 1521-1532.

Alta Scuola (2005a) – Studio del fenomeno franoso interessante la cava di Torgiovannetto di Assisi (PG) - Relazione di prima fase.

Alta Scuola (2005b) – Studio del fenomeno franoso interessante la cava di Torgiovannetto di Assisi (PG) - Relazione di seconda fase.

Alta Scuola (2006a) – Studio del fenomeno franoso in essere in località Torgiovannetto di Assisi (PG) ed individuazione degli interventi volti alla riduzione del rischio idrogeologico – Relazione finale. Committente: Comunità Montana del Subasio.

Alta Scuola (2006b) – Studio del fenomeno franoso in essere in località Torgiovannetto di Assisi (PG) ed individuazione degli interventi volti alla riduzione del rischio idrogeologico – Integrazione alla relazione finale.

Amitrano D., Grasso J.R. and Senfaute G. (2005) – Seismic precursory patterns before a cliff collapse and critical point phenomena. Geophysical Research Letters, 32. DOI: 10.1029/2004GL022270.

Amitrano D., Gaffet S., Malet J.P and Maquire O. (2007) – Understanding mudslides through micro-seismic monitoring: the Super-Sauze (South-East French Alps) case study. *Bull. Soc. Geol. Fr.,* 2007, t. 178, n°2, pp. 149-157.

Amitrano D., Arattano M., Chiarle M., Mortara G., Occhiena C., Pirulli M. and Scavia C. (2010) – Microseismic activity analysis for the study of the rupture mechanisms in unstable rock masses. *Nat. Hazards Earth Syst. Sci.*, 10, pp. 831-841, 2010.

Antonello G., Casagli N., Farina P., Leva D., Nico G., Sieber A.J. and Tarchi, D. (2004) - Ground-based SAR interferometry for monitoring mass movements. Landslides, 1, pp. 21–28.

Arai H. and Tokimatsu K. (2004) – S-wave velocity profiling by inversion of microtremor H/V spectrum. Bull. Seism. Soc. Am., 94, pp. 53-63.

Arosio D., Longoni L., Papini M., Scaioni M., Zanzi L. and Alba M. (2009a) - Towards rockfall forecasting through observing deformations and listening to microseismic emissions. *Natural Hazards and Earth System Science, 9*, pp. 1119–1131.

Arosio D., Longoni L., Papini M. and Zanzi L. (2015) - Modern Technologies for Landslide Monitoring and Prediction. Springer Natural Hazards 2015, pp. 141-154.

Balducci M., Regni R., Buttiglia S., Piccioni R., Venanti L.D., Casagli N. and Gigli G. (2011) – Design and built of a ground reinforced embankment for the protection of a provincial road (Assisi, Italy) against rockslide. Proc. XXIV Conv. Naz. Geotecnica, AGI, Napoli, 22th-24th June 2011.

Bancroft J.C. (2009) - Sensitivity measurements for locating microseismic events, CREWES Research Report.

Baptie B.J. (2010) – Lava dome collapse detected using passive seismic interferometry. Geophysical research letters, Vol. 37, L00E10, doi: 10.1029/2010GL042489.

Barchi M., DeFeyter A., Magnani B., Minelli G., Pialli G. and Sotera B. (1998b) – The structural style of the Umbria-Marche fold and thrust belt. Memorie della Società Geologica Italiana, 52, pp. 557-578.

Bard P.Y. and SESAME-Team (2005) - Guidelines for the implementation for the H/V spectral ratio technique on ambient vibrations-measurements, processing and interpretations. SESAME European Research Project EVG1-CT-2000-00026, Deliverable D23.12 (available at http://sesame-fp5.obs.ujf-grenoble.fr.).

Baroň I., Bečkovskŷ D and Lumìr M. (2013) – Infrared thermography sensing for mapping open fractures in depp-seated rockslides and unstable cliffs. EGU General Assembly 2013, 7-12 April, Vienna, Austria, id. EGU2013-10189

Batayneh A.T. and Al-Diabat A.A. (2002) – Application of a two-dimensional electrical tomography technique for investigating landslides along the Amman-Dead Sera Highway, Jordan. Env. Geol., 42, pp. 399-403.

Bekler T., Ekinci Y.L., Demirci A., Erginal A.E. and Ertekin C. (2011) - Characterization of a Landslide using Seismic Refraction, Electrical Resistivity and Hydrometer Methods, Adatepe – Canakkale, NW Turkey. Journal of Environmental and Engineering Geophysics. Vol. 16, Issue 3, pp. 115-126.

Bell R., Kruse J.E., Garcia A. and Glade T. (2006) –Subsurface investigations of landslides using geophysical methods – geoelectrical applications in the Swabian Alb (Germany). Geographica Helvetica, Jg. 61, pp. 201-208.

Bensen G.D., Ritzwoller M.H., barmin M.P., Levshin A.L., Lin F., Moschetti M.P., Shapiro N.M. and Yang Y. (2007) – Processing seismic ambient noise data to obtain reliable broad-band surface wave dispersion measurements. *Geophys. J. Int.,* doi:10.1111/j.1365-246X.2007.03374.x.

Bichler A., Bobrowsky P., Best M., Douma M., Hunter J., Calvert T. and Burns R. (2004) – Three-dimensional mapping of a landslide using a multi-geophysical approach: the Quesnel Forks landslide. Landslides, 1 (1), pp. 29-40.

Bláha P. (1996) - Geoacoustic method and slope deformations. Senneset K (ed) Landslides. Seventh international symposium on landslides. Balkema, Rotterdam, pp. 1521–1524.

Blikra L. H. (2008) - The Åknes rockslide: Monitoring, threshold values and early warning. In Proceedings of 10th International Symposium on Landslides and Engineered Slopes, pp. 1089–1094. Xi'an, P.R. China, June 30–July 4, 2008.

Blikra L. H. (2012) - The Åknes rockslide, Norway. In J. J. Clague & D. Sead (Eds.), Landslides: Types mechanisms and modeling, pp. 323–335. UK: Cambridge University Press.

Boccaletti M., Elter P. and Guazzone G. (1971) – Plate tectonic models for the development of the western Alps and Northern Apennines. Nature, 234, pp. 108-111.

Bogoslovsky V.A. and Ogilvy A.A. (1977) - Geophysical methods for the investigation of landslides. Geophysics, 42, 3, pp. 562-571.

Bonnefoy-Claudet S., Cornou C., Bard P-Y, Cotton F., Moczo P., Kristek J. and Fäh D. (2006) – H/V ratio: a tool for site effects evaluation. Results from 1-D noise simulations. Geophys. J. Int., 167, 827-837, doi: 10.1111/ j.1365-246X.2006.03154.x.

Boschi E., Guidoboni E., Ferrari G., Valensise G. and Gasperini P. (1997) - CFTI, Catalogo dei Forti terremoti Italiani dal 461 a.c. al 1990. INGSGA, Bologna.

Bour M., Fouissac D., Dominique P. and Martin C. (1998) - On the use of microtremor recordings in seismic Microzonation. Soil Dyn. Earthq. Eng., 17, pp. 465–474.

Brenguier F., Campillo M., Hadziioannou C., Shapiro N.M., Nadeau R.M. and Larose E. (2008a) - Postseismic relaxation along the San Andreas Fault at Parkfield from continuous seismological observations, Science, 321, pp. 1478–1481.

Brenguier F., Shapiro N.M., Campillo M., Ferrazzini V., Duputel Z. Coutant O. and Nercessian A. (2008b) - Towards forecasting volcanic eruptions using seismic noise, Nat. Geosci., 1, pp. 126–130.

Brocca L., Ponziani F., Moramarco T., Melone F., Berni N. and Wolfgang Wagner (2012) – Improving landslide forecasting using ASCAT-derived soil moisture data: a case study of the Torgiovannetto landslide in Central Italy. *Remote Sensing*, 4 (5), 1232-1244; doi: 10.3390/rs4051232.

Brückl E., Brückl J. and Heuberger H. (2001) – Present structure and prefailure topography of the giant rockslide of Köfels. Zeitschrift für Gletscherkunde und Glazialgeologie, 37, pp. 49-79.

Bruno F., Levato L. and Marillier F (1998) - High resolution seismic reflection, EM and electrokinetic SP applied to landslide studies: ‘‘Le Boup’’ landslide (western Swiss Alps). Proc. Environmental and Engineering Geophysical Society (European Section), 14–17 Sept.

Bruno F. and Marillier F. (2000) - Test of high-resolution seismic reflection and other geophysical techniques on the Boup landslide in the Swiss Alps. Surveys in Geophysics, 21, pp. 333–348.

Burjànek J., Gassner-Stamm G., Poggi V., Moore J.R. and Fah D. (2010) - Ambient vibration analysis of an unstable mountain slope, Geophys. J. Int., 180, 820–828, doi:10.1111/j.1365-246X.2009.04451.x.

Burjànek J., Moore J.R., Molina F.X.Y. and Fah D. (2012) - Instrumental evidence of normal mode rock slope vibration, Geophys. J. Int., 188, pp. 559–569.

Butler R., Mazzoli S., Corrado S., De Donatis M., Scrocca D., Di Bucci D., Gambini R., Naso G., Nicolai C., Shiner P. and Zucconi V. (2004) - Applying thick-skinned tectonic model to the Apennine thrust belt of Italy. Limitations and Implications. In K.R. McClay (Ed.) Thrust Tectonics and Hydrocarbon Systems. AAPG Memoir 82, ISBN 0-89181-363-2, pp. 647-667.

Cadet H. (2007) - Utilisation combinèe des méthodes basées sur le bruit de fond dans le cadre du microzonage sismique. PhD thesis, Université J. Fourier, Grenoble.

Caris J.P.T. and Van Asch TH.W.J. (1991) – Geophysical, geotechnical and hydrological investigations of a small landslide in the French Alps. Eng. Geol., 31, pp. 249-276.

Carter A.J. and Kendall J.M. (2006) - Attenuation anisotropy and the relative frequency content of split shear waves. Geophys. J. Int., 165, pp. 865 – 874.

Casagli N., Gigli G., Lombardi L. and Nocentini M. (2006a) – Valutazione delle distanze di propagazione relative ai fenomeni franosi presenti sul fronte della cava di Torgiovannetto (PG) – rapporto 1.0. Studio commissionato dal Dipartimento della Protezione Civile.

Casagli N., Gigli G., Lombardi L. and Nocentini M. (2006b) – Valutazione delle distanze di propagazione relative ai fenomeni franosi presenti sul fronte della cava di Torgiovannetto (PG) – rapporto 2.0. Studio commissionato dal Dipartimento della Protezione Civile.

Casagli N., Gigli G., Lombardi L., Nocentini M. and Vannocci P. (2007a) – Indagini geofisiche e geotecniche e modellazione dinamica della frana di Torgiovannetto (Pg) –

Rapporto 1.0. Convenzione fra il Dipartimento di Scienze della Terra dell'Università di Firenze e la Provincia di Perugia.

Casagli N., Gigli G., Lombardi L., Nocentini M., Mattiangeli L. and Vannocci P. (2007b) - Indagini geofisiche e geotecniche e modellazione dinamica della frana di Torgiovannetto (Pg) – Rapporto 2.0. Convenzione fra il Dipartimento di Scienze della Terra dell'Università di Firenze e la Provincia di Perugia.

Casagli N., Catani F., Del Ventisette C. and Luzi G. (2010) – Monitoring, prediction, and early warning using ground-based radar interferometry. Lanslides, 7, pp.291-301. DOI 10.1007/s10346-010-0215-y.

Casagli N., Gigli G., Intrieri E., Lombardi L., Nocentini M. and Frodella W. (2012) - Applicazione di nuove tecnologie di indagine e monitoraggio per fenomeni di instabilità in ammassi rocciosi. In: Barla G., Barla M., Ferrero A.M., Rotonda T. - Nuovi metodi di indagine, monitoraggio e modellazione degli ammassi rocciosi, pp. 137-158, Torino: Celid.

Catellanos F. and Van der Baan M. (2013) – Microseismic event locations using double-difference algorithm. CSEG Recorder, 38, pp. 26-37.

Castellaro S., Mulargia F. and Bianconi L. (2005) – Passive seismic stratigraphy: a new efficient, fast and economic technique. Journal of Geotechnical and Environmental Geology, 13, 26.

Cassinis R., Tabacco I., Bruzzi G.F., Corno C., Brandolini A. and Carabelli E. (1984) - The contribution of geophysical methods to the study of the great Ancona landslide (December 13, 1982). Geoexploration, 23, pp. 363–386.

Carter A.J. and Kendall J.M. (2006) - Attenuation anisotropy and the relative frequency content of split shear waves. Geophys. J. Int., 165, pp. 865–874.

Chambers J.E., Hobbs P., Pennington C., Jones L., Dixon N., Spriggs M. et al. (2010) - Integrated LiDAR, geophysical and geotechnical monitoring of an active inland landslide, UK. Geophysical Research Abstracts 12, EGU2010-5244.

Chávez-García F.J., Pedotti G., Hatzfeld D. and Bardd P.-Y. (1990) – An experimental study on site effects near Thessalonifi (Northern Greece). Bull. Seism. Soc. Am., Vol.80, No. 4, pp. 784-806.

Chávez-García F.J. and Cuenca J. (1995) - Site effects in Mexico City urban zone. A complementary study, Soil Dyn., Earthquake Eng. 15, pp. 141-146.

Chen, Z. and Stewart, R. (2005) - Multi-window algorithm for detecting seismic first arrivals. Abstracts, CSEG National Convention, pp. 355-358.

Claerbout J.F. (1968) – Synthesis of a layered medium from its acoustic transmission response. Geophysics, 33 (2), pp. 264-269.

Cruden D.M. and Varnes D.J. (1996) – Landslides Types and Processes. In: Turner A.K., Schuster R.L. (Eds.), Landslides: Investigation and Mitigation. Transportation Research Board Special Report 247. National Academy Press, WA, pp. 36-75.

Daku B.L.F., Salt J.E. and Sha L. (2004) – An algorithm for locating microseismic events. Electrical and Computer Engineering, 2004. Canadian Conference, Vol.4, 2-5 Ma, pp. 2311-2314. DOI:10.1109/CCeCE.2004.1347708.

DeRoin N. and McNutt S. (2012) – Rockfalls at Augustine Volcano, Alaska: The influence of eruption precursors and seasonal factors on occurrence patterns 1997-2009. Journal of Volcanology and Geothermal Research, 211-212, pp. 61-75.

Del Gaudio V. and Wasowski J. (2007) - Directivity of slope dynamic response to seismic shaking. Geophys. Res. Lett. 34, L12301, doi: 10.1029/2007GL029842.

Del Gaudio V., Coccia S., Wasowski J., Gallipoli M.R. and Mucciarelli M. (2008) - Detection of directivity in seismic site response from microtremor spectral analysis. Nat. Hazards Earth Syst. Sci., 8, pp. 751–762, doi: 10.5194/nhess-8-751-2008.

Del Gaudio V., Lee C.T. and Wasowski J. (2011) - Inferring seismic response of landslide-prone slopes from microtremor study. Proc. Second World Landslide Forum, Rome, 3–7 October.

Del Gaudio V., Wasowski J. and Muscillo S. (2013) – New developments in ambient noise analysis to characterize the seismic response of landslide-prone slopes. Nat. Hazards Earth Sci., 13, pp. 2075-2087.

Demoulin A., Pissart A. and Schroeder C. (2003) – On the origin of late Quaternary palaeolandslides in the Liège (E Belgium) area. Int. J. Earth Sci. (Geol Rundsch), 92, pp.795-805.

Deschamps A., Innaccone G. and Scarpa R. (1984) - The Umbrian earthquake (Italy) of 19 September 1979. Annales Geophysicae 2, pp. 29–36.

Dixon N. and Spriggs M. (2007) - Quantification of slope displacement rates using acoustic emission monitoring. Canad. Geotech. J., 44(8), pp. 966–976. Accessed 15 Oct 2010.

Donnelly L.J., Culshaw M.G., Hobbs P.R.N., Flint R.C. and Jackson P.D. (2005) - Engineering geological and geophysical investigations of a slope failure at Edinburgh Castle, Scotland. Bulletin of engineering geology and the environment, 64, 2, pp. 119-137.

Draganov D., Campman X., Thorbecke J., Verdel A and Wapenaar K. (2009) – Reflection images from ambient seismic noise. Geophysics Vol. 74, No.5, pp. A63-A67.

Drew J.E., Leslie H.D., Armstrong P.N. and Michard G. (2005) – Automated microseismic event detection and location by continuous spatial mapping. SPE Annual Technical Conference and Exhibition, 9-12 October, Dallas, Texas. Society of Petroleum Engineers. http://dx.doi.org/10.2118/95513-MS.

Duncan P. and Eisner L. (2010) - Reservoir characterization using surface microseismic monitoring: Geophysics, 75, no. 5.

Duval A.M. and Vidal S. (1998) - Microzonage de Tunis (Tunisie). Étude de l'aléa sismique local par enregistrement de séismes et de bruit de fond. Compte rendu de recherche du CETE Méditerranée n° 97.740.6060 au LCPC dans le cadre de la coopération CETE/LCPC/ENIT, Thème 036, Sujet 1 36 01 7 Actions sismiques, 100 pages.

Duval A.M., Vidal S., Méneroud J.P., Singer A., De Santis F., Ramos C., Romero G., Rodriguez R., Pernia A., Reyes N. and Griman C. (2001) - Caracas, Venezuela: Site effect determination with microtremors. Pure and Applied Geophysics, Pageoph, Vol.158, n° 12, pp. 2513-2523.

Dziewonski A., Franzen, J. and Woodhouse, J. (1985) - Centroid-moment tensor solutions for April–June, 1984. Physics of the Earth and Planetary Interiors 37, pp. 87–96.

Eaton D., Caffagni E., Rafiq A., van der Baan M. and Roche V. (2014) - Passive seismic monitoring and integrated geomechanical analysis of a tight-sand reservoir during hydraulic-fracture treatment, flowback and production: URTeC: 1929223.

Eisner L., Duncan P.M., Heigl W.M. and Keller W.R. (2009) - Uncertainties in passive seismic monitoring: The Leading Edge, 28, no. 6, pp. 648–655.

Eisner L., Hulsey B.J., Duncan P., Jurick D., Heigl W. and Keller W. (2010) - Comparison of surface and borehole locations of induced seismicity: Geophysical Prospecting, 58, no. 5, pp. 805–816.

Ekstroem G., Morelli A., Boschi E. and Dziewnonski A. (1998) - Moment tensor analysis of the central Italy earthquake sequence of September– October 1997. Earth and Planetary Sciences Letters 25, pp. 1971–1974.

Fäh D., Kind F. and Giardini D. (2001) – A theoretical investigation of average H/V ratios. . *Geophys. J. Int.* 145, pp. 535-549.

Felicioni G., Martini E., and Ribaldi C. (1994) - Studio dei Centri Abitati Instabili in Umbria. Atlante regionale: CNR GNDCI publication number 979, Rubettino Publisher, (in Italian), 418.

Fell R., Hungr O., Leroueil S. and Riemer W. (2000) - Keynote paper – Geotechnical engineering of the stability of natural slopes and cuts and fills in soil. Proc. GeoEng2000, Int. Conf. on Geotechnical and Geol. Eng. in Melbourne, Australia, Vol 1, Technomic Publishing, Lancaster, pp. 21-120, ISBN: 1-58716-067-6.

Ferrucci F., Amelio M., Sorriso-Valvo M. and Tansi C. (2000) – Seismic prospecting of a slope affected by deep-seated gravitational slope deformation: the Lago Sackung, Calabria, Italy. Eng. Geol., 57, pp. 53-64.

Field E.H. and Jacob K. (1993) - The theoretical response of sedimentary layers to ambient seismic noise. Geophys. Res. Lett., 20, pp. 2925-2928.

Field E.H. (1994) - Earthquake site response estimation. Ph.D. Thesis, Columbia University, New York, pp. 303.

Field E.H., Clement A.C., Jacob K.H, Aharonian V., Hough S.E, Friberg P.A, Babaian T.O., Karapetian S.S., Hovanessian S.M. and Abramian H.A. (1995) - Earthquake site response in Giumri (formerly Leninakan), Armenia, using ambient noise observations. Bull. Seism. Soc. Am. 85, pp. 349-353.

Frodella W., Morelli S., Gigli G. and Casagli N. (2014) - Contribution of infrared thermography to the slope instability characterization. In: World Landslide Forum 3, Beijing, China, 2-6 June 2014, WLF, pp. 97-103.

Gaffet S., Guglielmi Y., Cappa F., Pambrun C., Monfret T. and Amitrano D. (2010) – Use of the simultaneous seismic, GPS and meteorological monitoring for the characterization of a large unstable mountain slope in the Southern French Alps. Geophysical Journal International, 182, 1395-1410.

Gallipoli M.R., Lapenna V., Lorenzo P., Mucciarelli M., Perrone A., Piscitelli S. and Sdao F. (2000) – Comparison of geological and geophysical prospecting techniques in the study of a landslide in Southern Italy. European Journal of environmental and engineering geophysics, 4, pp. 117-128.

Gesret A., Desassis N., Noble M., Romary T. and Misons C. (2015) – Propagation of the velocity model uncertaintiesto the seismic event location. Geophys. J. Int., 200 (1), pp. 52-66. Doi: 10.1093/gji/ggu374.

Gigli G. and Casagli N. (2013) - Extraction of rock mass structural data from high resolution laser scanning products. In: Margottini C., Canuti P., Sassa K. - Landslide Science and Practice - Volume 3: Spatial Analysis and Modelling, pp. 89-94 Springer Berlin Heidelberg, ISBN:9783642313097.

Giocoli A., Stabile T.A., Adurno I., Perrone A., Gallipoli M.R., Gueguen E., Norelli E. and Piscitelli S. (2015) – Geological and geophysical characterization of the southern side of the High Agri Valley (southern Apennines, Italy). Nat. Hazards Earth Syst. Sci, 15, pp. 315-323.

Glade T, Stark P. and Dikau R. (2005) - Determination of potential landslide shear plane depth using seismic refraction - a case study in Rheinhessen, Germany. Bulletin of engineering geology and the environment 6, pp. 151-158.

Goertz-Allman B.P., Kuehn D., Oye V., Bohloli B. and Aker A. (2014) - Combining microseismic and geomechanical observations to interpret storage integrity at the In Salah CCS site. Geophys. J. Int., 198, pp. 447-461.

Goldstein P., Dodge D., Firpo M., Minner L. (2003) - SAC2000: Signal processing and analysis tools for seismologists and engineers. Invited contribution to “The IASPEI International Handbook of Earthquake and Engineering Seismology”. Edited by Lee W.H.K., Kanamori H., Jennings P.C., and Kisslinger C., Academic Press, London, 2003.

Goldstein P. and Snoke A. (2005) - SAC Availability for the IRIS Community. Incorporated Institutions for Seismology Data Management Center Electronic Newsletter. http://www.iris.edu/news/newsletter/vol7no1/page1.htm.

Gomberg J., Schulz W., Bodin P. and Kean J. (2011) – Seismic and geodetic signatures of fault slip at the Slumgullion Landslide Natural Laboratory. Journal of Geophysical Research, 116, B09404, doi: 10.10129/2011JB008304.

Got J.-L., Mourot P. and Grangeon J. (2010) – Pre-failure behaviour of an unstable limestone cliff from displacement and seismic data. Nat. Hazards Earth Syst. Sci., 10, pp. 819-829, 2010.

Graziani A., Marsella M., Rotonda T., Tommasi P. and Soccodato C. (2009b) – Study of a rock slide in a limestone formation with clay interbeds. Proc. Int. Conf. on Rock Joints and Jointed Rock Masses, Tucson, Arizona, USA 7th-8th January 2009.

Hadziioannou C., Larose E., Baig A., Roux P. & Campillo, M. (2011) - Improving temporal resolution in ambient noise monitoring of seismic wave speed, J. Geophys. Res., 116, B07304, doi: 10.1029/2011JB008200.

Hafez A. and Kohda T. (2009) - Accurate P-wave arrival detection via MODWT: International Conference on Computer Engineering & Systems, IEEE, pp. 391-396.

Häge M and Joswig M (2009) - Microseismic study using small arrays in the swarm area of Novy Kostel: increased detectability during an inter-swarm period. Studia Geophysica et Geodaetica, 52(4), pp. 651–660. Accessed 15 Oct 2010.

Hattori K., Yabe S., Otsubo H., Kono H., Tojo Y., Terajima T. and Ochiai H. (2011) – Self-Potential Approach to Early Warning for Rainfall-induced Landslide. American Geophysical Union, Fall Meeting 2011.

Havenith H.B., Jongmans D., Faccioli E., Abdrakhmatov K. and Bard P.-Y. (2002) - Site effects analysis around the seismically induced Ananevo rockslide, Kyrgyzstan. Bulletin of the Seismological Society of America, 92, pp. 3190–3209.

Hadziioannou C., Larose E. Coutant O., Roux P. and Campillo M. (2009) – Stability of monitoring weak changes in multiply scattering media with ambient noise correlation: laboratory experiments. J. acoust. Soc. Am., 125, pp.3688-3695.

Helmstetter A. and Garambois S. (2010) – Seismic monitoring of Séchilienne Rockslide (French Alps): analysis of seismic signals and their correlation with rainfalls. J. Geophys. Res. doi: 10.1029.

Herat M. (2008) - Model HVSR: a Matlab® tool to model horizontal-to-vertical spectral ratio of ambient noise. Comput. Geosci., 34, pp. 1514–1526.

Horike M., Zhao B. and H. Kawase (2001). Comparison of site response characteristics inferred from microtremors and earthquake shear waves, Bull. Seism. Soc. Am.81, pp. 1526 –1536.

Intrieri E., Gigli G., Mugnai F., Fanti R. and Casagli N. (2012) – Design and implementation of a landslide early warning system. Engineering Geology, 147-148, pp. 124-136.

Jibson R.W. and Keefer D.K. (1992) - Analysis of the seismic origin of a landslide in the New Madrid Seismic Zone, Seismol. Res. Lett., 63, pp. 427– 437.

Jones G.A., Raymer D., Chambers K. and Kendall J.M. (2010) - Improved microseismic event location by inclusion of a priori dip particle motion: a case study from Ekofisk: Geophysical Prospecting, 58, no. 5, pp. 727–737.

Iriantoro Putra G.H., Jongamns D. and Baillet L. (2012) – Analysis and classification of seismic data events recorded on a prone-to-fall column. Study case: Chamousset, French Alps. Thesis – Master of Earthquake Engineering and Engineering Seismology (MEEES).

Jibson R.W. and Keefer D.K., (1993) - Analysis of the seismic origin of landslides: Examples from the New Madrid seismic zone, Geol. Soc. Am. Bull., 105, pp. 521–536.

Jongmans D., Hemroulle P., Demanet D., Renardy F., and Vanbrabant Y. (2000) - Application of 2D electrical and seismic tomography techniques for investigating landslides. European Journal of Environmental and Engineering Geophysics, 5, pp. 75–89.

Jongmans D. and Garambois S. (2007) - Geophysical investigation of landslides: a review. Bulletin Societe Geologique de France, 178 (2), pp. 101-112. <10.2113/gssgfbull.178.2.101>. <hal-00196268>.

Joswig M (2008) - Nanoseismic monitoring fills the gap between microseismic networks and passive seismic. First Break, 26, pp. 81–88.

Kanai K. (1957) – The requisite conditions for predominant vibration of ground. Bull. Earthquake Res. Inst. Tokyo Univ., Vol. 31, p. 457.

Kawase H., Sànchez-Sesma J. and Matsushima S. (2011) – The optimal use of horizontal-to-vertical spectral ratios of earthquake motions for velocity inversions based on diffuse-field theory for plane waves. Bull. Seism. Sec. Am., Vol. 101, No.5, pp. 2001-2014, October 2011.

Kearey P., Brooks M. and Hill I. (2002) - An introduction to geophysical exploration. Wiley, Blackwell.

Khazai B. and Sitar N. (2004) - Evaluation of Factors Controlling Earthquake- Induced Landslides Caused by Chi-Chi Earthquake and Comparison with the Northridge and Loma Prieta Events, Eng. Geol., 71, pp. 79–95.

Kolesnikov Yu. I., Nemirovich-Danchenko M. M., Goldin S. V. and Seleznev V. S. (2003) – Slope stability monitoring from microseismic field using polarization methodology. Natural Hazards and Earth System Sciences (3), pp. 515-521.

Kwiatek G., Plenkers K., Nakatani M., Yabe Y., Dresen G. and JAGUARS-Group (2010) – Frequency-Magnitude Characteristics Down to Magnitude -4.4 for Induced Seismicity Recorded ad Mponeng Gold Mine, South Africa. Bull. Seism. Soc. Am., Vol.100, No.3, pp. 1165-1173, June 2010.

Yabe Y., Philipp J., Nakatani M., Morema G., Naoi M., Kawakata H., Igarashi T., Dresen G., Ogasawara H. and JAGUARS (2009) – Observation of numerous aftershocks of an Mw 1.9 earthquake with an AE network installed in a deep gold mine in South Africa. Earth Planet Space, 61, e49-e52, 2009.

Lachet C. and Bard P.Y. (1994) - Numerical and theoretical investigations on the possibilities and limitations of the Nakamura's technique. J. Physics of the Earth, 42-4, pp. 377–397.

Lachet C., Hatzfeld D., Bard P.Y., Theodulidis N., Papaioannou C. and Savvaidis A. (1996) - Site effects and microzonation in the city of Thessaloniki (Greece). Comparison of different approaches. Bull. Seism. Soc. Am., 86, 6, pp. 1692-1703.

Lacroix P. and Helmstetter A. (2011) – Location of Seismic Signals Associated with Microearthquakes and Rockfalls on the Séchilienne Landslide, French Alps. Bull. Seism. Sec. Am. Vol.101, No.1, pp. 341-353, February 2011, doi: 10.1785/0120100110.

Lapenna V., Lorenzo P., Perrone A., Piscitelli S., Sdao F., and Rizzo E. (2003) - High-resolution geoelectrical tomographies in the study of Giarrossa landslide (southern Italy). Bulletin of Engineering Geology and the Environment, 62, pp. 259–268.

Lapenna V., Lorenzo P., Perrone A., Piscitelli S., Rizzo E. and Sdao F. (2005) – 2D electrical resistivity imaging of some complex landslides in Lucanian Apennine chain, southern Italy. Geophysics, 70, B11-B18.

Lavecchia G., Brozzetti F., Barchi M., Keller J. and Menichetti M., (1994) - Seismotectonic zoning in east-central Italy deduced from the analysis of the Neogene to present deformations and related stress fields. Soc. Geol. Am. Bull., 106, pp. 1107-1120.

Lebourg T., Binet S., Tric E., Jomard H. and El Bedoui S. (2005) - Geophysical survey to estimate the 3D sliding surface and the 4D evolution of the water pressure on part of a deep seated landslide. Terra Nova 17(5), 399-406.

Lee C.C., Yang C.H., Liu H.C., Wen K.L., Wang Z.B. and Chen Y.J. (2008) - A study of the hydrogeological environment of the Li-shan landslide area using resistivity image profiling and borehole data. Engineering Geology, 98 (3-4), pp. 115-125.

Lee R.F., Abbott R.E.; Knox H.A. and Pancha A. (2014) – Seasonal changes in H/V spectral ratio at high-latitude seismic stations. American Geophysical Union - AGU, Fall Meeting 2014.

Lermo J. and Chávez-García F.J. (1993) - Site effect evaluation using spectral ratios with only one station. Bull. Seism. Soc. Am., 83, pp. 1574 - 1594

Lermo J. and Chávez-Garcìa F.J. (1994) - Are microtremors useful in site response evaluation? Bull. Seism. Soc. Am. 84, pp. 1350-1364.

Levy C., Jongmans D. and Baillet L. (2011) – Analysis of seismic signal recorded on a prone-to-fall rock column (Vercors massif, French Alps). Geophysical J. Int., 186 (1), pp. 296-310, doi: 10.1111/j.1365-246X.2011.05046.x.

Lin F.C., Moschetti M.P. and Ritzwoller M.H. (2007) - Surface wave tomography of the Western United States from ambient seismic noise: Rayleigh and love wave phase velocity maps, Geophys. J. Int., 173, pp. 281– 298.

Locati M., Camassi R. e M. Stucchi (2011) - DBMI11, the 2011 version of the Italian Macroseismic Database. Milano, Bologna, http://emidius.mi.ingv.it/DBMI11, DOI: 10.6092/INGV.IT-DBMI11.

Lomax A. and A. Michelini (2009), Mwpd: A Duration-Amplitude Procedure for Rapid Determination of Earthquake Magnitude and Tsunamigenic Potential from P Waveforms, Geophys. J. Int.,176, 200-214, doi:10.1111/j.1365-246X.2008.03974.x

Lozano L., Herraiz M. and Singh S. K. (2009) – Site effect study in central Mexico using H/V and SSR techniques: Independence of seismic site effects on source characteristics. Soil Dynamics and Earthquake Engineering 29, pp. 504-516.

Lundberg E., Malehmir A., Juhlin C., Bastani M. and Andersson A. (2014) - High-resolution 3D reflection seismic investigation over a quick-clay landslide scar in southwest Sweden: Geophysics, 79, no. 2, pp. B97– B107, doi: 10.1190/geo2013-0225.1.

Mainsant G., Larose E., Brönnimann C., Jongmans D, Michoud C., and Jaboyedoff M. (2012) – Ambient seismic noise monitoring of a clay landslide: Toward failure prediction, J. Geophys. Res., 117, F01030, doi: 10.1029/2011JF002159.

Malehmir A., Saleem M.U. and Bastani M. (2013) - High-resolution reflection seismic investigations of quick-clay and associated formations at a landslide scar in southwest Sweden: Journal of Applied Geophysics, 92, pp. 84–102, doi: 10.1016/j.jappgeo.2013.02.013.

Malischewsky P.G. and Scherbaum F. (2004) – Love's formula and H/V ratio (ellipticity) of Rayleigh waves. Wave Motion, 40, pp. 57-67.

Mantovani E., Viti M., Babbucci D., Cenni N., Tamburelli C., Vannucchi A. and Falciani F. (2014) – Assetto tettonico e potenzialità sismogenetica dell'Appennino Tosco-Umbro-Marchigiano.

Mavko G. (1992) – Parameters that influence seismic velocity: conceptual overview of rock and fluid factors that impact seismic velocity and impedance. Stanford Rock Physics Laboratory, pp. 73-112.

McCann D.M. and Forster A. (1990) - Reconnaissance geophysical methods in landslide investigations. Engineering geology, 29, 1, pp. 59-78.

McKean J., Bird E., Pettinga J., Campbell J. and Roering J. (2004) – Using LiDAR to pbjectively map bedrock landslide and infer their mechanics and material properties. Denver Annual Meeteing, November 7-10. Geological Sociaety of America Abstract with Programs, 36 (5), 332.

McKean J. and Roering J. (2004) – Objective landslide detection and surface morphology mapping using high-resolution airborne laser altimetry. Geomorphology, 57, pp. 331-351.

Méric O., Garambois S., Jongmans D., Wathelet M., Chatelain J.L and Vengeon J.M. (2005) – Application of geophysical methods for the investigation of the large gravitational mass movement of Séchilienne, France. Canadian Geotechnical Journal, 42, pp. 1105-1115, doi: 10.1139/T05-034.

Méric O., Garambois S. and Orengo Y. (2006) – Large gravitational movement monitoring using a spontaneous potential network. Proc. 19th Annual meeting of SAGEEP, Seattle, USA, EEGS Ed., Denver, USA, p. 6.

Méric O., Garambois S., Malet J.P., Cadet H., Gueguen P. and Jongmans D. (2007) - Seismic noise-based methods for soft-rock landslide characterization. Bulletin Société Géeologique de France, 178 (2), pp.137-148. .

Milsom J. (2003) - Field geophysics. Wiley, New York.

Mirabella F., Ciaccio M.G., Barchi M.R. and Merlini S. (2004) – The Gubbio normal fault (Central Italy): geometry, displacement distribution and tectonic evolution. Journal of Structural Geology, 26, pp. 2233-2249.

Mucciarelli M. and Gallipoli M.R. (2001) – A critical review of 10 years of microtremor HVSR technique. Bollettino di Geofisica Teorica ed Applicata. Vol. 42, N. 3-4, pp. 255-266.

Mucciarelli M. (2007) – Jumpin' Joy Quake. Seismol. Res. Lett, 77, pp. 744-745, doi: 10.1785/gssrl.77.6.744.

Nakahara H. (2014) – Auto correlation analysis of coda waves from local earthquakes for detecting temporal changes in shallow subsurface structure: the 2011 Tohoku-Oki, Japan, Earthquake. Pure and Applied geophysics, 172, pp.213-224. Doi:10.1007/s00024-014-0849-0.

Nakamura Y. (1989) – A method for dynamic characteristics estimations of subsurface using microtremors on the ground surface. Q. Rep. RTRI Jpn. 30, pp. 25-33.

Nakamura Y. (2000) - Clear identification of fundamental of Nakamura's technique and its applications, no. 2656, Proc. of the 12th World Conference on Earthquake Engineering, Auckland, New Zealand.

Nielsen M.H. (2009) - Structure and microseismicity of the unstable rock slide at Åknes, Norway. Ms. Thesis Geosciences, University of Oslo.

Newmark N.M. (1965) - Effects of earthquakes on dams and embankments. Géotechnique, vol. XV, n. 2, pp. 139-159.

Nogoshi M. and Igarashi T. (1970) – On the propagation characteristics estimations of subsurface using microtremors on the ground surface. J. Seismol. Soc. Jpn. 23, pp. 264-280.

Nogoshi M. and Igarashi T. (1971) – On the amplitude characteristics of microtremor (Part 2). J. Seismol. Soc. Jpn. 24, pp. 26-40.

Nunziata C., De Nisco G. and Panza G. F. (2009) - S-waves profiles from noise cross correlation at small scale. Engineering Geology, 105, pp. 161–170.

Ogunsuyi O.O., Schmitt D.R. and Martin D. (2011) – Geophysical Study of the Peace River Landslide. CSPG CSEG CWLS Convention.

Oliveto A., Mucciarelli M. and Caputo R. (2004) - HVSR prospecting in multi-layered environments: an example from the Tyrnavos Basin (Greece). Journal of Seismology, 8, 395-406.

Olsen K.B. (1989) - A stable and flexible procedure for the inverse modeling of seismic first arrivals. Geophysical Prospecting, 37, pp. 455–465.

Ordaz M. and Singh S. K. (1992) – Source spectra and spectral attenuation of seismic waves from Mexican earthquakes, and evidence of amplification in the hill zone of Mexico City. Bull. Seism. Soc. Am. 1992; 1:341-55.

Palmer D. (1980) - The generalized reciprocal method of seismic refraction interpretation. Society of Exploration Geophysicists, Tulsa, Oklahoma, pp. 104.

Pandolfi D., Bean C.J. and Saccorotti G. (2006) – Coda wave interferometric detection of seismic velocity changes associated with the 1999 M=3.6 event at Mt. Vesuvius. Geophysical Research Letters, 33, L06306, doi: 10.1029/2005GL025355.

Panzera F., Lombardo G., D'Amico S. and Galea P. (2013) - Speedy Techniques to Evaluate Seismic Site Effects in Particular Geomorphologic Conditions: Faults, Cavities, Landslides and Topographic Irregularities (chapter 5). InTech, pp. 102-138.

Pischiutta, M., Rovelli, A., Salvini, F., Di Giulio, G. and Ben-Zion Y. (2013) - Directional resonance variations across the Pernicana Fault, Mt.Etna, in relation to brittle deformation fields. Geophysical Journal International, vol.193, pp.986-996.

Parolai S., Richwalski S.M., Milkereit C. and Bormann P. (2004) – Assessment of the stability of H/V spectral ratios from ambient noise and comparison with earthquake data in the Cologne area (Germany). Tectonophysics 390, pp. 57-73.

Parolai S. and Galiana Merino J.J. (2006) – Effect of transient seismic noise on estimates of H/V spectral ratios. B. Seismol. Soc. Am., 96, pp. 228-236, doi: 10.1785/0120050084.

Perrone A., Piscitelli S. and Lapenna V. (2014) – Electrical resistivity tomographies for landslide monitoring: a review. Earth Science Reviews, 135.

Peterson J. (1993) - Observation and modeling of seismic background noise. U.S. Geol. Surv. Open File Report.

Petronio L., Boaga J. and Cassiani G. (2006) – Reflection seismic and surface wave analysis on complex heterogeneous media: the case of Mount Toc landslide in the Vajont valley. Italian Journal of Engineering Geology and Environments, Vol. 6, pp. 593-598.

Pilz M., Parolai S., Leyton F., Campos J. and Zschau J. (2009) – A comparison of site response techniques using earthquake data and ambient seismic noise analysis in the large urban areas of Santiao de Chile. Geophys. J. Int., 178 (2), pp. 713-728.

Pilz M., Parolai S., Bindi D., Saponaro A. and Abdybachaev U. (2013) – Combining Seismic Noise Techniques for landslide Characterization. Pure and Applied Geophysics. doi: 10.1007/s00024-013-0733-3.

Picozzi M., Parolai S., Bindi D. and Strollo A. (2009) - Characterization of shallow geology by high frequency seismic noise tomography. Geophysical Journal International, 176, pp. 164–174.

Ponziani F., Berni N., Pandolfo C., Stelluti M. and Brocca L. (2010) – An integrated approach for the real-time monitoring of a high risk landslide by a regional civil protection office, EGU Leonardo Topical Conference Series on the hydrological cycle 2010, Luxembourg, 10-12 November 2010.

Popescu M., Urdea P. and Şerban R. (2014) – Revealing the landslide structure using the electrical tomography technique. Case study: Buzad active landslide. Geographica Timisiensis, vol. XXIII, nr.2, pp. 87-96.

Pullammanappallil S.K. and Louie J.N. (1994) - A generalized simulated-annealing optimization for inversion of first arrival times. Bulletin of the Seismological Society of America, 84, pp.1397–1409.

Ratdomopurbo A. and Poupinet G. (1995) – Monitoring a temporal change of seismic velocity in a volcano: application to the 1992 eruption of Mt. Merapi (Indonesia). Geophysical Research Letters. Vol. 22, No.7, pp.775-778; doi: 10.1029/95GL00302

Renalier F., Jonmans D., Campillo M. and Bard P.-Y. (2010) - Shear wave velocity imaging of the Avignonet landslide (France) using ambient noise cross correlation. Journal of geophysical research, Vol. 115, F03032, doi: 10.1029/2009JF001538.

Reynolds J.M. (1997) – An introduction to applied and environmental geophysics. John Wiley & Sons, New York.

Rodriguez I.V. (2011) – Automatic Time-picking of Microseismic Data Combining STA/LTA and the Stationary Discrete Wavelet Transform. CSPG CSEG CWLS Convention 1.

Roux P., Sabra K.G. and Kuperman W.A. (2005) – Ambient noise cross correlation in free space: Theoretical approach. J. Acoust. Soc. Am., 117 (1), pp. 79-84.

Roux P.F., Marsan D., Metaxian J.P., O'Brien G. and Moreau L. (2008) - Microseismic activity within a serac zone in an alpine glacier (Glacier d'Argentière, Mont Blanc, France). J. Glaciol. 54, pp. 157–168, 184.

Sabra K.G., Roux P. and Kuperman W.A. (2005) – Emergence rate of the time-domain Green's function from the ambient noise cross-correlation function. J. Acoust. Soc. Am. 118 (6), pp. 3524-3531.

Sánchez-Sesma F., Rodríguez M., Iturrarán-Viveros U., Luzón F., Campillo M., Margerin L., García-Jerez A., Suarez M., Santoyo M.A. and Rodríguez-Castellanos A. (2011) – A theory for microtremor H/V spectral ratio: application for a layered medium. Geophysical Journal International, 186, pp. 221-225.

Seats K.J., Lawrence J.F. and Prieto G.A. (2012) – Improved ambient noise correlation functions using Welch's method. Geophysical Journal International, 188, pp. 513-523, doi: 10.1111/j.1365-246X.2011.05263.x.

Sens-Schönfelder C. and Wegler U. (2006) - Passive image interferometry and seasonal variations of seismic velocities at Merapi Volcano, Indonesia. Geophys. Res. Lett., 33, L21302, doi: 10.1029/2006GL027797.

Senfaute G., Duperret A. and Lawrence J.A. (2009) – Micro-seismic precursory cracks prior to rock-fall on coastal chalk cliffs: a case study at Mesnil-Val, Normandie, NW France. Nat. Hazards Earth Syst. Sci., 9, pp. 1625-1641, 2009.

Schmutz M., Albouy Y., Guerin R., Maquaire O., Vassal J., Schott J.-J. and Descloîtres M. (2000) - Joint electrical and time domain eleclromagnetism (TDEM) data inversion applied to the Super Sauze earthflow (France). Surveys in geophysics, 21, 4, pp. 371-390.

Schmutz M., Guerin R., Andrieux P. and Maquaire O. (2009) - Determination of the 3D structure of an earthflow by geophysical methods. The case of Super Sauze, in the French Southern Alps. Journal of Applied Geophysics, 68 (4), pp. 500-507

Schrott L, Hördt A, Dikau R (2003) - Geophysical applications in geomorphology. Borntraeger, Berlin.

Shan C., Bastani M., Malehmir A., Persson L. and Engdahl M. (2014) – Integrated 2D modeling and interpretation of geophysical and geotechnical data to delineate quick clays at a landslide site in southwest Sweden. Geophysics, Vol. 79, No. 4, EN61-EN75. Doi:10.1190/GEO2013-0201.1.

Shapiro N.M. and Campillo M. (2004) - Emergence of broadband Rayleigh waves from correlations of the ambient seismic noise, Geophys. Res. Lett., 31, L07614, doi: 10.1029/2004GL019491.

Shapiro N.M, Campillo M., Stehly L. and Ritzwoller M.H. (2005) – High-resolution surface-wave tomography from ambient seismic noise. Science, 307, pp. 1615-1617.

Snieder R. (2004) – Extracting the Green's function from the correlation of coda waves: a derivation based on stationary phase, Phys. Rev. E., 69, pp. 1–8, doi: 10.1103/PhysRevE.69.046610.

Spillman T., Maurer H., Green A. G., Heincke B., Willenberg H. and Husen S. (2007) - Microseismic investigation of an unstable mountain slope in the Swiss Alps. Journal of Geophysical Research 112, Paper no. B07301.

Staněk F., Anikiev D., Valenta J. and Eisner L. (2015) – Semblance for microseismic event detection. Geophys. J., Int., 201 (3), pp. 1362-1369.

Supper R., and Römer A. (2003) - New achievements in developing a high speed geoelectrical monitoring system for landslide monitoring. In Proceedings of the 9th Meeting of Environmental and Engineering Geophysics, Prague, Czech Republic. O-004.

Surinach E., Vilajosana I., Khazaradze G., Biescas B., Furdada G., and Vilaplana J.M. (2005) – Seismic detection and characterization of landslides and other mass movements. Natural Hazards and Earth System Sciences, 5, pp. 791–798.

Swanson P.L., Estey L.H., Boler F.M. and Billington S. (1992) – Mining-induced microseismic event location errors: accuracy and precision of two location system. Pageoph., Vol. 139, No. ¾.

Tanimoto T., Ishimaru S. and Alvizuri C. (2006) – Seasonality in particle motion of microseisms. Geophys. J. Int., 166, pp. 253-266. Doi: 10.1111/j.1365-246X.2006.02931.x

Tonnellier A., Helmstetter A., Malet J.P., Schmittbuhl J., Corsini A. and Joswig M. (2013) – Seismic monitoring of soft-rock landslides: the Super-Sauze and Valoria case studies. Geophysical Journal International. doi: 10.1093/gji/ggt039.

Triantafyllidis P. and Hatzidimitriou P.M. (2002) – Influence of source on 2-D site effects. Geophysical Research Letters, Vol.29, No.6, 1089, 10.1029/2001GL013870, 2002.

Trifunac M.D. and Todorovska M.I. (2000) – Long period microtremors, microseisms and earthquake damage: Northridge, CA, earthquake of 17 January 1994. Soil Dynamics and Earthquake Engineering, 19, pp.253-267.

Trnkoczy A. (2002) - Understanding and parameter setting of STA/LTA trigger algorithm. In: Bormann, P. (Ed.), IASPEINew. Manual of Seismological Observatory Practice, Vol. 2. GeoForschungs Zentrum Potsdam, pp. 119.

Usher P.J., Angus D.A. and Verdon J.P. (2013) - Influence of a velocity model and source frequency on microseismic waveforms: some implications for microseismic locations. Geophysical Prospecting, 61 (Supple), pp. 334 - 345 (12).

Vilajosana I., Suriñach E., Abellán A., Khazaradze G., Garcia D. and Llosa J. (2008) – Rockfall induced seismic signals: case study in Montserrat, Catalonia. Nat. Hazards Earth Sci., 8, pp. 805-812.

Volant P., Cotton F. and Gariel J.C. (1998) - Estimation of site response using the H/V method. Applicability and limits of this technique on Garner Valley Downhole Array dataset (California). In: Proc. of 11th Europ. Conf. Earthq. Eng., Balkema, Rotterdam, 13 pp., CD-ROM.

Walter M. and Joswig M. (2008) - Seismic monitoring of fracture processes generated by a creeping landslide in the Vorarlberg Alps. First Break, 26, pp. 131-135.

Walter M., Arnhardt C. and & Joswig M. (2012) - Seismic monitoring of rockfalls, slide quakes, and fissure development at the Super-Sauze mudslide, French Alps. Engineering Geology, 128, pp. 12-22.

Wapenaar K. (2004) - Retrieving the elastodynamic Green's function of an arbitrary inhomogeneous medium by cross correlation, Phys. Rev. Lett., 93, 254301, doi:10.1103/PhysRevLett.93.254301.

Wilson R.C. and Keefer D.K. (1983) - Dynamic analysis of a slope failure from the 6 August 1979 Coyote Lake, California, earthquake, Bull. Seism. Soc. Am., 73, pp. 863–877.C

Wong J., Han L., Bancroft J.C. and Stewart R. (2009) - Automatic time-picking of first arrivals on noisy microseismic data. CSEG Microseismic Workshop.

Wust-Bloch G.H. and Tsesarsky M. (2013) – Structure health monitoring in natural environments: pre-failure event location and full-waveform characterization by nanoseismic monitoring. Journal of environmental and engineering geophysics. Vol. 18, Issue 4, pp. 219-232.

Yang Y., Ritzwoller M.H., Levshin A.L. and Shapiro, N.M. (2007) - Ambient noise Rayleigh wave tomography across Europe, Geophys. J. Int., 168, pp. 259–274.

Zaki A., Chai H.K., Razak H.A. and Shiotani T. (2014) – Monitoring and evaluating the stability of soil slopes: A review on various available methods and feasibility of acoustic emission technique. Comptes Rendus Geosciences, 346 (9-19), pp. 223-232.

Zoppè G., Costa G., Dixon N., Spriggs M.P. and Marcato G. (2015) – Microseismicity and acoustic emission for landslide monitoring (North-East Italy). Engineering Geology for Society and Territory. Vol.2, pp. 1527-1530.